Finite Element Modeling of a Textured Seal Design for Reduced Wear

by

Oscar C.H. Yeh

S.B. Mechanical Engineering
Massachusetts Institute of Technology (1995)

Submitted to the Department of Mechanical Engineering
in partial fulfillment of the requirements for the degree of

Master of Science in Mechanical Engineering

at the

MASSACHUSETTS INSTITUTE OF TECHNOLOGY

May 9, 1997

Author .....
Department of Mechanical Engineering
May 9, 1997

Certified by .....
Mary C. Boyce
Associate Professor of Mechanical Engineering
Thesis Supervisor

Accepted by .....
Ain A. Sonin
Chairman, Department Committee on Graduate Students
Department of Mechanical Engineering

Finite Element Modeling of a Textured Seal Design for Reduced Wear

by

Oscar C.H. Yeh

Submitted to the Department of Mechanical Engineering on May 9, 1997, in partial fulfillment of the requirements for the degree of Master of Science in Mechanical Engineering

Abstract

Seals are universally employed to perform duties related to fluid sealing and joint packing. Though regarded as a generic component, their role is often vital to the performance of mechanical devices. The lifetime of a seal can determine the length of time before maintenance of the machine or device is required. Thus, extending the life of seals is especially critical for those operating in hostile environments such as mud. Because the presence of such abrasives can seriously compromise the life of a seal, this thesis considers the redesign of a seal that is used in the undercarriages of earth moving vehicles. Both *geometric* and *material* changes are considered in order to improve wear life.

Geometric modifications in the form of surface textures were considered after finite element modeling and experimental results determined that the seal wear was primarily due to regions of intensified stress and strain in the seal lip caused by abrasive particles. It was hypothesized that surface textures could "trap" the particles thereby eliminating any excess stretching or tearing of the seal while also preventing particle progression across the entire seal contact band. Experimental results of Ayala confirmed that these textures did dramatically improve the wear life of the seal; however, the wear reduction mechanism was completely different. Finite element analysis, time lapse video of the wear process, and laser induced fluorescence measurements of lubrication thickness identified the wear reduction mechanism as being strongly related to localized regions of high contact pressure and improved lubrication, both caused by the texture's effect on the seal's contact pressure profile.

Fiber composites have been utilized in many applications to improve mechanical properties such as modulus, fracture toughness, fatigue resistance, and wear resistance. Thus, the application of fiber-filled rubbers to seals was considered. However, a fundamental understanding of the wear behavior and a capability of modeling the basic stress-strain response of fiber-filled rubbers was recognized as being necessary for the material's proper application to seals. Therefore, a unit cell finite element model of a fiber-filled rubber was constructed and shown to properly capture the plane strain compression behavior of a polyurethane filled with glass fibers. The results of the unit cell model were also evaluated with the intention of drawing implications to the material's wear behavior.

Thesis Supervisor: Mary C. Boyce
Title: Associate Professor of Mechanical Engineering

Acknowledgments

I would first like to express my appreciation to Professor Boyce for all of her guidance and support during the past two years. She has been truly amazing in the way that she balanced so many different research projects, presentations, and teaching commitments while still finding the time to listen and talk to each one of her graduate students. I would like to personally thank her for being so generous with her time and for all of her understanding and advice. I have learned so much from her during our time together and am graduating with a true admiration of her excellence and dedication.

This project would not have been possible without the generous support of Caterpillar, Inc. CAT was extremely supportive in providing the necessary data, equipment, and materials for the project, but more importantly, their perspectives and experience were quite essential during the course of this research. I would particularly like to thank Alan Dickey, Jerry Metz, Mark Kiesel, Anthony Friend, and Teresa Doonan for their discussions and assistance.

I would also like to express my thanks to Hugo Ayala and his advisor, Professor Hart. This project was truly a collaborative effort, and I have enjoyed working with and learning from both of them. In particular, I would like to acknowledge the fact that all of the seal experiments were performed by Hugo, and his hard work and patience provided the results which formed the basis of this research (Hugo, don't forget our time in Peoria!). Many thanks are also given to Teresa Doonan and Andrey Lo for their assistance in the finite element modeling. I apologize for the hectic schedule at the end of the term and am grateful for your hard work.

Without a doubt, the graduate students of the Mechanics and Materials group have made the past two years so enjoyable. I want to acknowledge all of the discussions and assistance that helped me so much in my research. In particular, I would like to thank Clarence and Jorgen for their discussions on polymers, and Alexis for her expertise with the SEM. I would also like to thank *everyone* in the group for their friendship, encouragement, and tennis over these 2 years! I would like to make special mention of the members of my class: Kevin (congratulations to you and Bonnie, eh!), Nick, Jorgen (M&M's soccer captain for life), and Vivianne and of all of the other members of this year's graduating class: Clarence, Manish, Srihari, Brian Gally, Alex, Ganti, and Hong! I would particularly like to extend my gratitude and best wishes to Nick and Clarence. Nick has been an incredible friend, and we seemed to have taken every step together all the way from identical classes to the all nighters at the end, while Clarence has been like a brother to me this past year with all of his advice, concern, and encouragement. Lastly, congratulations to Jorgen and Gu on being appointed system administrators! I'll miss all of you!

I would also like to mention *all* of my friends outside the research group to whom I wish the best of luck. Special wishes go to my roommates Raj, Aaron (my friends for all 6 years here!), and Sean; Temina and Neala for all of the talks, encouragement, and thesis breaks; Mike, Dan, Lloyd, and the whole Mad Cows team for making it to the elite 8; the MIT cycling team; Anna, Pradeep, Jay, and Gon. Best wishes and I'll truly miss all of you.

Lastly and most importantly, I wish to thank my loving parents and my brother. Without a doubt, you have all been so important to me and are such a large part of who I am. Though I seem to be growing older and more independent, I know that I wouldn't be able to get very far without your love and encouragement. I love you all.

Table of Contents

List of Figures

List of Tables

Chapter 1

Introduction

Seals are a "workhorse" component used in mechanical devices to perform any duties related to joint packing and sealing of fluids or gasses. Typically constructed from rubber or even leather, their use is ubiquitous, and yet actual sealing mechanisms and understandings of lubrication, friction, and wear are not well understood. As a consequence, the design of seals has been based on trial and error manipulation of geometry and material.

In this chapter, a complete introduction to seals is presented. Different types of seals and seal materials are described, and the issues of sealing, lubrication, and wear are discussed. A specific type of seal, an undercarriage track joint seal, is then introduced. Reasons for researching ways to improve the life of these seals are motivated, and finally, an outline of the thesis is provided.

1.1 Types of Seals

A seal can be defined as a device that seals a gap or which makes a joint "fluid-tight" [1]. The fluid in this case can really be either liquid or gaseous. Seals are divided into two primary categories: static or dynamic. The primary difference between these two categories is that dynamic seals perform their function between two surfaces which translate relative to each other, whereas static seals operate between two fixed surfaces.

Static seals are quite diverse and are manufactured in an extremely large variety of shapes and sizes. Examples include gaskets and seal rings, and static seals are simply categorized as such. They are further described by their material composition and construction. Dynamic seals are generally divided into either clearance seals or contact seals. Clearance seals do not actually contact their mating surface. Conversely, contact seals are deformed directly against a mating surface to create rubbing contact.

Contact seals are further classified as either compression seals or pressure energized seals. The contact pressure of a compression seal is derived solely from the compression of the seal material against its mating surface. Pressure-energized seals, however, benefit from a contact pressure that is the result of a pre-load combined with an additional contribution from a pressurized fluid acting on one side of the seal. The pressurized fluid further deforms the seal, thus increasing the contact pressure. An example of a pre-load arrangement is an interference fit in which an O-ring sits in a groove.

Seals are quite often utilized in shaft applications. These shafts may be rotating or translating and can be found in automobiles, washing machines, or just about any mechanical device. Radial shaft seals fit around a shaft, and their sealing surface is located on the inner diameter of the seal. Its mating surface is then the outer diameter of the shaft. In contrast, face seals mate with a plane that is perpendicular to the shaft. Mechanical face seals use mechanical means such as steel springs to provide and maintain the contact pressure.

1.2 Sealing Mechanism

Seals have been used in industry for many years; however, the sealing mechanism is not well understood. Horve notes in particular that elastomeric lip seals have been in use since the 1940's, but seal design and processing are still largely the result of trial and error [2]. In this section, the common principles associated with sealing as outlined in the "Seals and Sealing Handbook" by Brown [1] are described.

Static seals have one sole purpose which is to prevent fluid leakage. They are therefore often called zero-leakage seals. Sealing is accomplished by creating a load between the seal and its mating surface through an interference fit which deforms the material of the seal. The contact pressure generated by this compression is then maintained by the stored

elastic strain energy of the material. Thus, any stress relaxation of the material itself, possibly due to thermal expansion, may compromise the performance of the seal.

In contrast, there are two competing goals which complicate the issue of loading dynamic seals. In order to prevent fluid loss, a high contact pressure is required; however, high pressures inevitably result in increased friction and wear. Typically, engineers choose to load dynamic seals with the minimum contact pressure necessary to prevent leakage. This minimum pressure can still be considerable, however, and frictional effects are amplified at low sliding velocities, especially during initial motion or a reversal of motion. Therefore, lubrication plays an especially important role in dynamic seals. Low coefficients of friction of the material should also be considered, but a successful dynamic seal may be described as one which allows a lubricating film to exist between the seal and mating surface while also preventing leakage [2].

1.3 Lubrication

The issue of lubrication introduces an additional complexity to sealing. Lubrication has been well studied in the literature, and many different types of lubricating conditions have been described such as hydrodynamic lubrication [2, 3, 4] and thin film lubrication [5, 6]. One common concern is clearly evident: surface roughness plays a vital role in lubrication behavior. This can be either surface roughness of the mating surface or of the seal itself.

In essence, micro-indentations on the surface allow pockets of oil or other lubricants to reside. Symons described the competing mechanisms of the surface roughness of a seal's mating surface [7]. If the surface is too smooth, it is difficult for a lubrication film to be maintained. As a result, adhesion and friction are increased, causing premature seal failure. If, however, the surface is too rough, the seal will simply be abraded. Thus, the ideal

surface roughness would provide a "happy" medium between these two types of seal failure.

The seal's mating surface is only one half of the seal system. Jagger noted that the surface roughness of the seal itself should be considered as well [8]. To this end, Potosky defines a number of parameters that can be used to describe a seal's entire topology [9]. However, there is currently little in the literature which considers the seal's topology under loading.

Under hydrodynamic lubrication conditions, Salant contends that micro-asperities on the material surface deform non-uniformly during motion, causing a reverse pumping action [4]. Horve's findings are similar. In pump rate measurement experiments, she observed that seals containing a large number of micro-asperities showed a much larger pump rate over seals with very few micro-asperities [2].

In all cases, the surface roughness of the mating surface and of the seal greatly determine the amount of lubrication that can exist and therefore directly influence the rate of wear.

1.4 Wear

Wear is influenced by a number of factors which have already been discussed. Lubrication, friction coefficient of the material, and operating conditions such as temperature and pressure all contribute to determining the life expectancy of a seal. A normal seal life for a hydraulic cylinder seal is roughly 4000 hours, while a lip type seal can expect 1000 hours according to Brown [1].

A well designed seal can exhibit excellent wear resistance; however, if the operating conditions include the presence of abrasive particles, the wear behavior is greatly altered. Because of the variety of environments in which seals operate, Tanoue, et al [10]; Golu-

biev and Gordeev [11]; and Hirabayashi, et al[12] all investigated wear in the presence of particles. Golubiev and Gordeev examined the wear of mechanical seals in abrasive slurries by monitoring the change in the height of the seal lip as a function of time. Their results exhibited three distinct periods of wear rate: break-in period, steady wear, and hazardous wear [11]. Tanoue, et al investigated the wear of seals operating in oil containing solid particles. Seal wear was measured for oil containing alundum and carbon particles ranging in size from 0.05 to 10 microns. They noted that the size of the solid particles which corresponded to the most seal wear was on the order of the film thickness between the two surfaces (approximately 0.3 microns) [10]. Their reasoning concluded that particles smaller than the length scale of the film thickness would simply pass through the film without causing wear, whereas particles that were larger than the film thickness would have difficulty penetrating the seal contact band. Thus, particles that were similar in length scale to the film thickness would have the greatest opportunity of penetrating and damaging the seal contact band.

1.5 Seal Materials

An ideal seal material would combine a low coefficient of friction with enough flexibility to conform completely to a mating surface. In addition, the material's mechanical properties would not vary significantly in different operating environments (corrosive chemicals, temperature changes, etc.).

A wide variety of materials are used in seals; however, the majority of seals are composed of synthetic rubber compounds. Materials which are too hard or stiff have difficulty conforming to irregularities in the mating surface. Therefore, rubbers are quite popular because of their inherent elasticity. Additionally, rubbers can be compounded differently for specific applications. Nitrile rubbers, for instance, can be compounded with less nitrile to improve low temperature properties. In other situations where resistance to petroleum

based oils is critical, the nitrile content can then be increased. Popular rubbers include nitriles (most popular synthetic rubber for seals), polyurethanes (excellent tear and abrasion resistance), polychloroprene (excellent resistance to weather ageing), and ethylene-propylene.

Thermoplastics are sometimes used to make seals as well. The most popular of this class of materials is PTFE. Thermoplastics are most often used as reinforcements for a seal assembly. In some cases, however, the material can actually be used in the seal lip. PTFE is an excellent choice for a seal lip material because of its low coefficient of friction, its resistance to chemicals, and its consistent behavior over a wide temperature range.

Other types of material used in seal applications are cemented carbides, leather, felt, and various fabrics used to reinforce seals. Cemented carbides are a type of powder metal composite that are used because of their excellent compressive strength and resistance to thermal and mechanical fatigue. Materials like leathers and felt are used because they can actually absorb and retain lubricants. While felts are used in light sealing applications, leather possesses excellent abrasion resistance and can be used between two relatively rough surfaces. Commonly used fabrics are cotton, nylon, and terylene.

1.6 Undercarriage Track Joint Seals

1.6.1 Seal Description and Operating Conditions

The type of seals under investigation in this thesis are found in the undercarriage of track type earth moving vehicles, as shown in figure 1.1 The track is made up of a number of links connected by pins, much like a bicycle chain. Each pin consists of a rod which fits into a bushing. The rod rotates within the bushing as the link progresses around the drive sprocket of the vehicle. The rod-bushing assembly is lubricated with oil, and seals as shown in figure 1.2 are used to prevent leakage of this very important lubricant. The whole pin assembly (rod, bushing, seal, and end caps) is press fit together, as shown in figure 1.3.

Figure 1.1: Track type earth moving vehicle. [13]

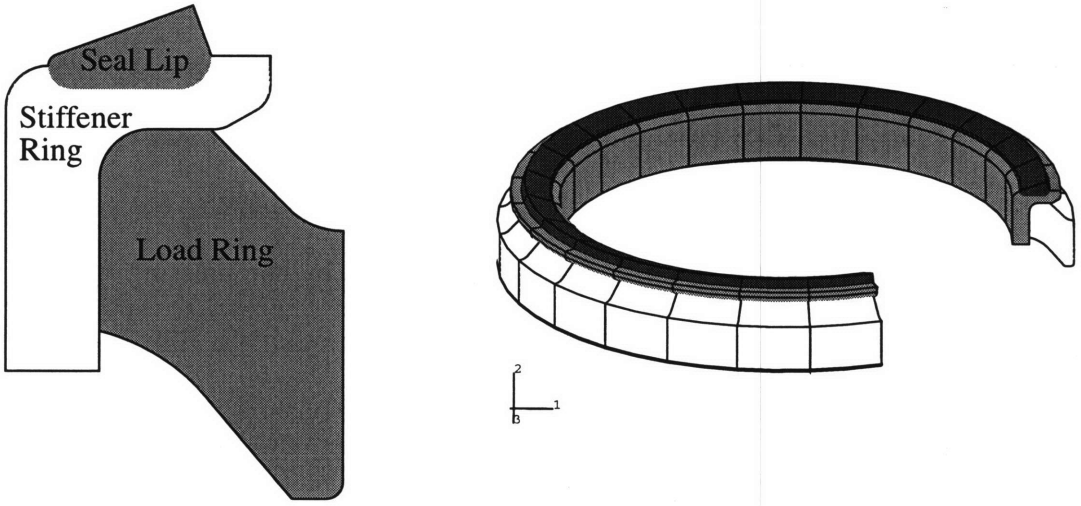

Figure 1.2: Undercarriage Track Joint Seal

The seal itself is actually an assembly made of three separate units: the seal lip, the stiffener ring, and the load ring. The seal lip is made of a filled polyurethane elastomer and is cured directly onto the glass filled polycarbonate stiffener ring during manufacturing. The seal lip is quite soft in comparison to the stiffener ring and is the portion of the seal that directly contacts the mating surface. The purpose of the stiffener ring is to transfer forces from the load ring to the seal lip. The load ring is made of a nitrile rubber and is used to create and maintain contact pressures much like the springs in mechanical face

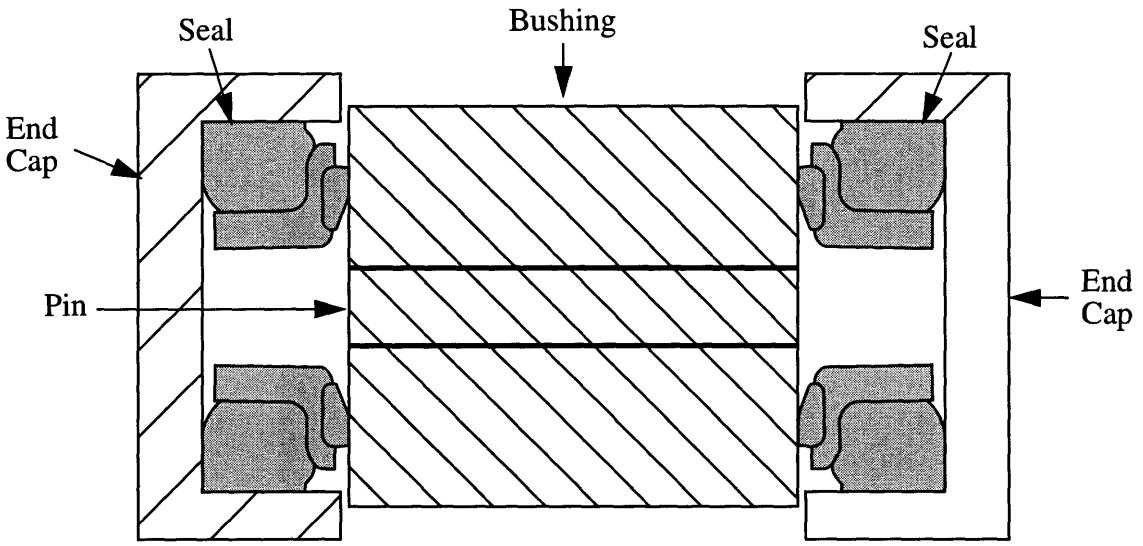

Figure 1.3: Pin Assembly (cross-sectional view). [14]

seals. The load ring is simply slipped around the stiffener ring and can rotate relative to the stiffener ring. However, ribs are placed onto the stiffener ring to discourage this motion.

Because the lip of these seals are pressed against a bushing surface which is a plane perpendicular to the shaft, these seals are considered to be face seals. The press fit assembly creates a high contact pressure on the lip of the seal by compressing the seal unit in both the axial and radial directions. In addition, the motion of the link around the drive sprocket clearly causes an oscillatory motion between the bushing and rod. Therefore, the seals are additionally classified as oscillating. This is distinctly different from rotary seals which spin in one direction continuously. The oscillation frequency is also quite low compared to the high speed of rotation of other seals.

Because these vehicles are used in a wide variety of environments, the expected life of the seals are often compromised by intrusive particles such as mud or sand. Once the seals are worn enough so that leakage occurs, the rods and bushings can be damaged. Replacing these components is quite expensive; however, replacing a set of seals requires a large amount of labor to disassemble the entire track and un-press each pin assembly. Addition-

ally, these vehicles usually operate continuously at project sites, and any time lost due to maintenance is quite costly.

In summary, the seals under investigation are face seals which (1) are press fit, creating a high initial contact pressure, (2) oscillate at low speeds with respect to the bushing, and (3) operate in the presence of abrasives such as sand or mud. The seals come in a variety of sizes corresponding to the size of the vehicle. The specific seal being examined in this document measures approximately 10 cm in diameter.

1.6.2 Research Motivation

In past designs, the pins of the track were always grabbed on only one side by the drive sprocket. As a result, the bushing became worn severely since there is no lubrication between the bushing and the sprocket. After approximately two to three thousand operation hours, the bushings had to be either replaced or simply rotated so that the unworn side could be used. This event was called a "bushing turn," and it allowed a maintenance period where the seals could be replaced at the same time since each pin had to be un-pressed.

More recently, new designs have prolonged the life of the bushings. Free-rotation systems allow the bushing to spin independently of the track links. This degree of freedom reduces friction and also wears the bushing evenly. Because the "bushing turn" was essentially eliminated, an opportunity to replace the seals was lost. If the vehicles had to be serviced due to seal failures, the advantages of the new free-rotation systems could not be fully realized. Thus, the maintenance period was now set by the seal life, and there was a clear need to improve the design of the track seals. Designing a seal with improved wear resistance would extend the length of time between maintenance services.

1.6.3 Summary of Initial Experimental Work

A first step towards understanding the seal life was reported in the S.M. thesis of Ayala [13]. In order to improve the seal design, an understanding of the deformation and wear of

the seal during operation was needed. Therefore, Ayala designed an apparatus which acted to measure the in-situ wear of the seal.

As shown in figure 1.4 below, a pair of rods were used to measure the height of the seal lip during experimentation. A complete pin assembly was used, and the bushing was rotated against the seal through an arc of 20 degrees at a speed of 30 cycles/second. The assembly was surrounded by a mud box which contained an abrasive mixture of fireclay, bank sand, Cabosyl, salt and water. Experiments were run for 0.5 million and 1 million cycles. The graphs shown below in figures 1.5 and 1.6 compare data for an experiment run with and without the abrasive slurry mixture. As clearly shown, wear was rather minimal for a seal operating in an environment free of abrasive particles. However, in the presence of mud, the wear behavior was much more dramatic. It is also interesting to note that all seals suffered permanent deformation on the order of 6% of the original seal height.

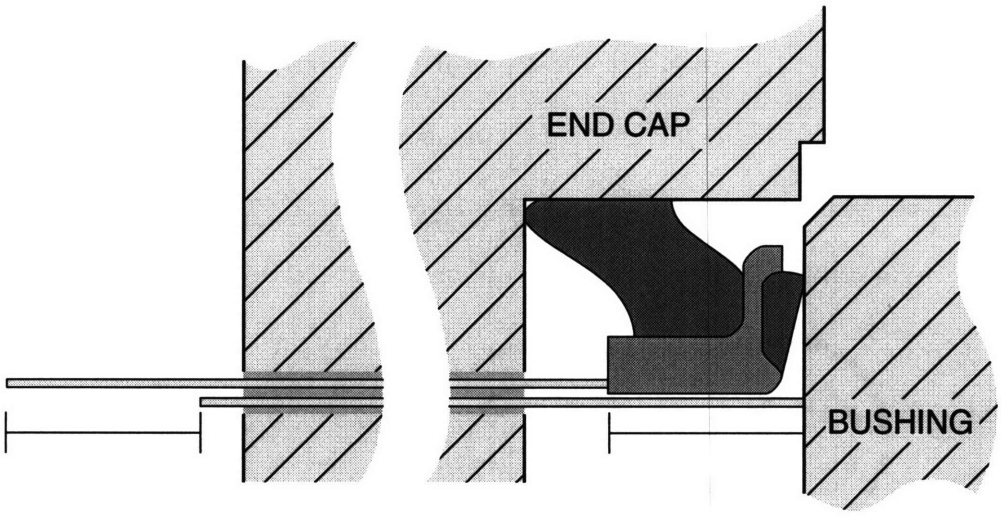

Figure 1.4: Rods used to measure the in-situ wear of the seal by measuring the height of the seal lip. [13]

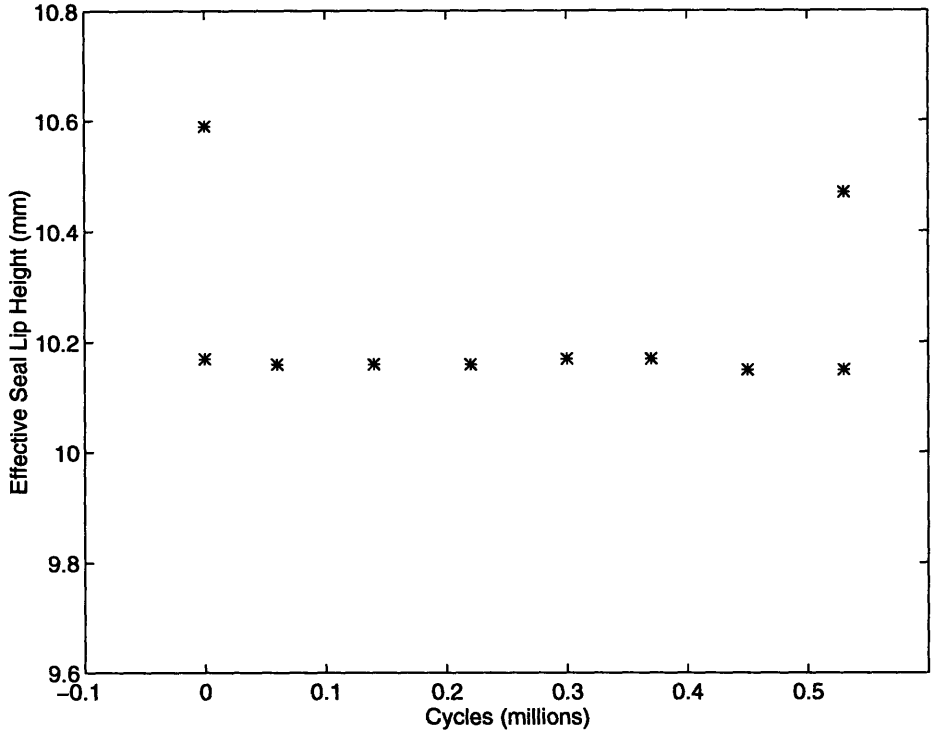

Figure 1.5: In-situ wear measurements of a seal operating in a "clean" environment. [13] The effective seal height is the measured difference of the 2 rods shown in figure 1.4.

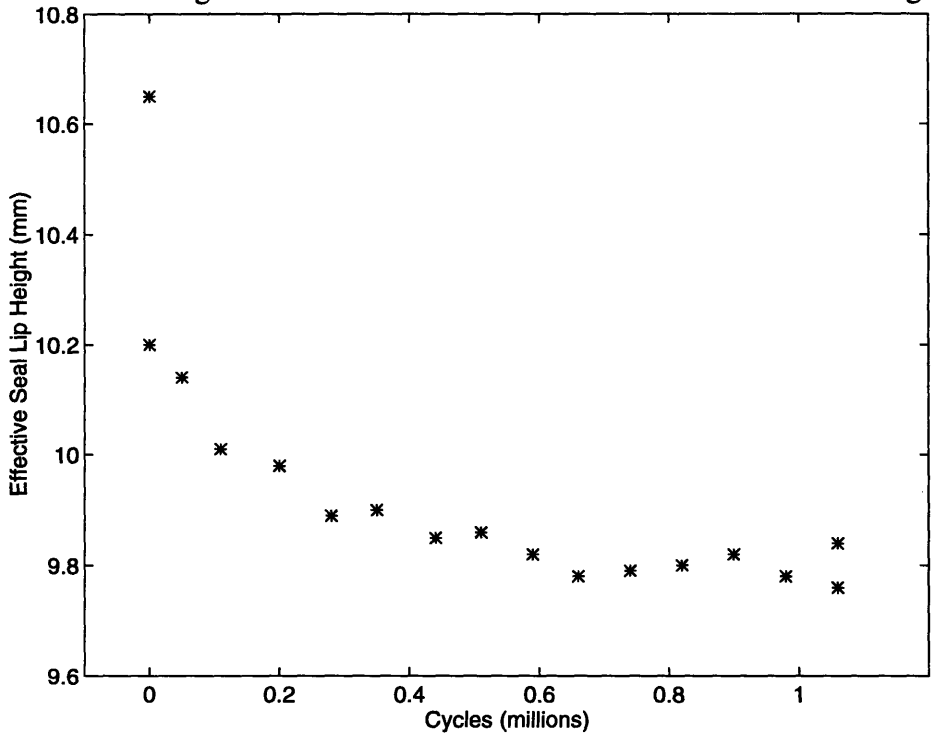

Figure 1.6: In-situ measurements of a seal operating in the presence of abrasive particles. [13] The effective seal height is the measured difference of the 2 rods shown in figure 1.4.

1.7 Thesis Outline

This thesis considers the re-design of a track seal for improved wear life. The wear life of the seal can be extended in two ways: through geometric changes to the shape of the seal and through the selection of new seal materials. Both of these types of modifications are explored and discussed.

However, before considering either of these changes, it is first necessary to establish the fundamental behavior of the seal. Chapter 2 discusses the loading conditions under which the seal operates and the probable mechanism for seal wear. Finite element modeling of all three components of the seal assembly provided the stress and strain distributions that the seal encounters, and experimental work performed by Ayala validated the model results and identified dirt penetration and abrasion as the primary cause of seal wear.

Having identified the wear mechanism, chapter 3 describes finite element simulations used to explore the micromechanics of seal wear through dirt abrasion. Specifically, these simulations modeled the interaction between the seal lip and abrasive particles. This chapter details the finite element simulation and then discusses the results. These results were extremely valuable as they generated ideas about how to improve the life of the seal by controlling the progression of particles once in the seal band.

One idea that came from the micromechanics simulations was the addition of textures to the seal surface in order to trap particles and thus control damage to the seal lip. Thus, in chapter 4, improving the life of the seal through geometric changes are explored via a parametric study of different seal surface textures. Finite element models of the texture are described, and their effects on the contact stress profile along the seal lip are discussed. Additionally, current experimental results are also presented which demonstrate the success of these surface textures in prolonging the wear life of the seal. Additionally, a discus-

sion is included which describes the texture's mechanism for wear reduction as concluded from considerations of both the finite element and experimental results.

Subsequent chapters of the thesis explore improving the wear life of the seal through a change in the seal lip material. Because of the many advantages provided by composite materials, fiber filled rubbers are considered as an alternate seal lip material. However, the proper application of such a material to the complex loadings that a seal encounters requires a thorough understanding of how fiber fillers affect the material response of the composite. In particular, the composite's wear and fatigue properties are of great importance for sealing applications.

Few models, however, provide a true understanding of how fiber filled rubbers wear. Such models are quite complicated because of the complex nature of rubber behavior. Thus, before even pursuing such a complicated model, a fundamental ability to model the stress-strain behavior of a fiber filled rubber composite was recognized as being extremely valuable. Thus, chapters 6 through 9 describe modeling the stress-strain behavior of a fiber filled rubber through a unit cell finite element model.

Chapter 6 presents experimental results for polyurethane filled with three levels of glass fibers in uniaxial and plane strain compression.

Chapter 7 describes material models for both the fiber and rubber matrix material. The complexities of modeling rubbery materials are also discussed in light of constitutive models that are commonly used to model rubbers.

Chapter 8 describes the simple unit cell finite element model of the fiber filled composite. Its results are shown to properly capture the behavior of fiber-filled rubbers, and with this confidence, stress and strain distributions within the unit cell are discussed in regards to certain wear and fatigue models.

Chapter 2

Fundamental Behavior of Seal

In this chapter, the fundamental behavior of the seal is discussed through the use of finite element modeling of the seal deformation and experimental results on seal wear. A finite element model is described for a two dimensional axisymmetric model of the entire seal assembly. This first model was important to understanding the loading and behavior of the seal system as well as the level of accuracy of the modeling. The results would help define the loading parameters for subsequent models and would identify needs for a more accurate understanding of the material behavior. ABAQUS was the commercial finite element package that was used.

Experiments [14, 15] involving time lapse video of the wear process and laser induced fluorescence (LIF) measurements of the lubrication film thickness underneath the seal lip provided further understandings of the seal system. The LIF measurements displayed a strong coupling with the contact stresses along the seal lip. In addition, the time lapse video of the in-situ wear of the seal identified the mechanism for wear as being dirt penetration and abrasion.

2.1 Finite Element Model of Track Seal

2.1.1 Material Models

The materials of the three seal components are all polymers. The polyurethane seal lip and nitrile load ring materials are both elastomeric in nature, and so a hyperelastic material model was used. For simplicity and direct comparison with the seal manufacturer's own models, the first order Mooney-Rivlin model [16] for rubber elasticity was chosen as a first approximation. This model requires two parameters, C_1 and C_2, used in the following expression of the material's strain energy:

$$W = C_1(I_1 - 3) + C_2(I_2 - 3) \tag{2.1}$$

The Mooney-Rivlin model is discussed in more detail in chapter 7. For the polyurethane seal lip material, C_1 was 3.1 MPa, and C_2 was 0.05 MPa, as specified by the manufacturer. For the nitrile load ring material, C_1 was 0.45 MPa, and C_2 was 0.05 MPa.

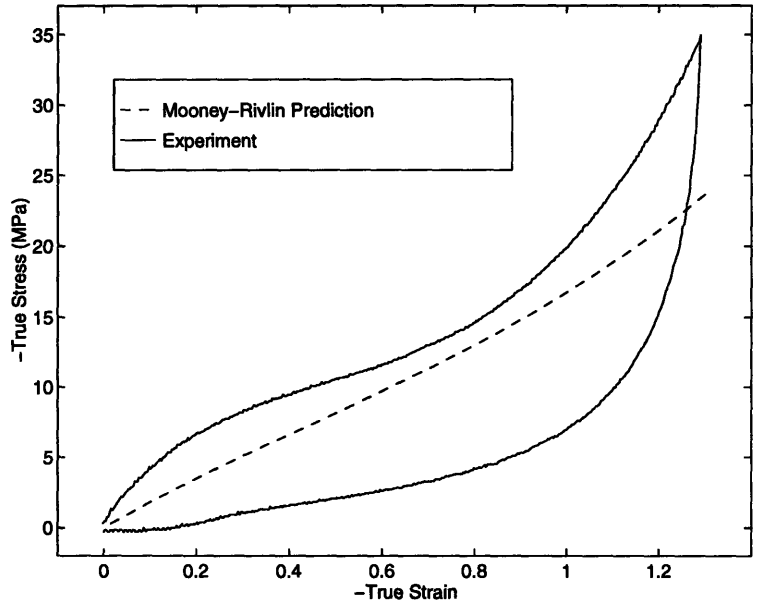

Figure 2.1: Mooney-Rivlin prediction of the polyurethane seal lip material in uniaxial compression.

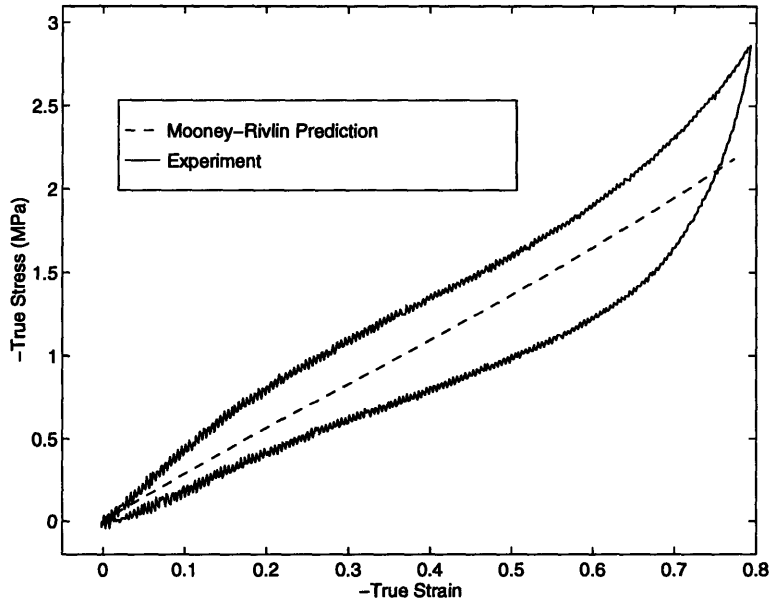

Figure 2.2: Mooney-Rivlin model prediction of the nitrile load ring material in uniaxial compression.

Figures 2.1 and 2.2 show a comparison between the experimental data and the Mooney-Rivlin model predictions in uniaxial compression. Clearly, the Mooney-Rivlin model provides a rather poor portrayal of the experimentally observed material behavior. The model parameters used for the predictions in figures 2.1 and 2.2 were supplied by the manufacturer of the seal, Caterpillar, Inc. These parameters were determined largely from comparisons between experimental data pertaining to the actual seal assembly and results from their own finite element model. In particular, load-displacement curves of the entire seal assembly, measurements of the seal lip contact band, and the overall deformed shape of the seal were used in order to approximate the material model parameters that would provide the best match with the seal assembly behavior. As will be discussed later in this chapter, these model parameters provide reasonable correlation with the experimental data pertaining to the seal; however, it is noted here that the Mooney-Rivlin predictions shown in figures 2.1 and 2.2 do not correspond very well with the experimental data pertaining to each material's actual behavior.

The glass filled polycarbonate is extremely stiff in comparison to the other two materials and was therefore expected to experience very little strain. Thus, the material was modeled as a linear elastic isotropic material with Young's Modulus, E, equal to 6.3 GPa, and a Poisson's ratio, ν, of 0.33.

2.1.2 Element Type

The seal naturally has geometric and loading symmetry in the plane perpendicular to its axis. In cylindrical coordinates, this symmetry is the r-θ plane. Additionally, the press fit into the pin assembly defines a symmetric displacement boundary condition. Thus, to utilize the symmetry and reduce the computational complexity of the model, two dimensional axisymmetric elements were used. The axisymmetric condition requires that there is no displacement in the angular direction, θ. Due to the symmetry, the r-θ and z-θ shear

stress and strains are zero.

Quadratic elements were selected because the geometry of the actual seal possesses many curved features as would the expected deformation of the seal. To better capture these curves, quadratic 8 node (four sided) elements were chosen.

Additionally, hybrid formulation elements were used. The material model being used for the seal lip and load ring is a rubber hyperelastic model, and incompressibility of the material is assumed. Rubbers are nearly incompressible materials, so this assumption is appropriate. However, incompressibility also implies that a displacement history cannot uniquely define the solution. For example, consider that a hydrostatic pressure can be applied to a body without changing the displacements. Conversely then, a small displacement change can produce extremely large changes in the pressure making a displacement based solution inappropriate numerically [17]. Satisfying the incompressibility condition can act to "lock" a mesh when displacement based elements are used. Therefore, a hybrid formulation is used in which the pressure is treated as an independently interpolated solution variable combined with the displacement solution variables. Thus, the elements used were two dimensional, axisymmetric, quadratic, hybrid formulation, 8 node elements, designated CAX8H in ABAQUS.

2.1.3 Modeling the Interface Between Seal Lip and Stiffener Ring

The seal lip is cured directly onto the stiffener ring during manufacturing. The intention of the design is that the seal lip and stiffener ring be perfectly bonded together so that there is no relative motion. Therefore, the seal lip and stiffener ring share common nodes along its interface. In this way, there can be no separation or motion between these two components in the model.

2.1.4 Modeling Interface Between Stiffener Ring and Load Ring

The load ring is simply slipped around the stiffener ring during seal assembly. While the load ring is permitted to rotate relative to the stiffener ring, this motion is discouraged by friction generated between the two components and by vertical ribs that are located on the outer diameter of the stiffener ring. Thus, two surfaces are defined: the outer edge of the stiffener ring and the inner surface of the load ring. Coulombic friction is modeled between the two surfaces with a friction coefficient, μ, equal to 0.5. In the Coulombic friction model, the two surfaces are not permitted to slide relative to each other so long as the shear stress magnitude is less than μ times the pressure between the two surfaces.

2.1.5 Modeling the Bushing and End Cap Contact

The seal assembly is constrained in its axial direction by the bushing and end cap. The bushing surface contacts the seal lip, and the end cap contacts the load ring on its bottom surface. Two rigid surfaces were therefore defined to model the bushing and the bottom of the end cap. Contact between the rigid surfaces and the seal were accomplished through the use of interface elements (IRS12).

2.1.6 Modeling Radial Contact Between the End Cap and Load Ring

The end cap is shaped in such a way that the seal sits in a pocket within the end cap, as shown in figure 1.2. The load ring is thus constrained in the radial direction by the end cap. This contact was modeled using a displacement boundary condition on all of the nodes lying on the outer diameter of the load ring.

2.1.7 Step Definitions

Two separate steps defined the load history of the seal in the finite element model. The first step modeled the radial compression caused by fitting the seal assembly into the end cap. The second step defined the compression in the seal's axial direction caused by the press-fit of the bushing.

Step 1 consisted of a displacement boundary condition on the nodes lying on the outer diameter of the load ring. With both rigid surfaces fixed, these nodes were displaced -0.45

mm in the radial direction. In step 2, the rigid surface representing the end cap was displaced 3.4 mm in the z (2) direction to simulate the full contact between the seal and bushing. This displacement results in a seal height of 11.3 mm after deformation.

2.2 Finite Element Model Results and Discussion

2.2.1 Overall Seal Results

Figures 2.3, 2.4, and 2.5 show the finite element mesh before loading, after step 1, and after step 2. The interface elements have been removed so that the deformation of the seal lip is clearer.

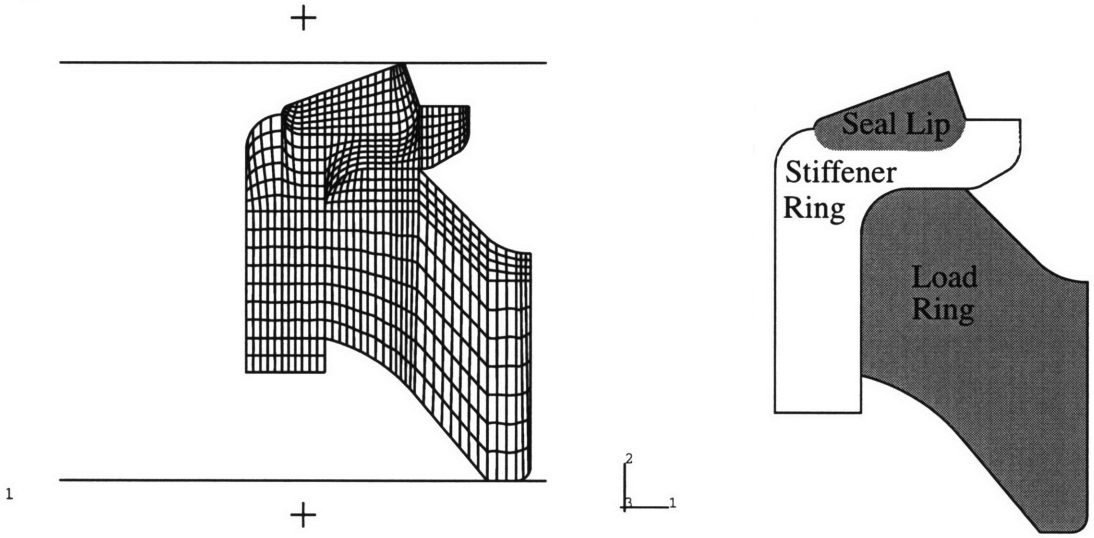

Figure 2.3: Finite element mesh shown before loading. A diagram of the seal is provided to help distinguish between the three seal components.

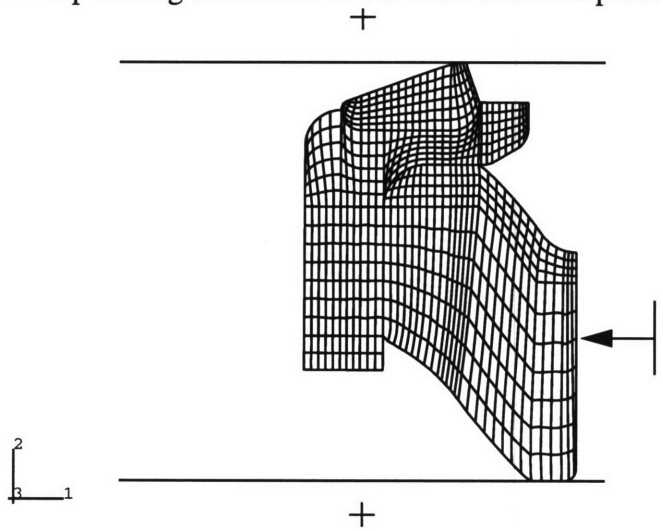

Figure 2.4: Finite element mesh shown after radial displacement applied (step 1). Deformation of the seal lip has already occurred because both rigid surfaces were fixed.

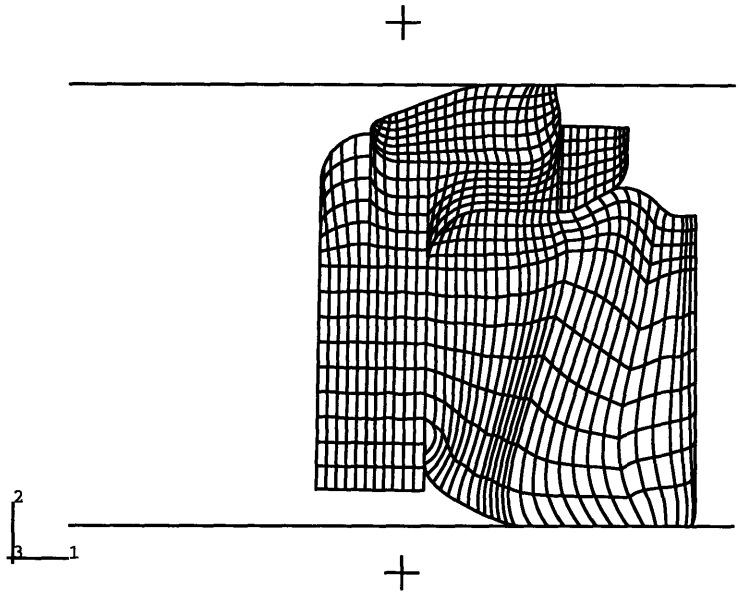

Figure 2.5: Finite element mesh shown after axial displacement applied (step 2).

The finite element model shows that the seal undergoes a complicated deformation state after it is has been press fit into the pin assembly. The seal lip was primarily strained in the axial direction, and as such, the maximum strains in the axial direction were found to be approximately -0.5. The load ring, in contrast, was mostly deformed in shear. Thus, shear strains were on the order of one in certain regions of the load ring. Because the load ring is constrained radially by the end cap, it was expected that the maximum radial strains occurred at value of -0.87. No significant deformation was found in the stiffener ring. Maximum strains in the body of the stiffener ring were only on the order of 1e-3. However, it was noticed that the stiffener ring was strained in the hoop direction. In the two-dimensional picture of the finite element model, the stiffener ring had rotated with respect to the axial direction after the load step had been completed. Thus, it was appropriate that the maximum hoop strains were found in the lower portion of the stiffener ring (approximately -0.03). A contour of the strains in the axial direction are shown in figure 2.6 as an example of the strain distribution throughout the seal assembly.

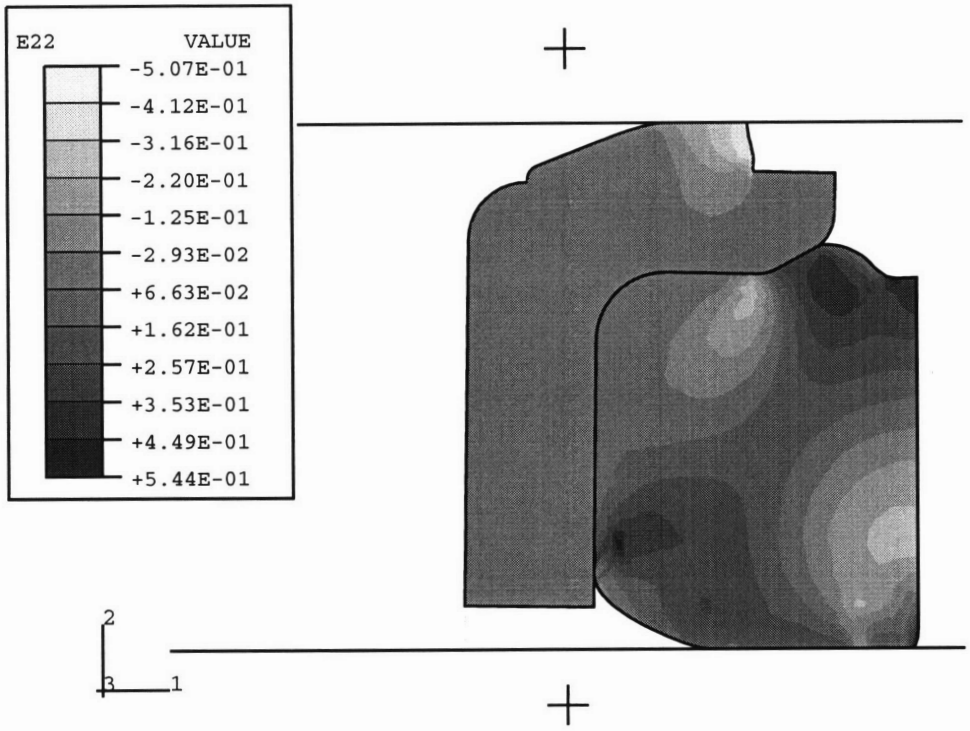

Figure 2.6: Axial strain contour of full seal assembly.

A pressure contour in figure 2.7 shows that the seal assembly was primarily under compressive stresses after step 2 was completed. However, certain regions at the interface between the seal lip and the stiffener ring were in tension. Additionally, large pressure concentrations were located at the interfaces between the seal components. For example, the maximum tensile stresses in the radial direction were 30 MPa at the interface between the seal lip and stiffener ring.

In the axial direction, the maximum stress occurred at the seal lip with a value of approximately -14 MPa. In the tangential, or hoop, direction, the maximum stress was found in the lower portion of the stiffener ring at a value of -37 MPa. The maximum compressive shear stress was -6.3 MPa at the interface between the stiffener ring and load ring, while the maximum tensile shear stress was 12 MPa located at the interface between the seal and stiffener ring.

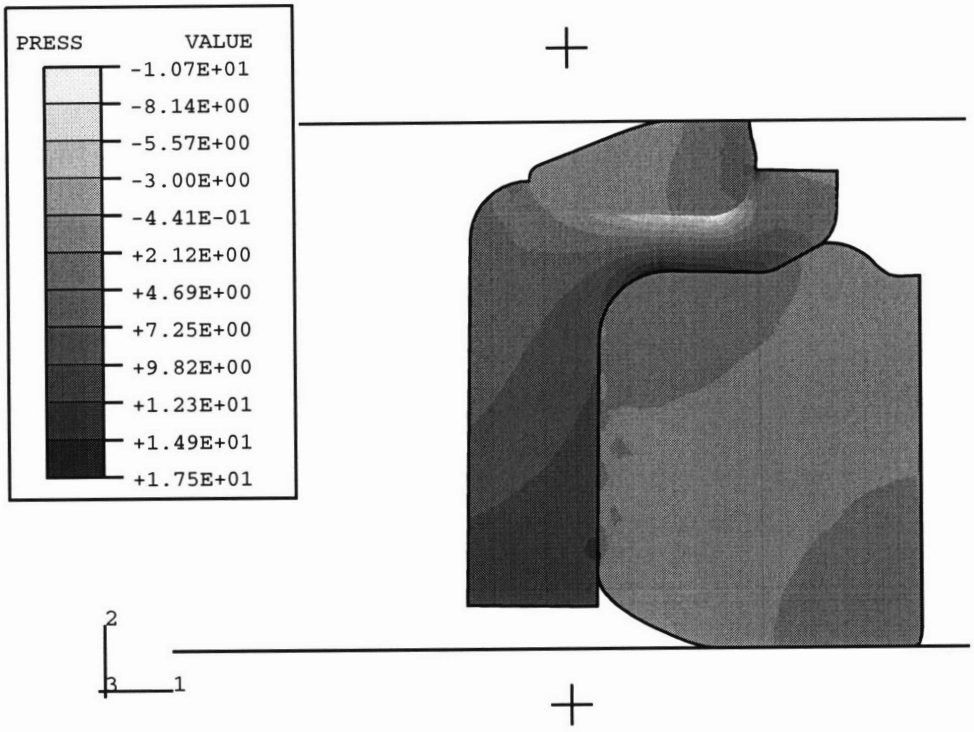

Figure 2.7: Pressure contour of the full seal assembly.

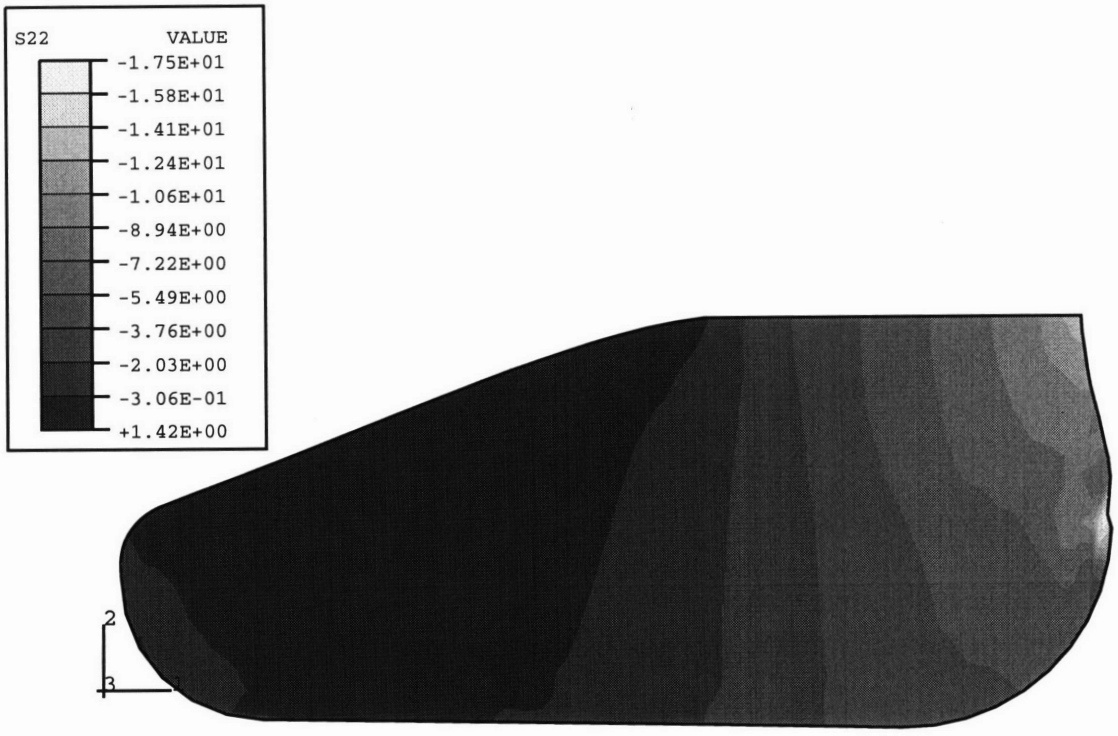

Figure 2.8: Axial stress contour of the seal lip.

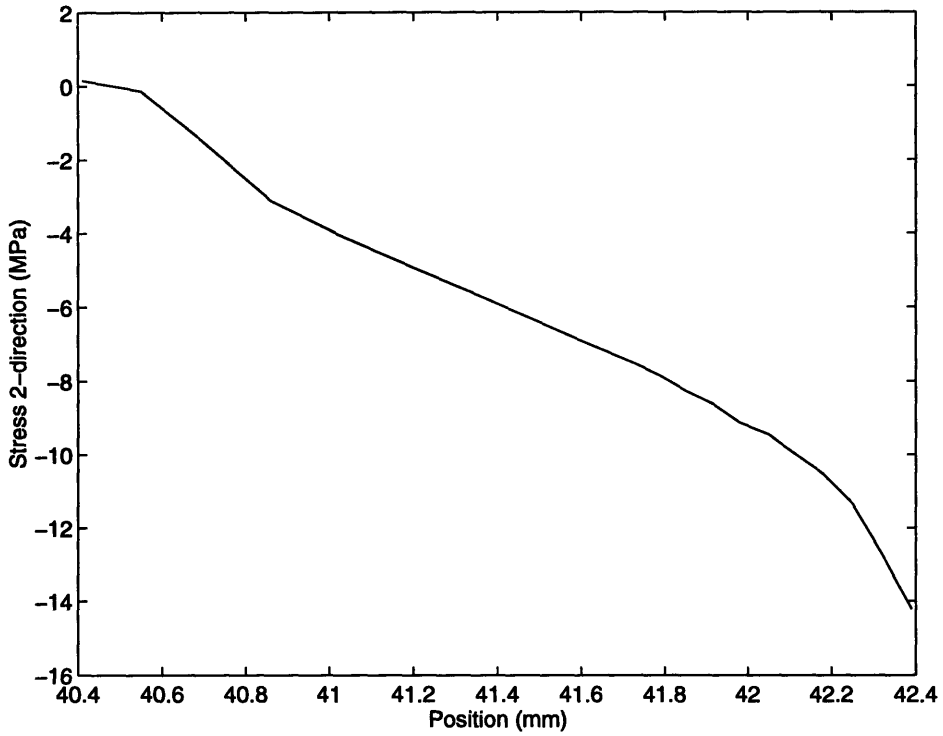

Figure 2.9: Axial stress profile along the seal lip contact band.

2.2.2 Seal Lip Results

The contact stresses in the region of the seal lip are of particular interest because they determine both the sealing and lubrication characteristics of the assembly. A close up of the stress in the axial direction for the seal lip is shown in figure 2.8. The axial direction stress distribution is shown since in the region of contact, this stress component represents the contact stress. As can be seen, the peak contact stress is located at the outer edge of the seal lip. A graph of the contact stress along the seal lip is shown in figure 2.9. The contact stress ranges from a maximum of -14 MPa on the outer edge of the seal to a minimum of -0.15 MPa on the inner edge.

2.2.3 Validation of Model

Validation of the finite element model was accomplished through comparisons with two different types of experimental data. The first set of data was a load displacement curve of the entire seal assembly. This data was obtained through the use of an Instron

1125 mechanical testing machine. The same information was obtained from the finite element model by recording the displacement of the moving rigid surface as well as the reaction force felt in the axial direction by that same surface. Figure 2.10 shows a plot of the experimental data and finite element results. The agreement is quite good; however the model seems to be consistently underpredicting the load throughout all compression displacements. The error is highest at approximately 23%, corresponding to an axial compression of approximately 2 mm.

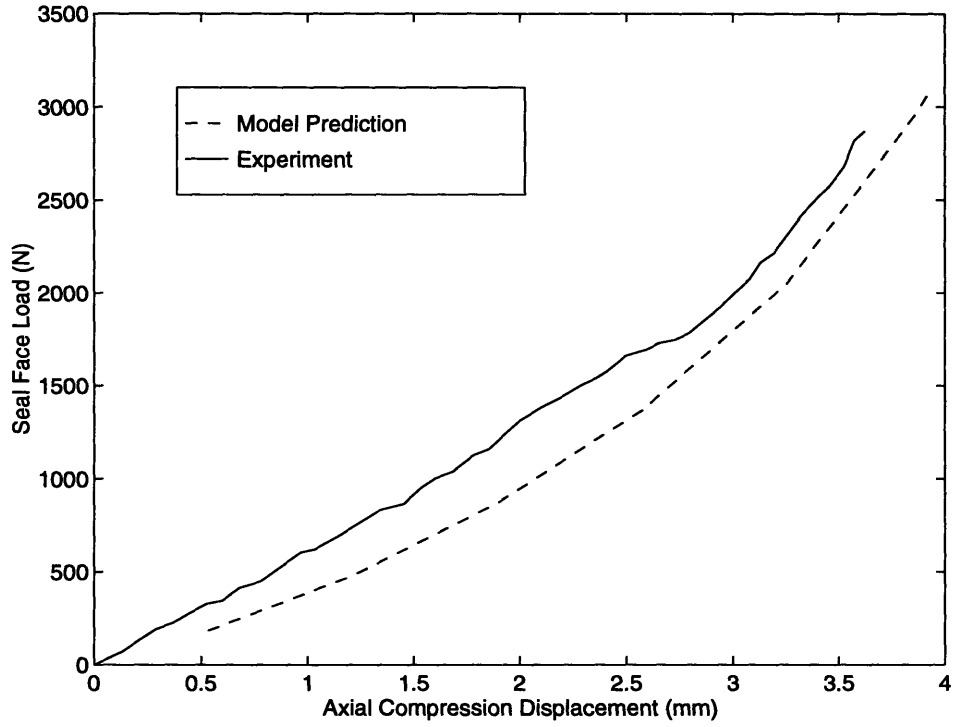

Figure 2.10: Load displacement behavior of the seal assembly.

The second set of experimental data used to validate the finite element results was a plot of the contact band width of the seal lip versus the applied load. During loading, the triangular tip of the seal is flattened against the bushing. The experimental data was obtained by using a clear plexiglass surface instead of a bushing. As the triangular tip is flattened, the width of the seal lip that is in contact can be measured through the plexiglass. The finite element model predictions and the experimental data are shown in figure

2.11. The finite element model consistently overpredicts the actual seal band width for axial compressions greater than 2.0 mm. The overprediction is as large as 23%at a compression of 3.3 mm.

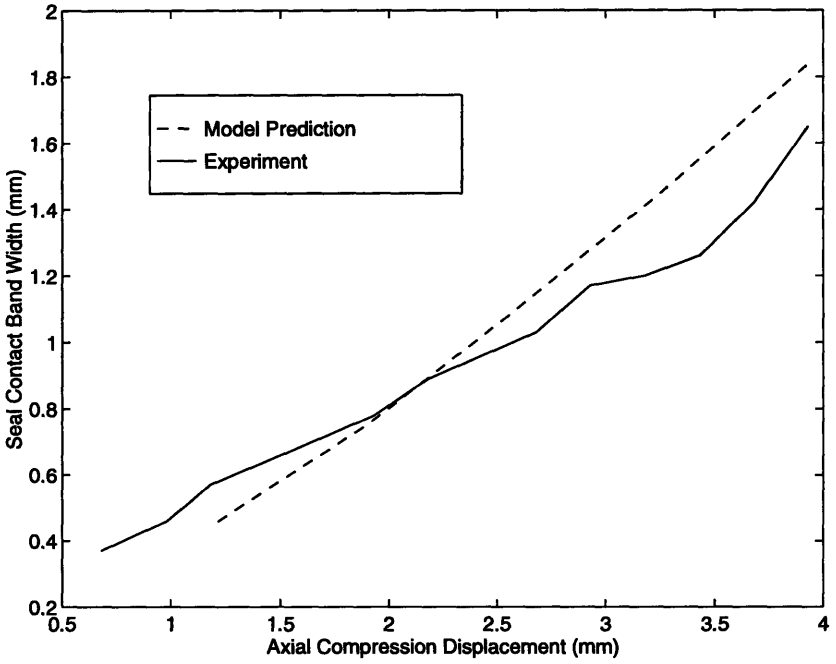

Figure 2.11: Seal lip contact band measurements. Experimental data courtesy of Tom White of Caterpillar, Inc.

Overall, the finite element model predictions are quite reasonable; however, the comparisons with the experimental data certainly point out areas which could use improvement. The model underpredicts the load-displacement behavior of the seal assembly and overpredicts the seal contact band width at higher axial compressions. In both cases, the error can be attributed directly to a material model that is too soft. Figure 2.1 shows that the Mooney-Rivlin prediction for the seal lip material is much softer than uniaxial compressions experiments would indicate. Additionally, the Mooney-Rivlin prediction for the nitrile load ring also underpredicts the experimental stress-strain results, as shown in figure 2.2.

Figure 2.12 shows the seal contact band width predictions for a finite element model which utilized two different material models for the seal lip and load ring material. The

seal lip material was modeled with an elastic-visco plastic material model, as proposed by Arruda and Boyce [18], while the nitrile load ring was modeled with the Arruda-Boyce 8 chain model of rubber elasticity [19]. These material models are discussed in detail in chapter 7. Figures 2.13 and 2.14 show the uniaxial compression comparisons between these two material models and the experimental results. These models are found to more accurately capture the experimentally obtained stress-strain behavior of the materials in comparison to the Mooney-Rivlin model. As shown in figure 2.12, the contact band width is consistently underpredicted throughout the axial compression range. At the higher compressions (3.1 to 3.9 mm) however, this error is quite acceptable. At full compression, the model underpredicts the width by less than 8%. In comparison, the error is as high as 43% at an axial compression of approximately 1.5 mm.

Using the Arruda-Boyce material models improved the contact band width predictions at high axial compressions. These improvements are largely due to the ability of the Arruda-Boyce models to correctly capture the stress-strain response of the materials. Additionally, because the Arruda-Boyce predictions are stiffer than the Mooney-Rivlin predictions, the load-displacement curve is naturally stiffer as well. Figure 2.15 shows the load-displacement curve resulting from use of the Arruda-Boyce models. The agreement is clearly much better now; however, the Arruda-Boyce predictions now overpredict the seal face loads at the higher axial compressions. The error is as high as 16% and can be attributed to two primary causes. First, there is compliance in the Instron testing machine. Thus, the experimental data should appear less stiff. Second, the experimental data shown in figures 2.13 and 2.14 are for material samples that are quite likely processed differently than the actual seal. For example, in the actual seal, it is quite possible that fillers in the seal lip material gain a preferential orientation due to the injection molding process and

the dimensions of the seal lip. Thus, the material properties would certainly differ from the experimental data shown in the figures.

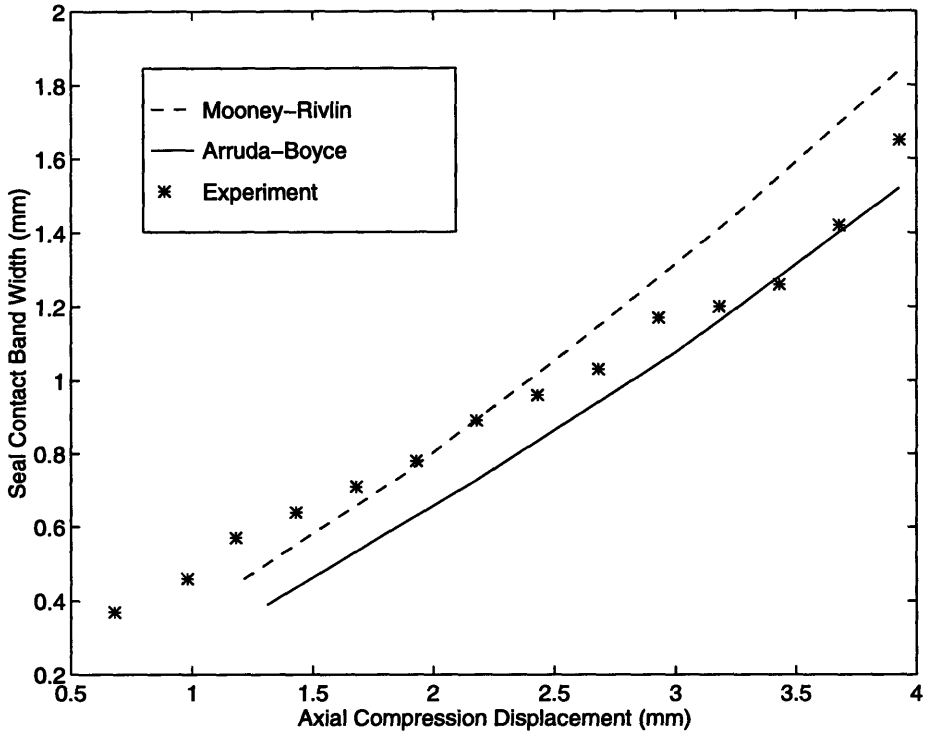

Figure 2.12: Mooney-Rivlin and Arruda-Boyce material model predictions of the seal contact band width. Experimental data courtesy of Tom White of Caterpillar, Inc.

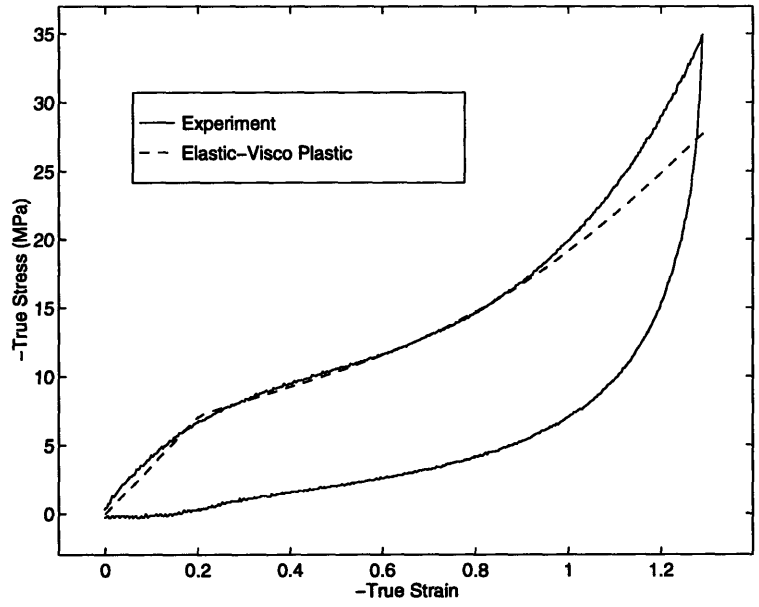

Figure 2.13: Uniaxial compression prediction of the seal lip material using the Arruda-Boyce elastic-visco plastic model. (E=35 MPa; ν=0.48; $\dot{\gamma}_o$=1.436e5s^{-1}; As=1.89e-19 J; s=6.5 MPa; CR=2.15 MPa; N=1.35)

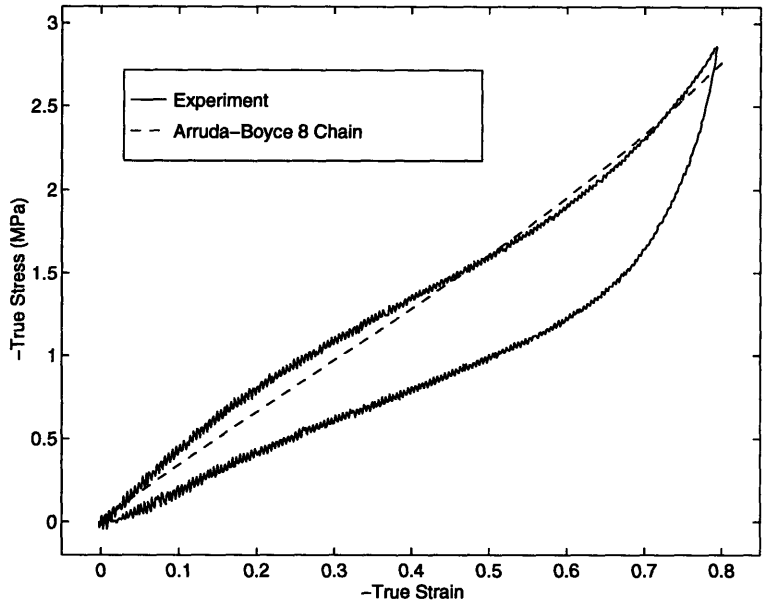

Figure 2.14: Uniaxial compression predictions of the load ring material using the Arruda-Boyce 8 chain model. (CR=0.99 MPa; N=3.9)

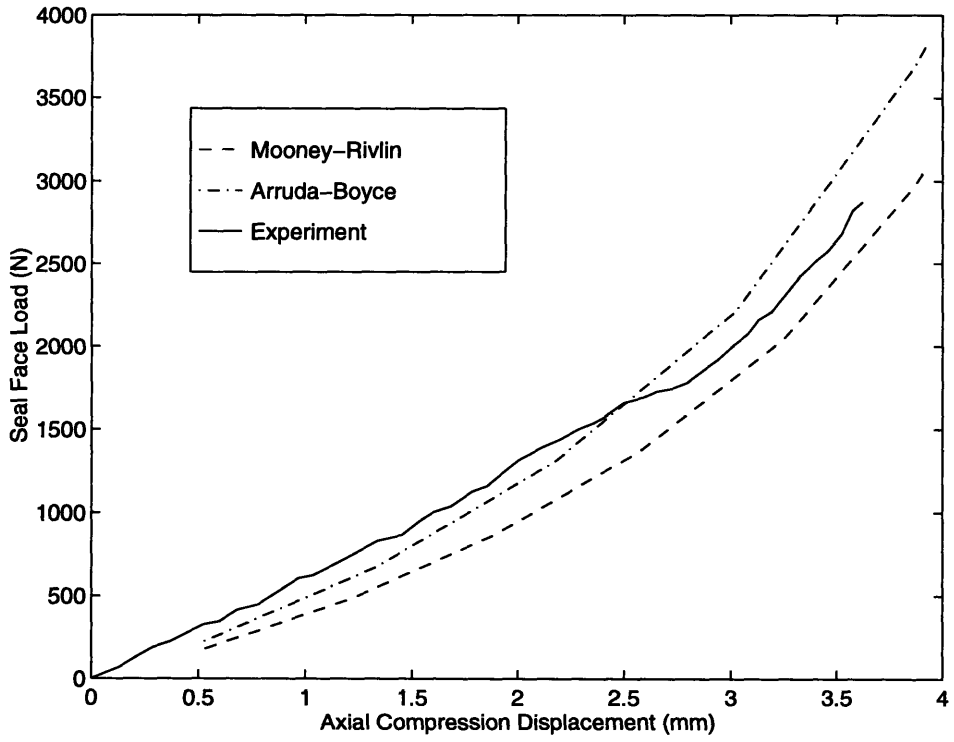

Figure 2.15: Mooney-Rivlin and Arruda-Boyce model predictions of the seal load-displacement response.

Thus, the Arruda-Boyce material models improved the correlations with both the seal contact band width data and the load-displacement behavior of the seal. Furthermore, these models correlate extremely well with the uniaxial compression data for the seal lip and load ring materials (figures 2.13 and 2.14). However, the load-displacement behavior is overpredicted at high axial compressions, and the contact band width is seriously underpredicted at low axial compressions. This result would seem to indicate that the actual seal lip materials and the experimental material samples exhibit slightly different mechanical properties. Again, an examination comparing how the seal was manufactured versus how material samples were prepared may provide insights into this difference. Additionally, it should be noted that the experimental data was acquired for new material samples only. In comparison, the experimental data displayed in figure 2.10 is for a single seal. Specifically, the same seal was loaded and unloaded for each data point of the curve. In light of the well known Mullins Effect [20] and of the permanent deformation as exhibited in the experimental data shown in figure 2.1, one would not expect the same material response for a new sample and for a sample being repeatedly loaded and unloaded. The issues surrounding the behavior of a material that has been previously loaded are further addressed and discussed in chapter 6.

It should also be noted that the elastic visco-plastic polymer material model requires a fair amount of computational time. In light of this, the Mooney-Rivlin approximations are accepted as being reasonable for now and are used in the simulations found in chapters 3 and 4 in order to provide a first order approximation that is computationally inexpensive. While fully realizing that the Mooney-Rivlin model does not accurately capture the seal's material behavior, particularly in different loading conditions [16], the sole intention in using the Mooney-Rivlin model in chapters 3 and 4 was to efficiently observe general

trends in the behavior of the seal system. Issues pertaining to the proper modeling of rubber and filled rubber behavior are the subject of chapters 6 through 8.

2.3 Experimental Results

2.3.1 Experimental Procedure

This section describes the more recent experimental work of Hugo M. Ayala [14, 15]. Previously, in-situ measurements of wear were made on a test apparatus that included the entire pin assembly, a means for oscillating the seal, and an abrasive mixture to simulate actual operating conditions. In these newer experiments, a glass surface was used instead of the steel bushing as the mating surface. While these two surfaces are not alike in features such as surface roughness, the glass provided a means for using time-lapse video to capture the entire wear process visually. A CCD camera in conjunction with a position encoder were able to record the wear of the seal as a function of cycles of operation. Test conditions, such as the oscillation frequency and amplitude, were identical except for the use of the glass surface. The experimental setup is shown in figure 2.16.

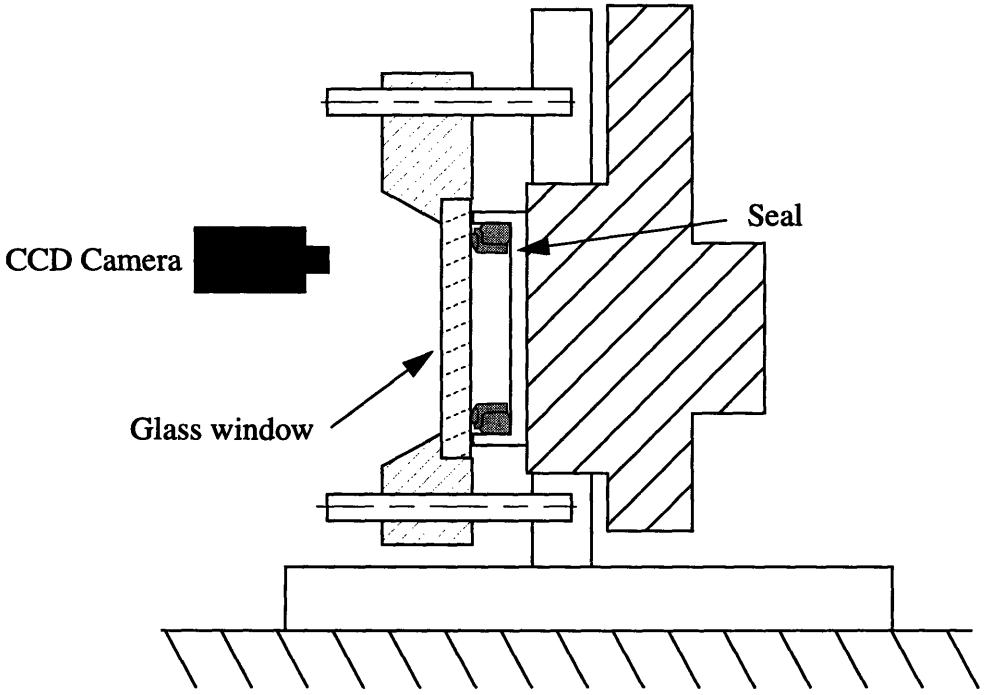

Figure 2.16: Experimental setup for time lapse video of the wear process. [14]

Experimental results revealed that the use of the glass surface accelerated wear. However, it is believed that the wear process is still accurately portrayed in the time lapse video and that conclusions drawn from wear measurements can be applied generally.

A second experimental technique was also used to aid the study of the seal wear process. As discussed in the first chapter, wear and lubrication are coupled quite strongly. Therefore, laser induced fluorescence was used to characterize the amount of lubrication in the seal contact band. This technique requires dissolving a dye into the lubrication oil and then using a laser to fluoresce the dye. Higher light intensities would then suggest the presence of more oil. This technique would prove to be extremely useful in studying the effect of textures on lubrication.

2.3.2 Time Lapse Video Experiments

In-situ wear measurements of a track seal were taken while a CCD camera recorded the wear process of the seal through the glass surface. An example of the CCD image of a track seal is shown in figure 2.17.

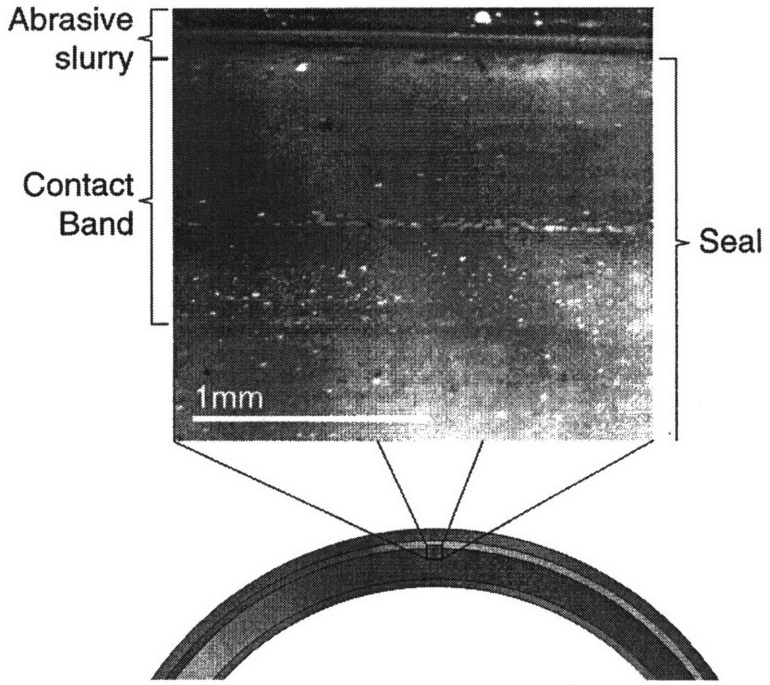

Figure 2.17: CCD image of a track seal. [14]

Figure 2.18 shows the in-situ wear measurements. In previous work [13], wear was measured by monitoring height differences in the seal lip. In the experiments discussed here, wear is monitored by direct observation of the seal contact band through the glass surface; thus, wear is measured as the ratio of the seal contact band that has been penetrated by dirt particles. Figure 2.18 shows that the wear rate was clearly divided into two distinct regions. From zero cycles to approximately 7000 cycles, there was essentially no penetration of dirt and therefore no wear. Beyond 7000 cycles, a period of aggressive wear was exhibited whereby a dirt front is observed to penetrate through the contact band. These split regions are similar to Golubiev and Gordeev's observations. They termed these two regions as the break-in period and the aggressive wear period.

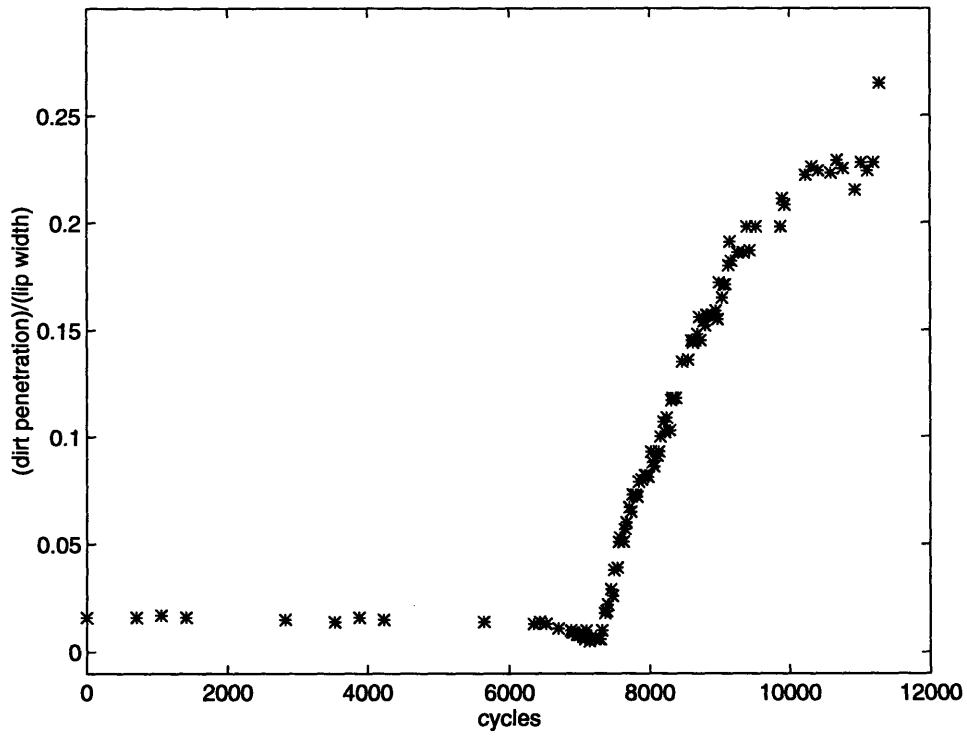

Figure 2.18: In-situ wear measurements of a track seal. [14]

Figure 2.19 provides an excellent visual interpretation of the wear plot. As clearly shown in the sequence of frames, a dirt front was formed at approximately 7000 cycles.

Once this front was formed, it proceeded to wear an extremely large portion of the seal contact band within 2000 cycles.

2.3.3 Laser Induced Fluorescence (LIF) Results

Figure 2.20 shows a picture of the seal lip as viewed with LIF. The white region at the top of the figure represents oil clinging to the edge of the seal. Below this region, dark bands represent thin films of oil trapped inside the seal contact band. As shown, the figure is darkest towards the outside of the seal. The bands become progressively lighter towards the center of the seal indicating the increase in oil film thickness.

2.3.4 Discussion

Comparison of the LIF measurements with the finite element results show that the area of lowest lubrication corresponds with the area of highest contact pressure. Figure 2.21 shows the contact stress distribution across the seal lip from the same viewpoint as the LIF

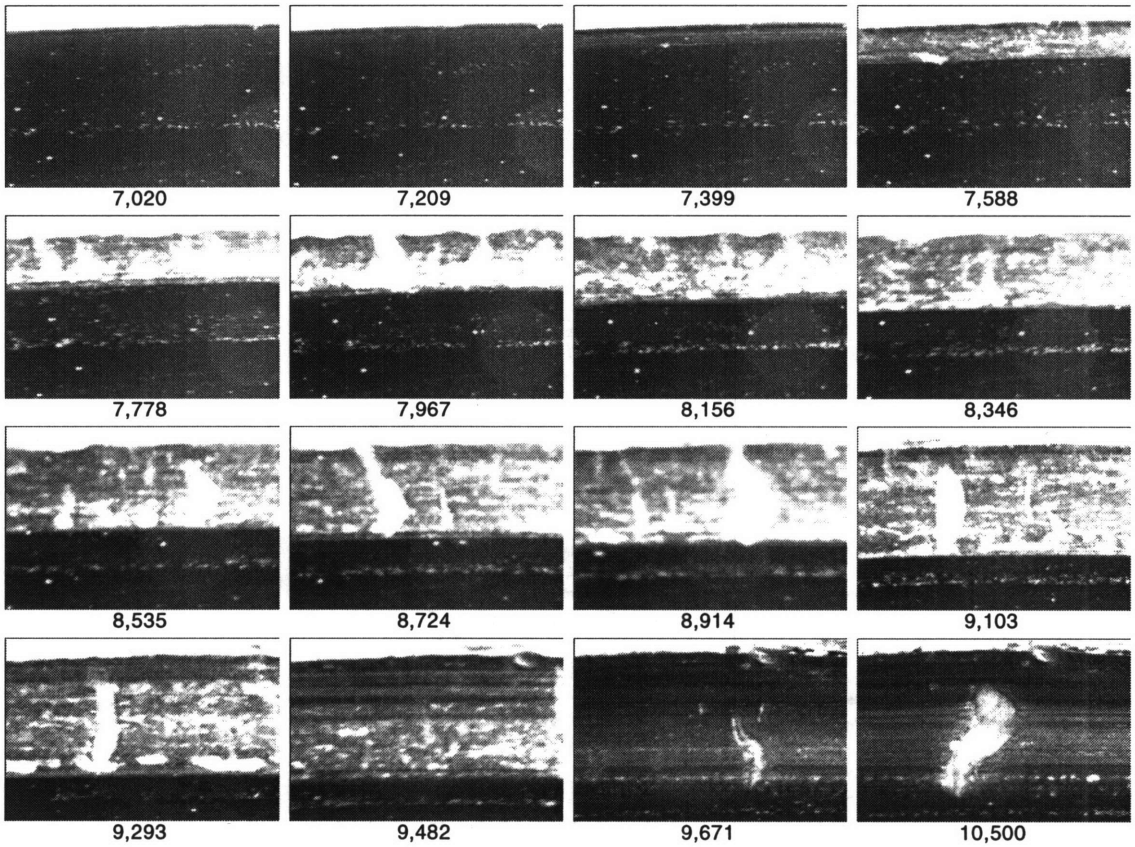

Figure 2.19: Advance of abrasive particles into the seal lip contact band. [14]

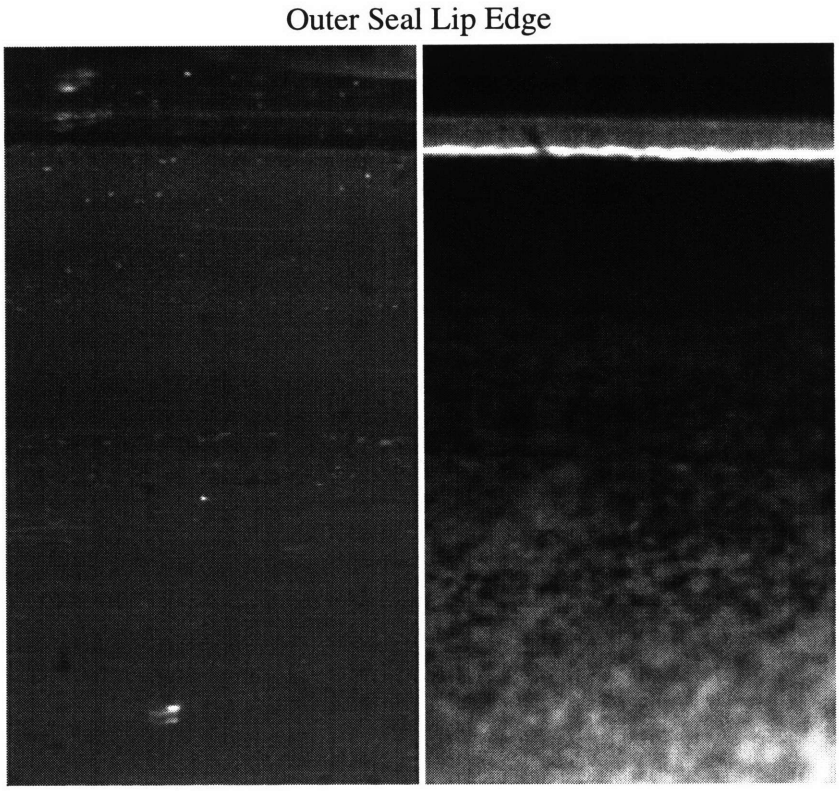

Figure 2.20: LIF image of a track seal lip.[14]

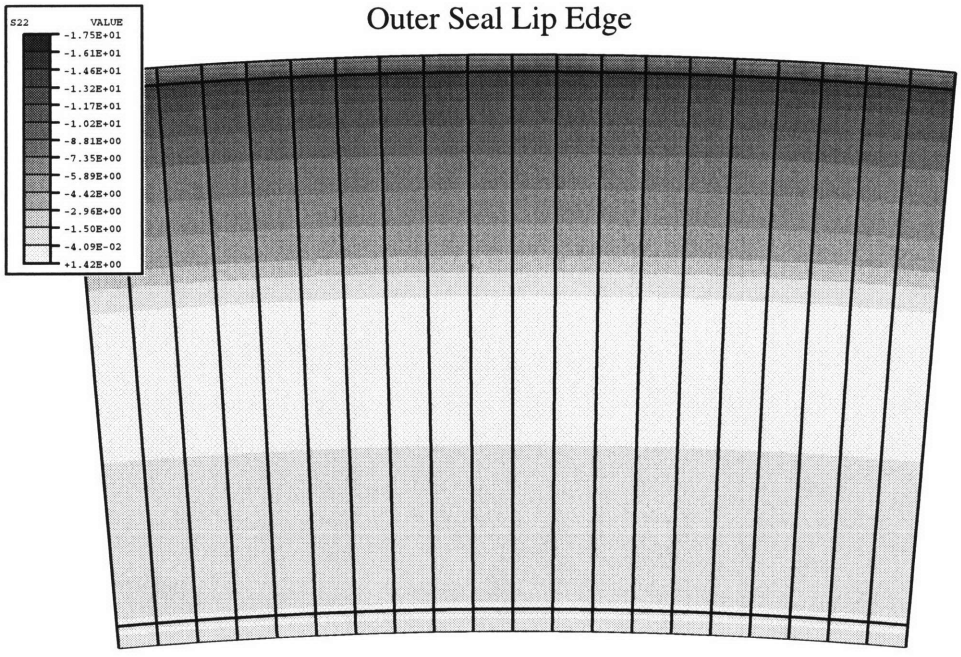

Figure 2.21: Finite element model of the seal lip showing the contact pressure distribution.

equipment. The comparison of figures 2.20 and 2.21 show that the amount of lubrication can be directly correlated to the contact stress. At the highest contact stress, the lubrication is thinnest, and the lubrication film increases as the contact stress is decreased. This correlation makes physical sense and is extremely useful since the contact stress profile along the seal contact band can be used directly to predict the lubrication distribution along the seal contact band.

Previously, it was shown that abrasive particles were the cause for the wear of the seal (see figures 1.5 and 1.6). The time lapse video of the wear process provided extremely useful information about *how* these abrasive particles wear the seal. The wear data of figure 2.18 coupled with the visualization of the wear process in figure 2.19 suggests that the wear of the seal can be divided into two main events. The first is the formation of a dirt front (at approximately 7000 cycles), and the second is the aggressive wear marked by the progression of the dirt front across the seal contact band (cycles 7000 to 9000).

Furthermore, these observations suggest that the life of the seal can be extended in two ways. The first is by preventing the formation of the dirt front, while the second is preventing the progression of the dirt front once it has formed inside the contact band.

Chapter 3

Micromechanisms of Dirt Abrasion

In the last section, it was shown that two events mark the wear of the seal by abrasive particles. The first event was the formation of a dirt front at the edge of the seal contact band. The second event is the actual abrasion of the seal which can be visualized by the dirt front progressing across the seal contact band. Two fundamental questions can be asked in regards to these two events. First, once the dirt front has been established, how do the particles enter the seal lip? Second, how do the particles wear the seal as they progress across the seal contact band?

In this chapter, finite element simulations related to the second question are presented in order to try and gain an understanding of the interactions between the seal lip and the abrasive particles at a micro level. The focus on the abrasion event is justified since the majority of seal wear occurs during this period. The results from these simulations offer information useful to models of fatigue and wear of rubbers, while at the same time, the understanding of the interactions provides a means to explore new seal designs which could improve the wear life of the seal.

3.1 Model Description

3.1.1 General Description and Purpose

During the abrasion process, abrasive particles are trapped beneath the bushing surface and the seal lip. The oscillatory motion of the seal then shears the seal lip over the bushing. Thus, fundamental modeling of the abrasion process is accomplished by compressing a "block" of the seal lip material over a particle, which is simply modeled as circular. After the block has been compressed an appropriate amount, the material is then displaced over the particle in a direction perpendicular to the compression. Figure 3.1 shows a diagram of this loading.

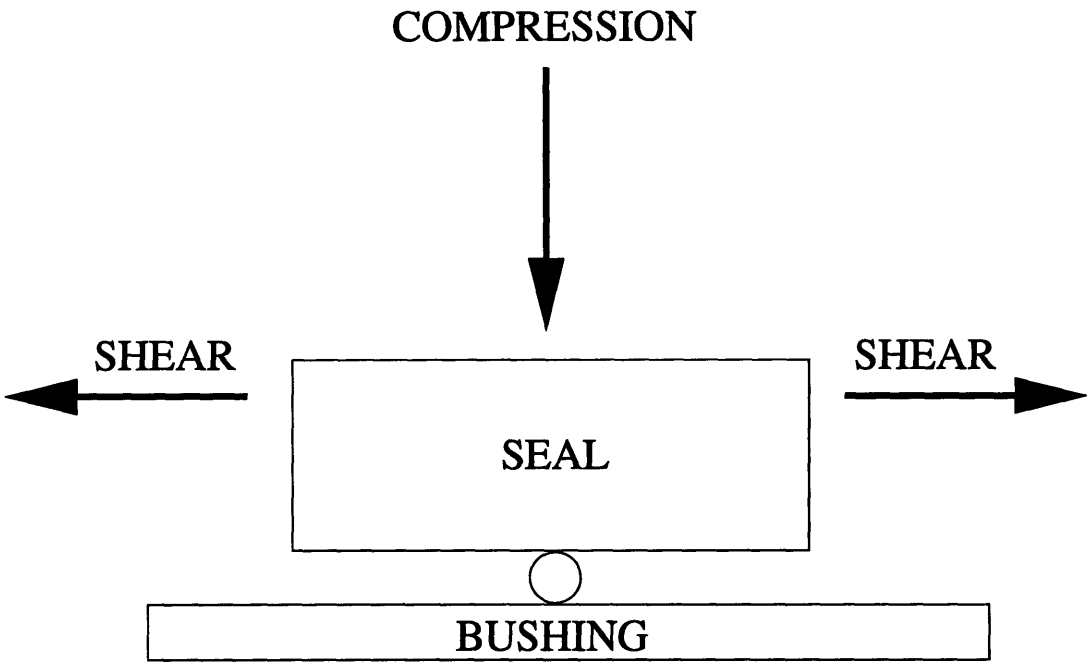

Figure 3.1: Schematic of compression and shearing over a particle.

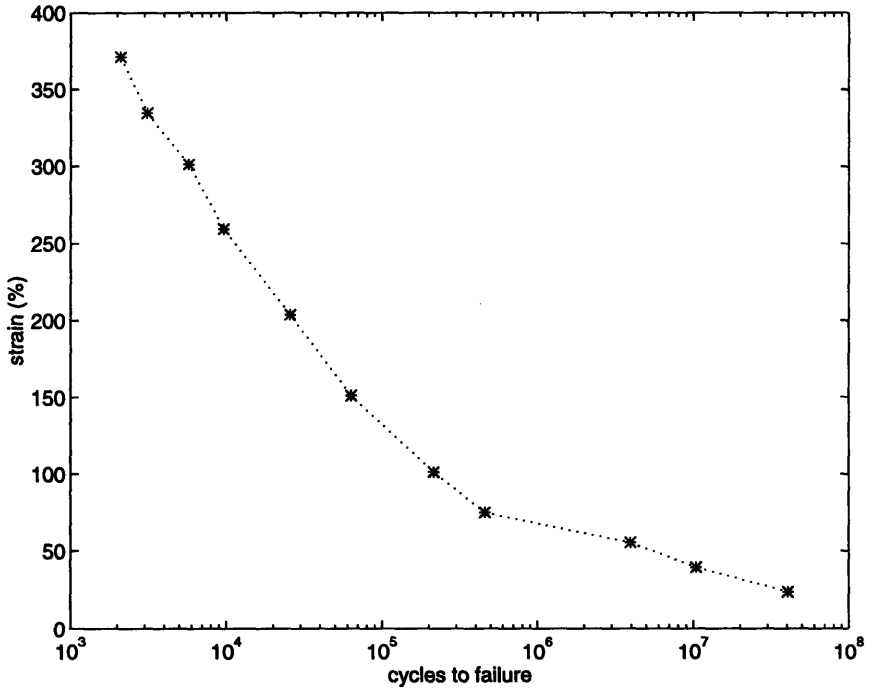

Figure 3.2: Strain-life curve for natural latex rubber vulcanizate in an ozone chamber [21].

The purpose of this simulation is to provide a strain or stress history that can be used to characterize the type of loadings that the seal lip might encounter during interactions with an abrasive particle. This is accomplished by selecting a point in the block of material and then tracking the magnitudes of strain and stress for that point during the compression and shearing steps.

Such information can then be related to models of stress and strain. Strain-life curves such as the one shown in figure 3.2 are often used to make a rather "rough" prediction of cycles to failure based on the strain amplitude of the cyclic loading. Other types of data include cut growth rate curves which are plotted against tear energies, as shown in figure 3.3. Most often, these curves are generated from tensile tests on a rectangular piece of rubber that has an initial cut placed in it. The tear energy is related to the geometry of the cut in the specimen, the strain energy density of the material at a specific stretch of the material, and a factor, k, which varies with stretch [22]. The data is used much like Paris' Law [23] is used to determine fatigue lives based on crack propagation rates. An empirical relationship between the cut growth rate and the tear energy T was found to be:

$$\frac{dc}{dn} = \frac{T^2}{G} \tag{3.1}$$

where dc/dn is the cut growth rate; T is the tear energy, and G is the rough cut growth constant of the rubber [24]. Because T is a function of the cut length, c, the total number of cycles to failure can be determined by integrating this relationship. T is a function of the strain energy density of the material, and in order to determine this strain energy density, one must integrate a stress-strain relationship for the material from an initial strain to a final strain during each load cycle. The results of the finite element simulations being described here could provide these strain measures. Additionally, wear models such as those suggested by Shallamach [25] relate wear of rubber to tear energies as well.

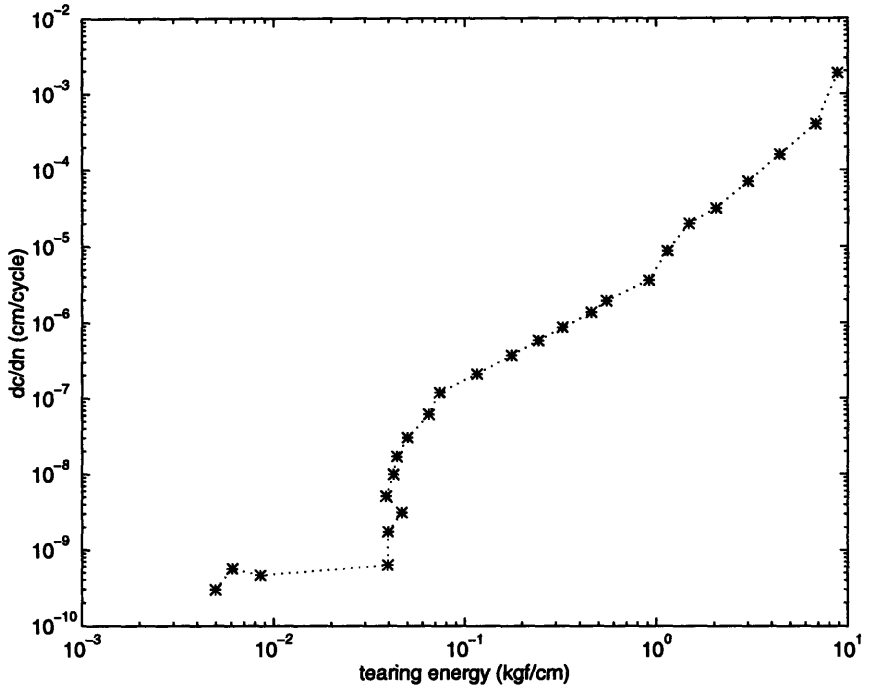

Figure 3.3: Fatigue crack propagation rate versus tearing energy for natural latex rubber gum vulcanizate. [21]

Other models of rubber wear also rely on information that these simulations can provide. Ratner proposes a model for the wear of rubber that is based on the macroscopic mechanical properties of the material [26]:

$$\frac{V}{L} = K\mu\frac{W}{H\sigma_b\varepsilon_b} \tag{3.2}$$

where V/L is the volume of worn material per unit length of sliding; K is a proportionality constant; μ is the friction coefficient; W is the load at contact; H is the indentation hardness of the material; σ_b is the tensile strength of the material; and ε_b is the elongation at break of the material. The finite element results could provide W for this expression.

In summary, models of fatigue and wear require some measure of the strain or stress that the material will encounter during interactions with the abrasive particle. Because micro-tearing has been the proposed mechanism for the fatigue and wear, regions of ten-

sile stress and strain are of particular interest when examining the results of these simulations.

3.1.2 Finite Element Model Description

The material block represents a portion of the seal lip contact band. Because seal lip band measurements averaged between 1.55 and 1.6 mm after being pressed into the pin assembly, the material block was dimensioned with a width of 1.6 mm. The height of 0.8 mm was arbitrary. For simplicity, the model was represented two dimensionally with plane strain elements. The plane strain condition restricts strains to be planar only.

The hybrid formulation was again necessary because as discussed previously, the material model used for this mock seal was the Mooney-Rivlin model. The same material parameters as those chosen for the seal lip in the two-dimensional axisymmetric model of the full seal assembly were used. Again, it is emphasized that the purpose of using this model was to observe the general trends of the seal system in a computationally efficient manner. As shown in chapter 2, the Mooney-Rivlin model does not accurately predict the actual seal material behavior, and the reader is referred to chapters 6 through 8 which discuss more accurate constitutive modeling. Additionally, quadratic elements were selected because of the usefulness of the mid-node in modeling contact with the particle. Because contact is modeled between nodes on a surface and because of the large size difference between the particle and material block, additional nodes were needed in the region near the particle so that the particle could not slip between two nodes. Quadratic elements provided an additional node without adding an additional element. Therefore, CPE8H elements were used. CPE6H elements were also used in the areas of mesh refinement because of the large deformation of the elements near the particle. The three sided elements permitted more deformation before convergence problems ended the simulations.

3.1.3 Modeling the Abrasive Particle and Bushing

For this set of simulations, abrasive mud or dirt particles were modeled as round rigid surfaces. The particles were 0.025 mm (25 microns) in diameter. Naturally, it was desirable to model particles with high hardness values since these would be most damaging to the seal. Thus, the material properties of silica were selected as a reference. Silica has a Young's Modulus as high as 69 GPa, while the seal lip material has a Young's Modulus of roughly 35 MPa. Thus, it was quite valid to simply model the particle as a rigid surface. In terms of computational time, this assumption was also quite beneficial.

The bushing is simply represented as a flat line in this two dimensional finite element model. Like the particle, the bushing surface was modeled as rigid.

3.1.4 Contact Modeling

This simulation involves three sets of contact since three separate entities exist in the model: the bushing surface, the particle, and the seal lip. Varying the type of contact between these three components effectively models different wear scenarios. Two different sets of contact conditions were modeled in these simulations.

The first case modeled friction between the bushing and seal and between the particle and seal only. No friction was modeled between the bushing and particle. Friction coefficients of 0.1 and 0.4 were used for the interactions between the bushing and seal and between the particle and seal respectively. These conditions represent a situation in which a particle becomes trapped within the seal lip and acts as a cutting edge towards the bushing.

In the second scenario, the particle was fixed to the bushing surface. Thus, a boundary condition was placed on the particle to restrict all displacements. Friction was only modeled between the bushing and seal with μ equal to 0.1. Friction was removed from between the seal and particle to facilitate the shearing of the material block over the particle. These

boundary conditions simulate a particle becoming embedded in the bushing surface and then abrading the seal surface.

3.1.5 Loading Conditions

The loading of the finite element model was accomplished in two steps. In the first step, a displacement boundary condition was placed on the upper row of nodes of the material block. These nodes were displaced towards the rigid surface 0.2 mm. In the absence of the abrasive particle, this amount of displacement caused a contact pressure of approximately 7 MPa along the surface of the material block. This value is approximately the same as the average contact pressure experienced by the seal lip in the axisymmetric model of the full seal assembly. In the second step, the same nodes were displaced in the positive x direction, perpendicular to the direction of compression.

3.2 Dirt Abrasion Simulation: Results

3.2.1 Compression: Frictionless Particle-Bushing Interaction

Figure 3.4 shows the deformed state of the finite element model before shearing had been implemented. The edges of the material block have deformed non-uniformly due to the friction interaction with the bushing surface. The material has deformed around the particle but has not completely enveloped it. Small gaps to the sides of the particle are shown in a close up view in figure 3.5. These gaps measure approximately 164 square microns.

Figure 3.6 shows the strain contour in the direction of compression. Strain contours show that the influence of the particle caused strain concentrations in a region measuring approximately 100 microns to each side and above the particle. In both the 1 and 2 directions, the maximum strain magnitudes were located just above the particle. In the 1-direction, the maximum strain magnitude was 0.85 located about 10 microns above the particle, while in the 2-direction, the maximum occurred at a value of -0.66 directly above the par-

ticle. Interestingly enough, strains in the direction of compression were not all compressive. On each side of the particle, a region of tensile strain is shown. The strain is approximately 0.4 in these regions. A contour of the shear strain is shown in figure 3.7. Maximum shear strains occurred diagonally above the particle at a magnitude of 1.09.

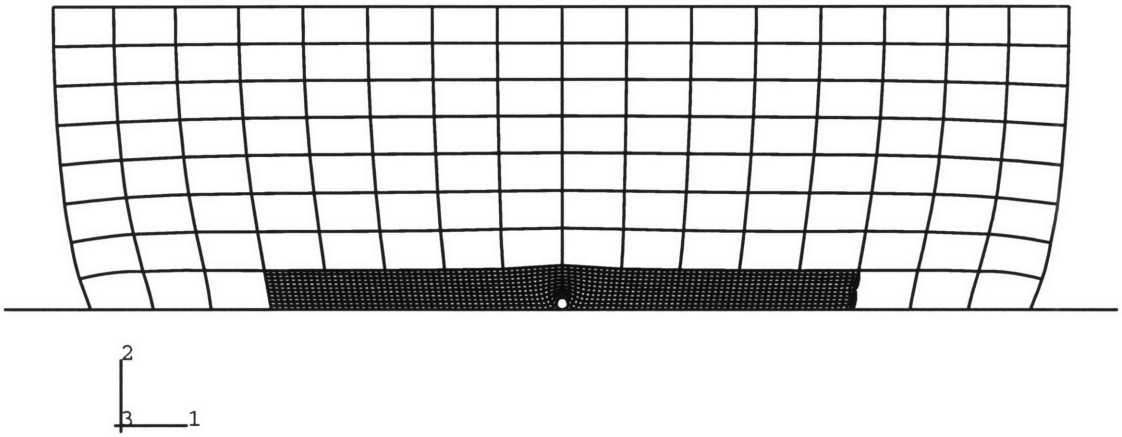

Figure 3.4: Deformed mesh after compression loading. (frictionless particle-bushing interaction)

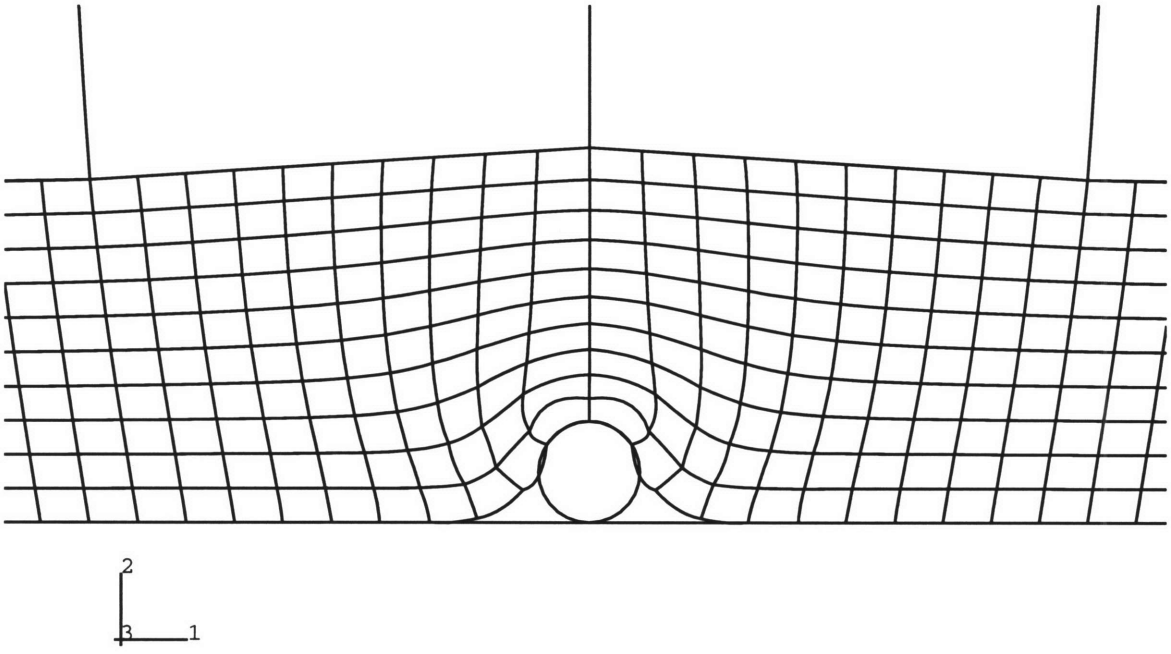

Figure 3.5: Detailed view near the abrasive particle after compression loading. (frictionless particle-bushing interaction)

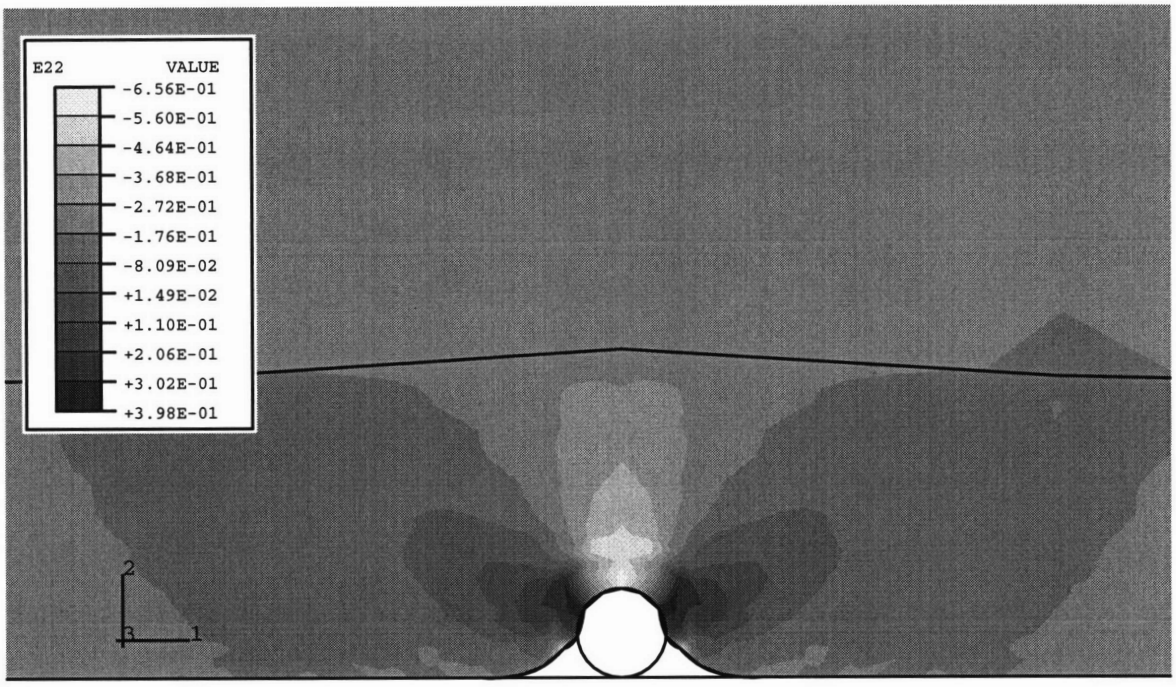

Figure 3.6: 2-direction strain contour after compression loading. (frictionless particle-bushing interaction)

The maximum stresses occurred directly above the particle in both the 1 and 2 directions. In the 1-direction, the maximum stress was -55 MPa, and in the 2-direction, the maximum was approximately -70 MPa. Maximum shear stresses were 13 MPa located in the same location as the shear strain maximums. The maximum compressive principal stress was -70 MPa directly above the particle, and the maximum tensile principal stresses were 5.7 MPa located at each side of the particle. Contours of the shear stress and 2-direction stress are shown in figures 3.8 and 3.9, respectively. Additionally, figure 3.10 shows the stress in the 2 direction along the bottom surface of the material block. A maximum stress peak occurs at center of the particle, and regions of tension are clearly shown to each side.

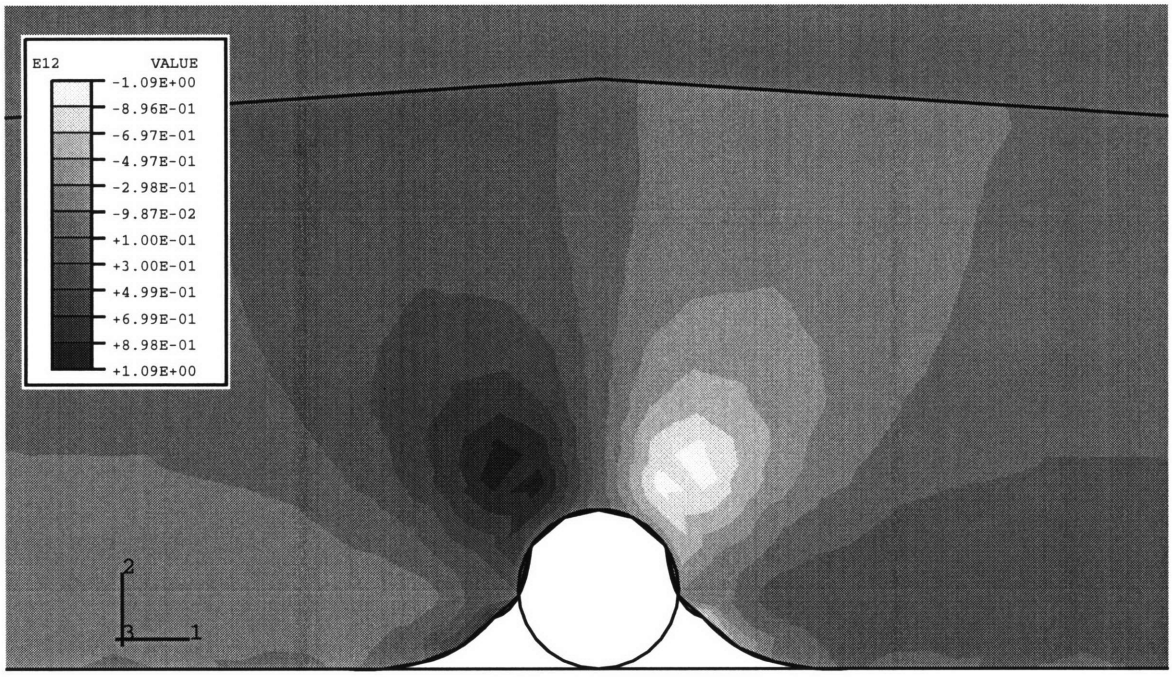

Figure 3.7: Shear strain contour after compression loading. (frictionless particle-bushing interaction)

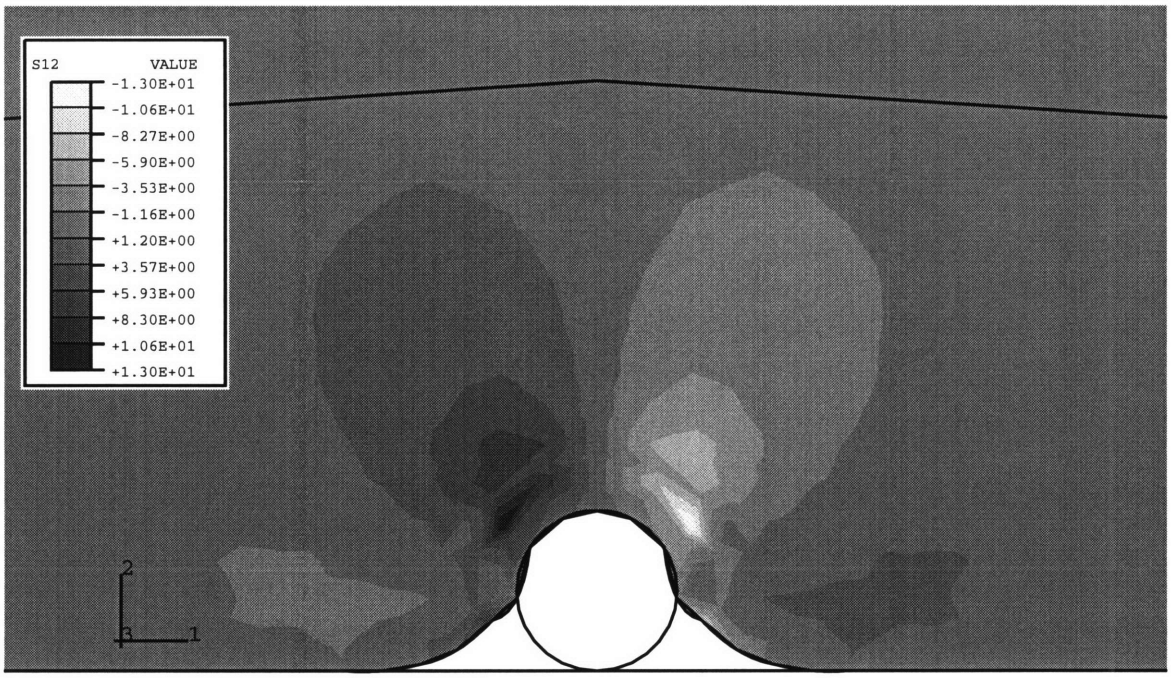

Figure 3.8: Shear stress contour after compression loading. (frictionless particle-bushing interaction)

Figure 3.9: 2-direction stress contour after compression loading. (frictionless particle-bushing interaction)

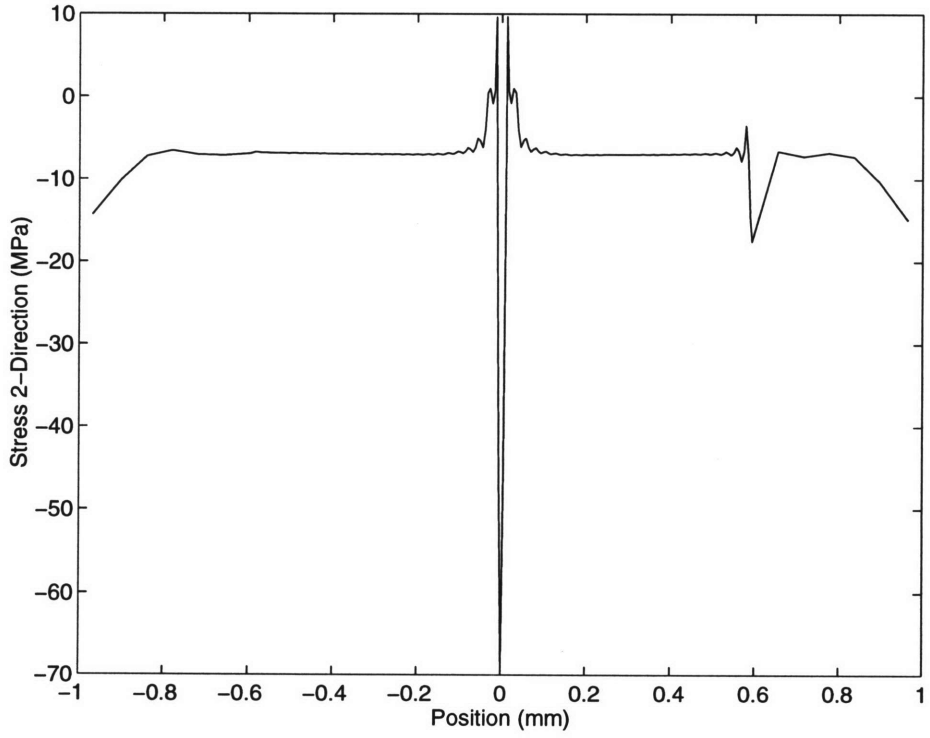

Figure 3.10: 2-direction stress profile along bottom surface of finite element mesh. (frictionless particle-bushing interaction)

3.2.2 Shearing: Frictionless Particle-Bushing Interaction

Figure 3.11 shows the deformation of the material block and particle during different stages of the shear loading. The upper row of nodes of the material block were displaced in the positive 1-direction a total of 0.5 mm. As shown in the figure, the particle was trapped within the material block and was dragged along.

Figure 3.12 shows a strain contour in the 2-direction after the full 0.5 mm of displacement. Clearly, the shearing action caused an asymmetry in the strain contour around the particle. In this particular contour, the trailing edge (the side of the particle opposite the direction of motion, in this case, the left side) of the particle has accumulated more strain than the leading edge. Additionally, a tiny opening has appeared between the top of the particle and the material block. The maximum strain in the 2-direction has increased to -1.47 above and on the leading edge of the particle, and the regions of tensile strain to the sides of the particle have increased their values to 0.51. Overall, the strains have been increased significantly. In the 1-direction, the maximum strain has increased to 1.29, and in the shear direction, the strains have increased to -1.21 on the leading edge of the particle and 1.46 on the trailing edge.

Similarly, the distribution of stresses became asymmetric, and stress magnitudes increased as well. The magnitude of the maximum stress in the 1-direction increased to -101 MPa, and the maximum stress in the 2-direction increased to -130 MPa. Maximum shear stresses increased to 16.7 MPa on the trailing edge of the particle and decreased to 11.4 MPa on the leading edge, and the maximum compressive and tensile principal stresses increased to -130 MPa and +7.7 MPa, respectively. A contour of the 1-direction stress is shown in figure 3.13, and a graph of the stress in the 2-direction along the surface of the material block is shown in figure 3.14. The general shape of the curve has remained

the same; however, the minimum and maximum values have changed during the displacement in the 1-direction.

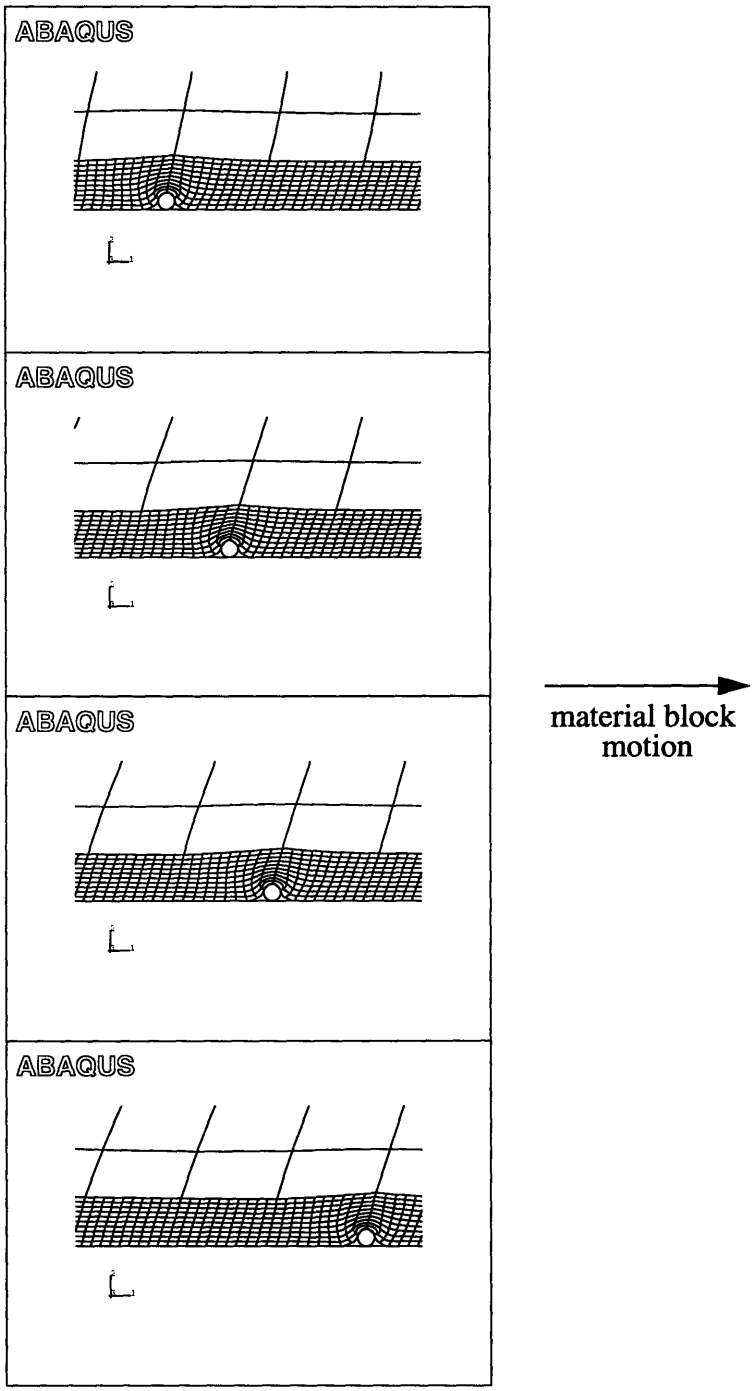

Figure 3.11: Deformed finite element mesh during incremental stages of shearing.

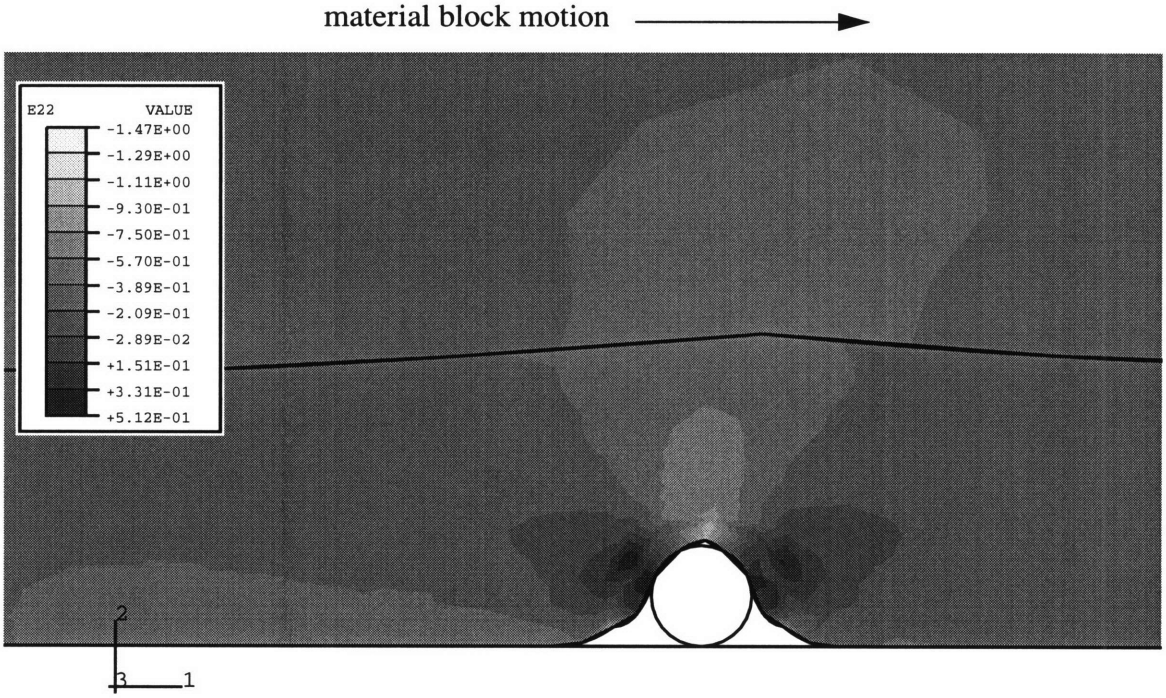

Figure 3.12: 2-direction strain contour after shearing. (frictionless particle-bushing interaction)

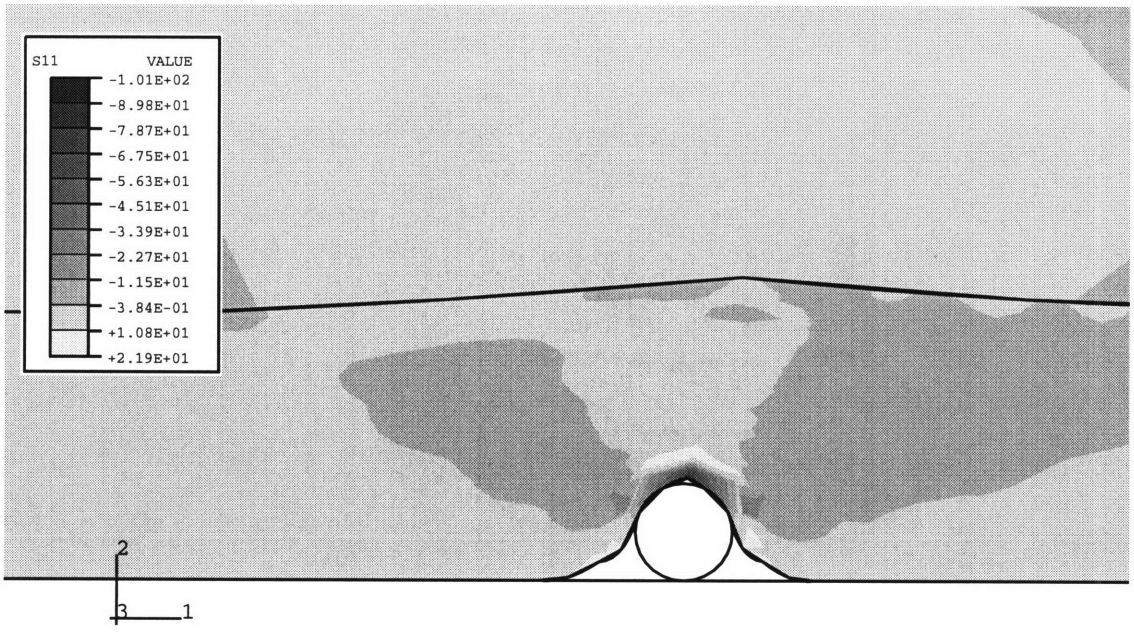

Figure 3.13: 1-direction stress contour after shearing. (frictionless particle-bushing interaction)

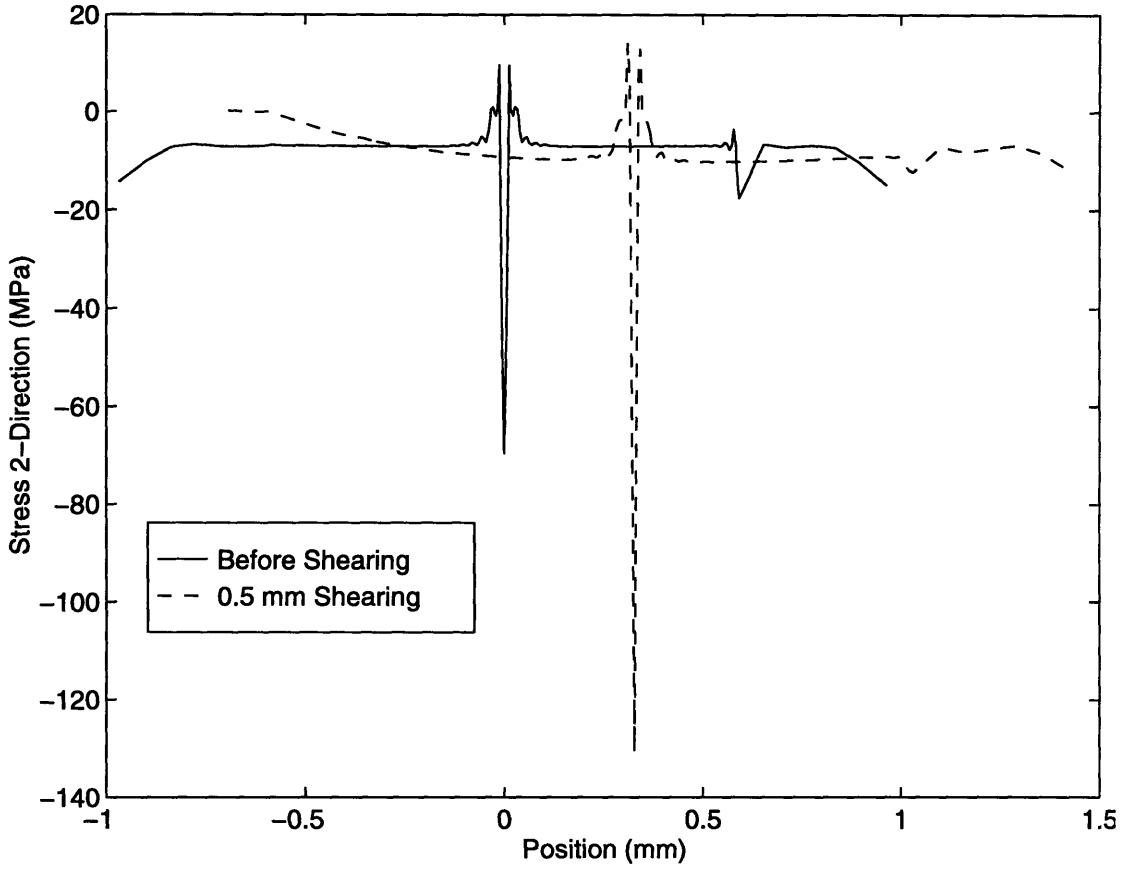

Figure 3.14: 2-direction stress profile along the bottom surface of the finite element model after shearing. (frictionless particle-bushing interaction)

3.2.3 Compression: Fixed Particle-Bushing Interaction

In this simulation, friction was removed from between the particle and material block, and the particle was fixed to the bushing surface. During the compression stage of the loading, the results were very similar to those described above for the friction case. Maximum strains and stresses occurred in similar locations, but the magnitudes of these maximum values were lower. This result is reasonable since friction had been removed from between the particle and material block. For comparison, the maximum stress in the 2-direction along the surface of the material block was -36.5 MPa compared to -70 MPa in the former case. Figures 3.15 and 3.16 show the strain and stress contours in the 2-direction.

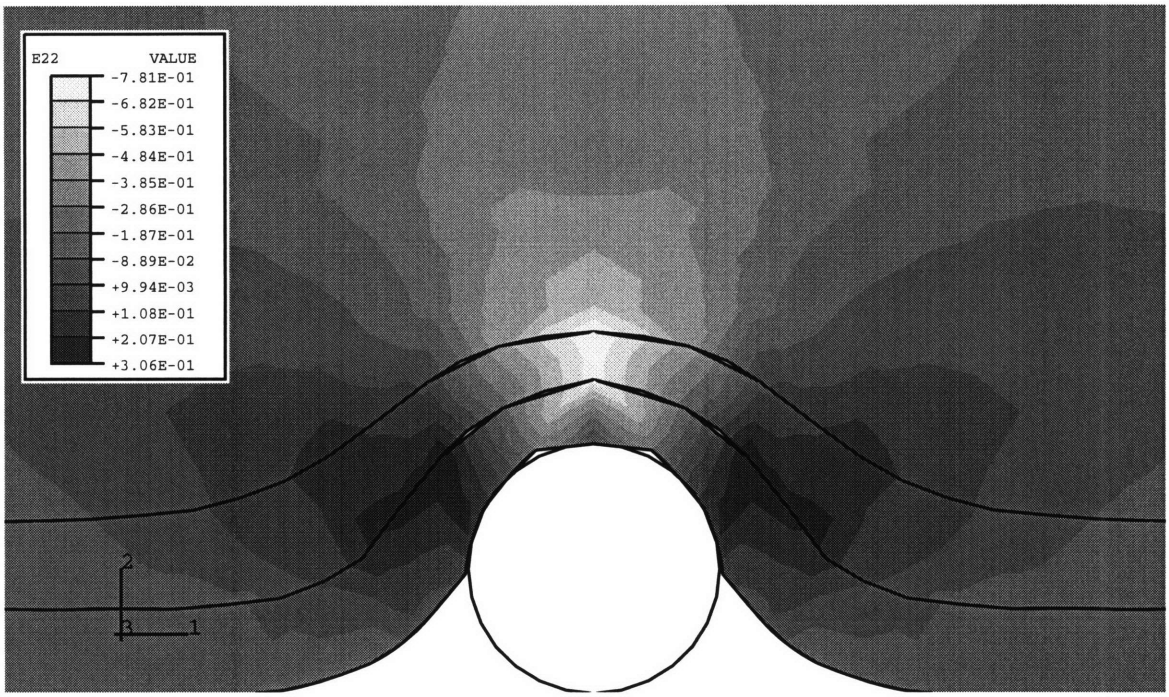

Figure 3.15: 2-direction strain contour after compression loading. (fixed particle-bushing interaction)

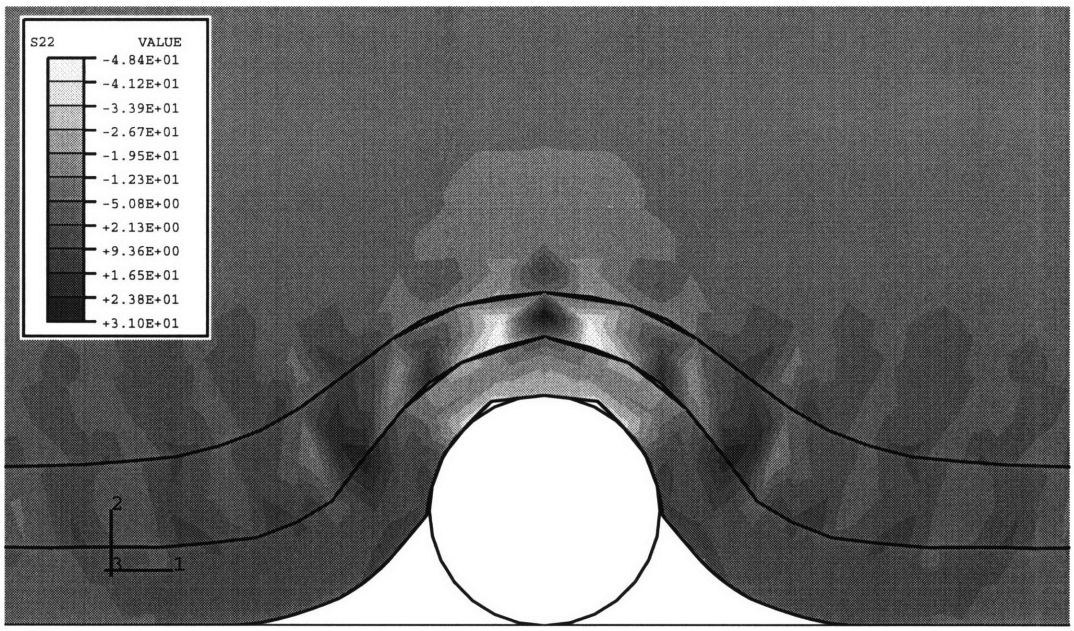

Figure 3.16: 2-direction stress contour after compression loading. (fixed particle-bushing interaction)

3.2.4 Shearing: Fixed Particle-Bushing Interaction

Figure 3.17 shows the deformed shape of the finite element model during different stages of the shear loading. Because of convergence problems, the upper of row of nodes were only displaced 0.12 mm in the positive 1-direction. This progression of pictures shows the severity of deformation of the material block during this type of loading.

The effect of the shear loading for the fixed particle situation again caused an increase in stress and strains and introduced asymmetry in their distributions. For comparison, the maximum stress in the 2-direction was increased to -71.6 MPa from -35.5 MPa, and the strain in the same direction reached a maximum of -0.84 from -0.78. Maximum shear stress magnitudes were 7.91 MPa before shearing. This value was compressive on the right side of the particle and tensile on the left side. After shearing, the right side reached a shear stress of -26 MPa, and the left side reached a value of 16. MPa. In the 1-direction, strains were increased from approximately -0.3 to -0.77, while stresses increased from -35 MPa to -67 MPa. Additionally, the maximum principal strain value was -1.21, occurring at the right side of the particle, and the maximum principal stress was located above the particle at a value of -78 MPa. Figure 3.18 displays the strain contour in the direction of shearing (1-direction), and figure 3.19 shows the shear stress contour. The apparent mesh separation in these figures (also seen in figures 3.15 and 3.16, though less obvious) is purely a plotting effect which occurred in regions where nodal constraints (multiple point constraints, or MPC's) were used in order to refine the mesh. Figure 3.17 verifies that there was no actual mesh separation.

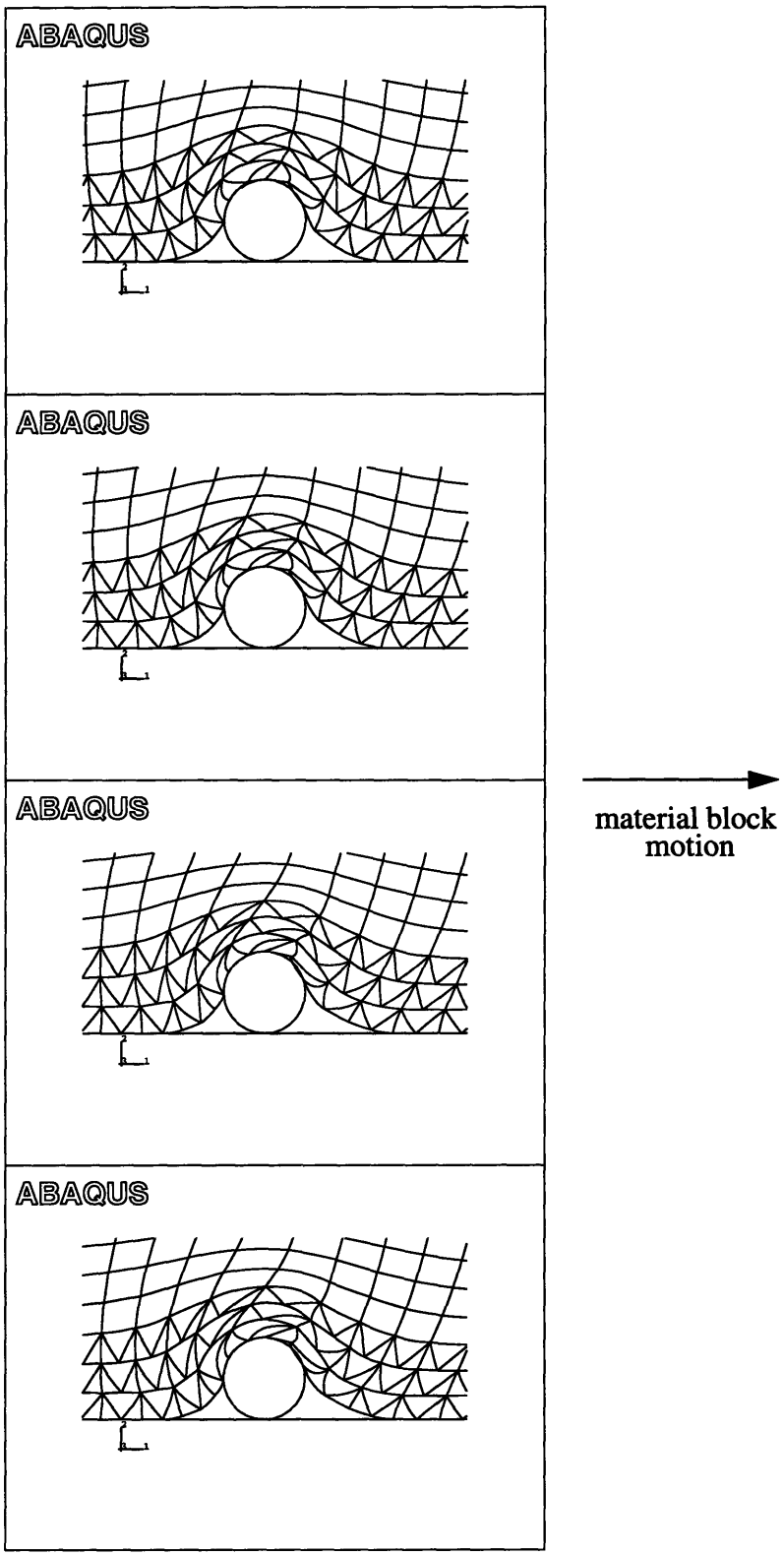

Figure 3.17: Deformed finite element mesh during incremental stages of shearing. (fixed particle-bushing interaction)

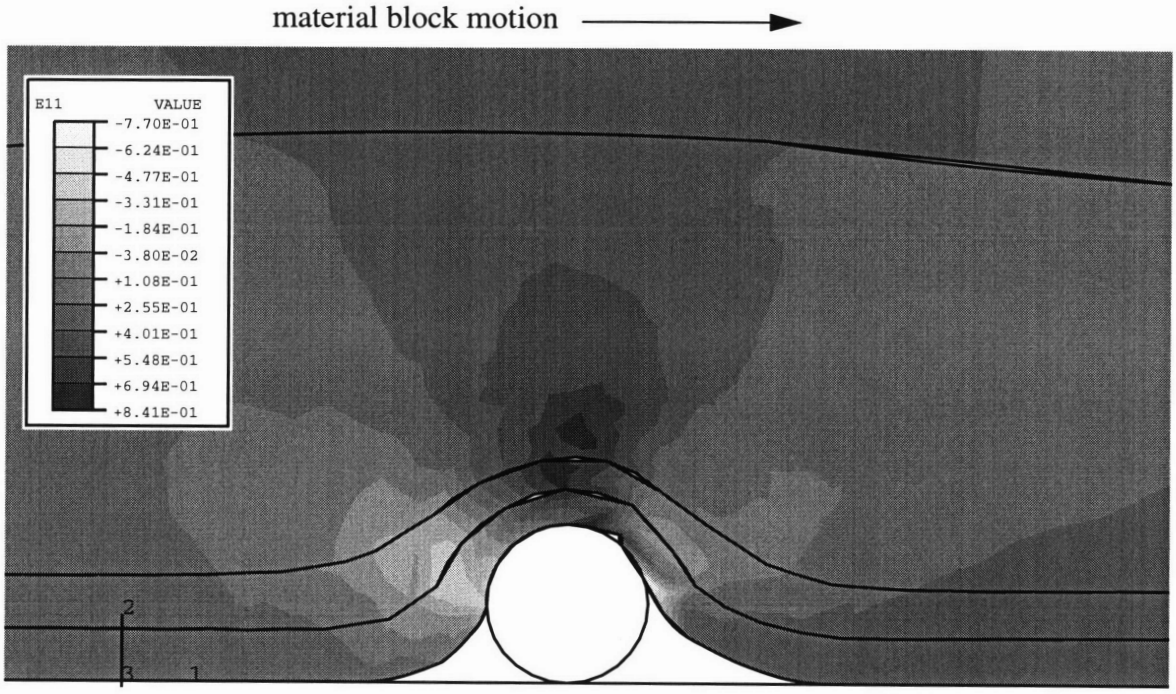

Figure 3.18: 1-direction strain contour after shear loading. (fixed particle-bushing interaction)

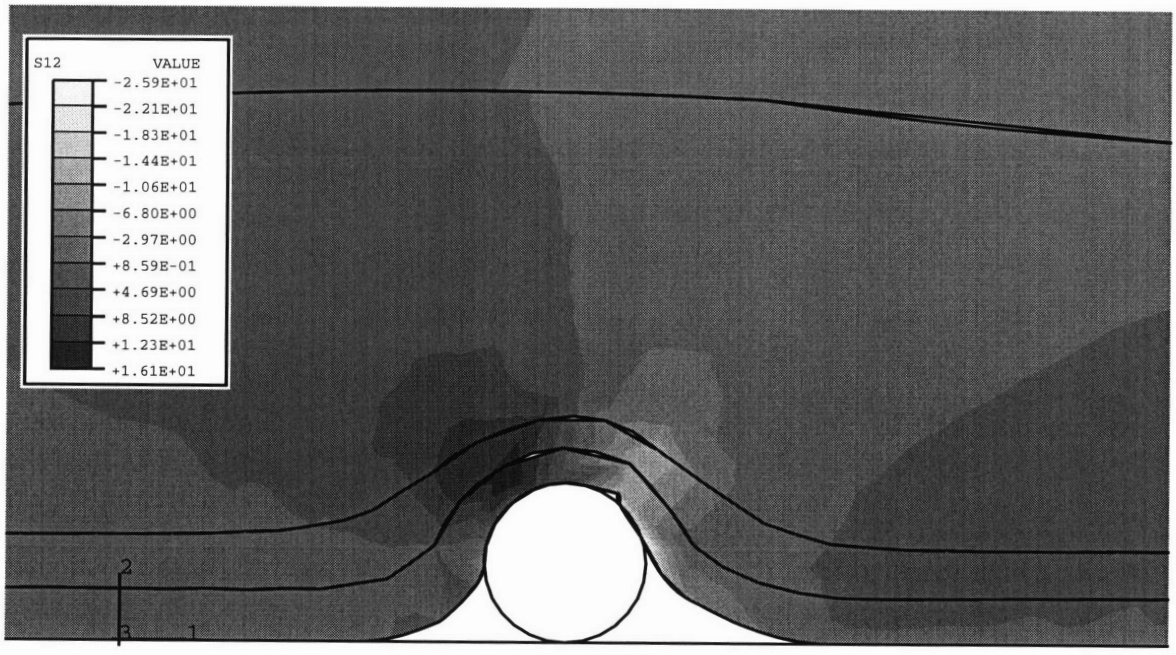

Figure 3.19: 1-direction stress contour after shear loading. (fixed particle-bushing interaction)

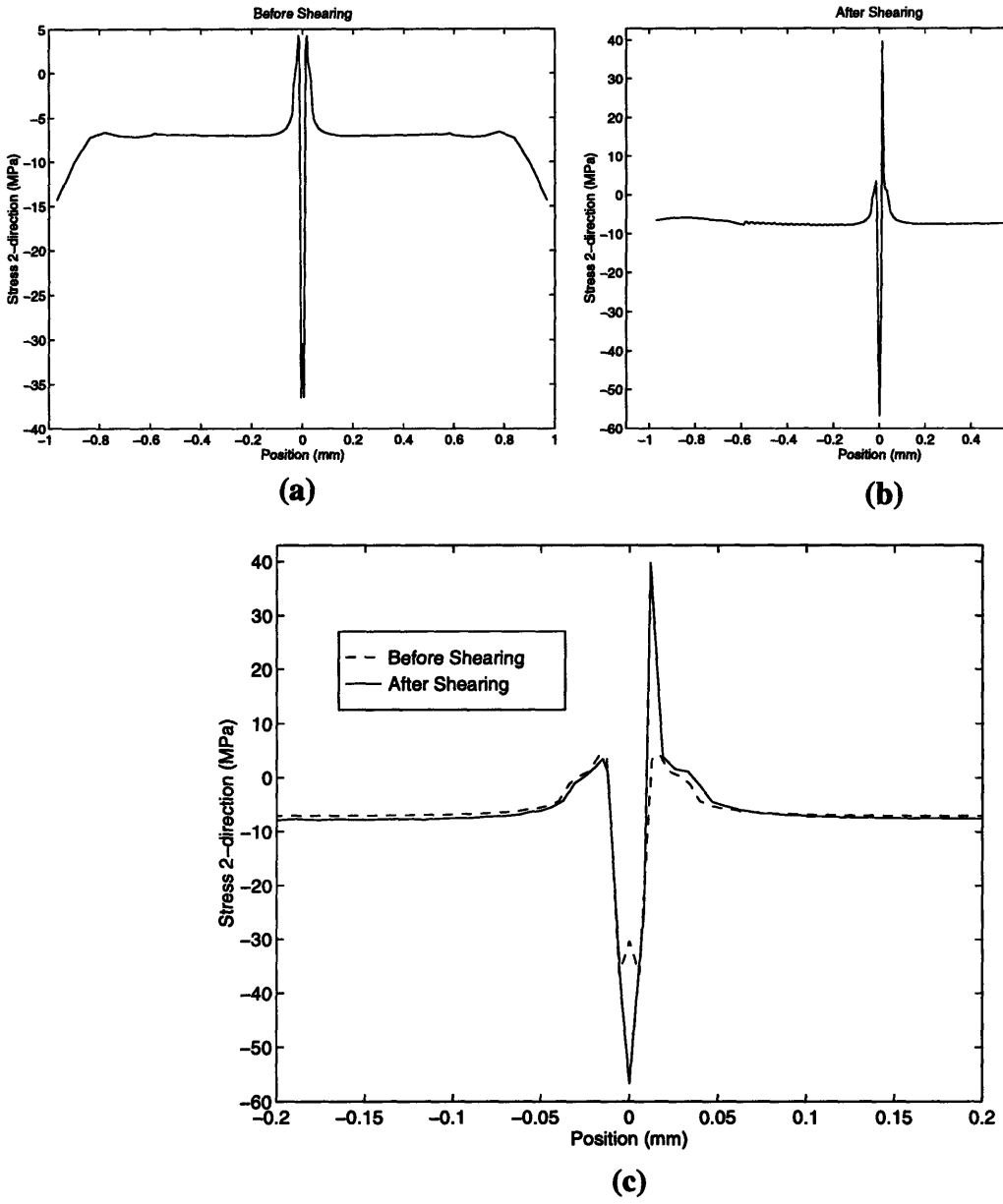

Figure 3.20: 2-direction stress profile along the material block surface for fixed particle-bushing interactions. (a) before shearing (b) after shearing (c) detailed view near particle

Besides significantly increasing the stress and strain maximums, the shape of the stress distribution at the surface of the material block is of particular interest. In the frictionless case, the stress distribution at the surface of the material block basically had the same shape during shearing even though the stress magnitudes changed (figure 3.14). Figure

3.20 shows the 2-direction stress distribution at the surface of the material block before and after shearing for the fixed particle case. The shape of this curve is drastically different. On either side of the center of the particle, a maximum stress was reached, and these maximum values were of opposite signs. The material block was displaced in the positive 1-direction, so the left side of the particle was forced into a state of compression. The other side was placed into tension since the material block cannot freely displace over the particle, as shown by the tiny opening that has developed above and to the right of the particle.

The maximum stress magnitudes at the surface were significantly increased during the shearing as well. For the 0.12 mm displacement, the maximum stress in the 2-direction along the surface of the material block was approximately -55 MPa in compression and 40 MPa in tension. Curves like figure 3.20 can be plotted for the stresses and strains in each direction. In this way, the stresses and strains encountered by each point along the material block surface can be characterized.

As a measure of *cyclic* strain or stress history for a material point, the stress and strains for a particular point in the material can be recorded as a function of the displacement. In figure 3.21, the stress in the 2-direction for an element that is initially directly above the particle is plotted versus the displacement of the upper row of nodes. The upper curve represents the initial motion in the positive 1-direction. The lower curve represents the oscillatory motion, that is the motion in the negative 1-direction after the initial displacement was completed. While the upper row of nodes returned past their original position, the material near the particle clearly did not, as shown by the difference in stresses between the lower and upper curves at displacement equal to zero. Figure 3.22 shows the position of this particular element at displacement equal to zero for the two cases.

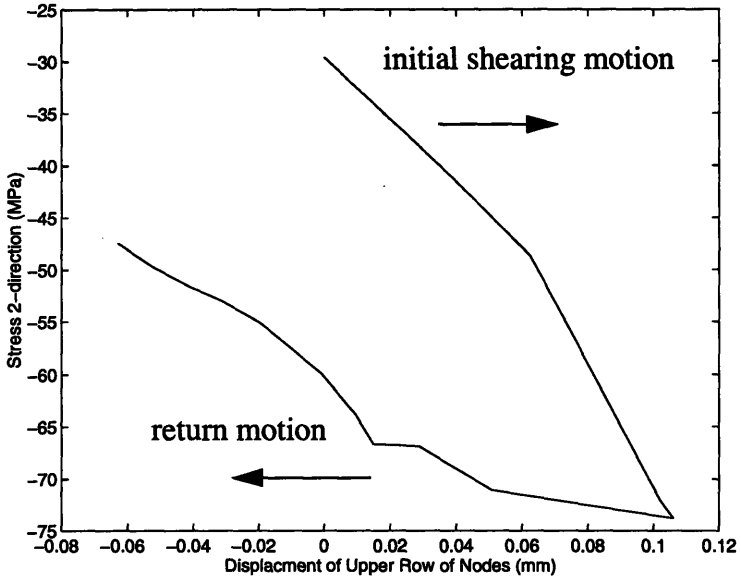

Figure 3.21: 2-direction stress history for a material point which is initially directly above the particle.

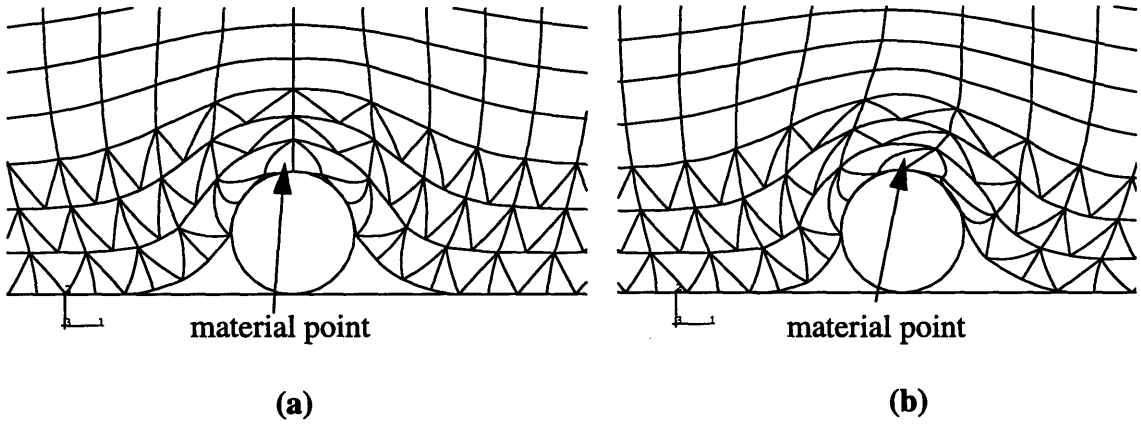

Figure 3.22: Position of the material point corresponding to zero displacement. (a) before the initial shearing motion (b) during the return motion

3.3 Dirt Abrasion Simulation: Discussion of Results

3.3.1 Frictionless Particle-Bushing Interaction

The results of this simulation showed a particle that was trapped within the material block and then dragged along during shearing. Therefore, the frictionless particle bushing

interaction seems to model the case in which a particle becomes trapped in the seal contact band. This situation has ramifications for both the seal and the bushing.

Figure 3.5 showed that the seal material was not able to completely envelop the particle. Thus, openings were created at the sides of the particle which would permit oil loss and provide avenues for further particle entrainment. These openings also illustrate that these regions of the material block are being stretched. These regions of tension and how they fluctuate during loading are of importance because they could be the mechanisms for the wear and abrasion of the seal through cyclic stretching and tearing. Figure 3.14 showed that in the 2-direction, the stress at the sides of the particle increased from approximately 9.5 MPa to 14 MPa during the shearing loading. Additionally, the maximum principal stresses at the sides of the particle were increased from 5.7 MPa to 7.7 MPa, and strains were significantly increased as well. This local amplification of stresses and strains near the particle clearly would accelerate material failure.

It is also interesting to note that the shape of the stress in the 2-direction along the surface of the material block did not change significantly during shearing. This is explained by the fact that the deformation of the material block near the particle did not really change very much. Only the magnitudes of the stresses and strains changed, and the increase was quite significant. For example, the peak stress in the 2-direction was nearly doubled.

From the viewpoint of the bushing, the particle that has become trapped in the seal acts like a cutting edge as the seal is oscillated back and forth. Evidence of damage to the bushing has been observed as grooves on the bushing surface by Caterpillar, Inc. A natural extension of this model then would be to model the bushing as deformable and then to examine the stress concentrations that develop on the bushing surface. The round particle

did not show much of a stress concentration; however, a more jagged particle could be revealing.

3.3.2 Fixed Particle Interaction

The friction and boundary conditions of this simulation modeled a situation in which a particle becomes embedded on the surface of a bushing. In this case, the particle acts more like a cutting edge for the seal. As evidenced by figure 3.20, the fixed particle greatly altered the stress profile of the material surface during shearing. The shearing motion in combination with the fixed particle caused extreme stress concentrations directly to each side of the particle. Again, this local amplification of both stresses and strains leads to material failure.

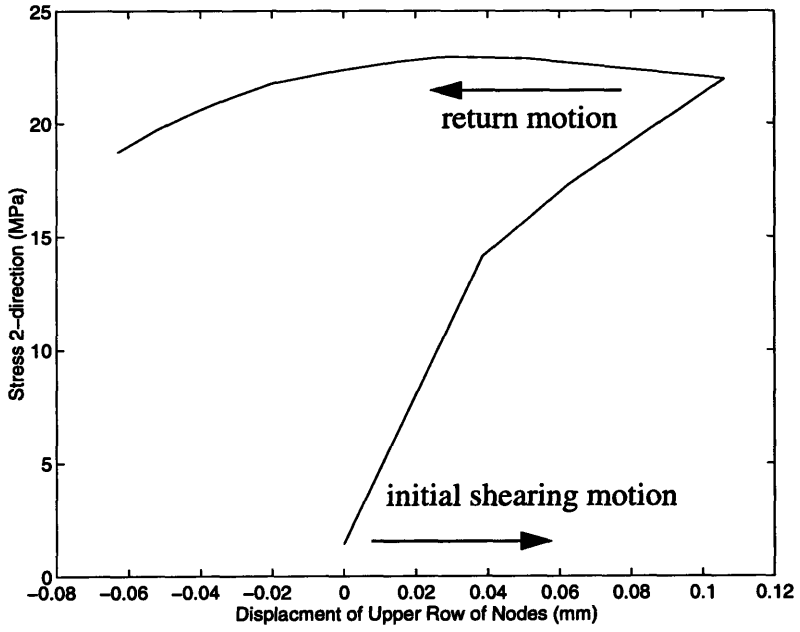

Figure 3.23: 2-direction stress history for a material which is initially located on the right side of the particle.

It is also quite important to note that the stresses to either side of the particle changed signs during the shearing motion (figure 3.20). Thus, a strain or stress history like that in figure 3.21 can be assembled. These *cyclic* stresses provide a fatigue failure mechanism for the seal lip material. Figure 3.23 shows an additional plot for a section of the material

that is initially at the side of the particle. That is, the region is in tension in the 2-direction before shearing. Again, the tensile stresses and fluctuations, as opposed to the compressive ones, are important in considering phenomena like crack propagation and fatigue.

3.3.3 Relationship to Wear and Fatigue Models

An immediate observation from all of the stress and strain contours is that the seal undergoes a very complicated deformation state when in contact with the abrasive particle. Thus, strain-life curves such as the one shown in figure 3.4 can only provide an extremely rough estimate as some sort of averaged strain measure would be needed. In addition, strain or stress-life curves can only capture the fatigue behavior of the material for a specific set of operating conditions. With polymeric materials, there are many factors that can affect fatigue life, and performing tests which would completely characterize the material's fatigue behavior would be extremely cumbersome. Thus, unless the proper operating parameters (for example, the cyclic loading rate, type of loading, and temperature) were used, the life predictions would be even more inappropriate.

Similarly, there is a major obstacle in using the cut growth rate life predictions as discussed earlier because of the complex loading state of the seal lip. The tear energy can only be calculated by first determining the strain energy density. This requires determining the stress-strain curve for the material and then integrating from an initial strain to a final strain. When performing this calculation, the type of loading condition has already been predetermined by the experimental curve being used. For example, the data shown in figure 3.5 was obtained from *tensile* experiments. Thus, the fatigue life predictions resulting from this calculation would only be valid for tensile (mode I) loading. In the case of the seal, however, the loading condition is quite complex as shown by the presence of stresses in the 1, 2, and 1-2 directions. However, the simulations can compute the strain energy density near the particle.

3.3.4 Improving Seal Wear Life

Overall, while possible to characterize the stress and strain cycles that the seal might encounter during oscillatory interactions with a particle, it is difficult to make an estimate of the fatigue or wear life based on this information. However, it is generally understood that reducing the levels of stress and strain would reduce the wear and fatigue of the seal.

This was certainly confirmed experimentally by Ayala's S.M. thesis results which showed that wear only occurred in the presence of abrasive particles. In the absence of a particle, the finite element simulations show a uniform contact stress distribution of only -7 MPa, whereas figures 3.14 and 3.20 show the incredible increase in stress due to the presence of a particle. It is quite clear then that the increased stresses and strains, as shown in the finite element models, are the cause for the accelerated failure of the seal lip material.

Thus, if the stress and strain distributions of the seal lip can be limited despite the presence of abrasive particles, the wear life of the seal can be improved. As discussed, the large strains and stress are generated from stretching of the material over the particle, especially during shearing motions. It was hypothesized then that the addition of depressions or grooves on the seal lip surface could be used to limit the strains experienced by the seal lip and to effectively "trap" the particles. These depressions would help limit stretching of the lip material since the abrasive particles could simply fit inside the depressions. This would also eliminate the gaps around the particles which enable easy entrance of more dirt particles.

The aggressive wear period could then be controlled since the particles are trapped in the depressions, thereby avoiding any locally increased stresses and strains as well as eliminating progression of the particles across the seal contact band. This idea is similar to that of Tian's [27] in which surface features were used to contain wear debris.

Chapter 4

Seal Texturing

Based on the idea of adding surface features such as depressions or grooves to the surface of the seal lip, investigations were performed both experimentally and through finite element modeling to test the feasibility of improving the wear life of the seal through texturing. It was hypothesized that the addition of such textures would extend the wear life of the seal by trapping the particles, thereby eliminating the locally elevated strains and stresses induced in the seal material due to compression and shearing over the particle; eliminating these stresses would eliminate abrasion of the seal material and thus control the progression of the aggressive wear period.

This chapter first describes how initial experimental results demonstrated that circular depressions surrounded by a raised rim, or "bump," significantly prolonged the wear life of the seal. Next, finite element simulations of three types of textures were considered in order to understand their effect on the seal system. Examining the contact stress profile at the seal lip proved to be extremely useful as it indirectly provided additional information about the lubrication profile underneath the seal lip and around each texture. Finally, current experimental results involving time-lapse video and LIF measurements [14] are used to validate the success of the textured seal design and to provide a basis for understanding the wear reduction mechanism, especially in relation to the finite element results.

4.1 Introduction

4.1.1 Initial Experimental Results

Based on the idea of adding depressions to the seal surface to reduce local straining and to control the aggressive wear period through particle trapping, an experiment involving different types of "textures" was performed. The experiments reported here were con-

ducted by Hugo Ayala as part of his doctoral research [15]. A test track seal was divided into four regions. The first region contained grooves that ran tangentially along the circumference of the seal, while the second region contained grooves that ran radially. The third region contained circular depressions, and the fourth region was left untextured. This seal was worn in the presence of abrasive particles and then examined. All of the textures were found to extend the life of the seal in comparison to the unmodified seal. By comparing the wear in each of the four regions, the test results showed that circular depressions outperformed the other types of textures in terms of extending the seal wear life.

Upon closer examination, it was discovered that the circular depressions were actually surrounded by a raised rim of material. The raised rim was the result of seal material that was displaced when the textures were made. (Depressions were created by inserting a heated pin into the surface of the seal.)

4.1.2 Texture Finite Element Modeling

Based on these experimental results, three types of textures were considered: depressions, raised bumps, and a combination of depressions and bumps. These features are intended to be placed periodically along the circumference of the seal's lip surface. The finite element models were made from two dimensional axisymmetric elements. As shown in figure 4.1, the axisymmetric model represented a cylinder of material from the seal surface. The radial direction thus represents distance from the seal lip edge as well as distance between textures.

The overall dimensions of the model cylinder without the texture measured 2.26 mm high in the 2 dimensional representation. The height corresponded to the depth of seal material in the lip of the seal assembly. Besides the geometry of the textures, the width of the model was left open so that the effect of seal lip edge position and texture spacing could be studied.

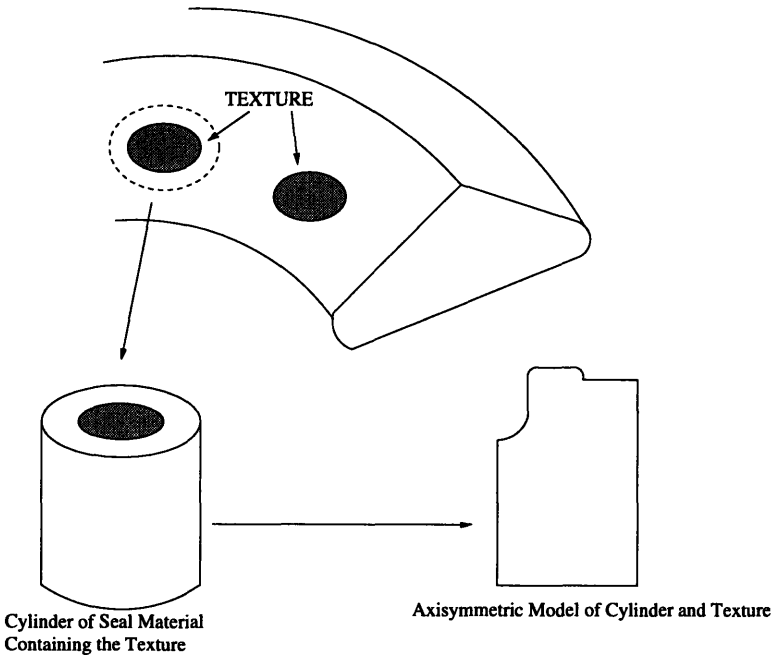

Figure 4.1: Schematic of axisymmetric model in relation to the actual seal.

The model was assembled from two dimensional, axisymmetric, quadratic, hybrid elements (CAX8H). In some cases, three sided elements (CAX6H) were used for mesh refinement. Again, the material model used was the Mooney-Rivlin hyperelastic model with the same material parameters as before. It is emphasized that the Mooney-Rivlin model was used here to efficiently observe the general trends which result from parametric changes to the texture geometry. The Mooney-Rivlin model does not properly capture the behavior of the seal materials, and the reader is referred to chapters 6 through 8 for a discussion of more accurate constitutive models.

The bushing surface was modeled with a rigid surface definition in contact with the bottom surface of the cylinder of material. Loading was accomplished by displacing the upper row of nodes in the negative 2-direction. In essence, this displacement represented the displacement of the stiffener ring in the full seal assembly model. The chosen displacement value was 0.87 mm. This displacement value corresponded to an average contact

stress of -8 MPa in the absence of any textures. It was assumed that the addition of features on the order of 0.15 mm in height would not affect this value. Considering that the entire seal assembly has a height of 14.7 mm before compression, this assumption is quite valid.

The average contact stress as shown in the full seal assembly finite element model was actually -7 MPa. However, the model overestimated the seal contact band. If the total force on the seal is redistributed over a seal contact band more like the measured 1.55 to 1.6 mm, the average contact stress is closer to -8 MPa.

Finally, because the cylinder represents a repeated unit cell, the sides of the model were contstrained to deform uniformly.

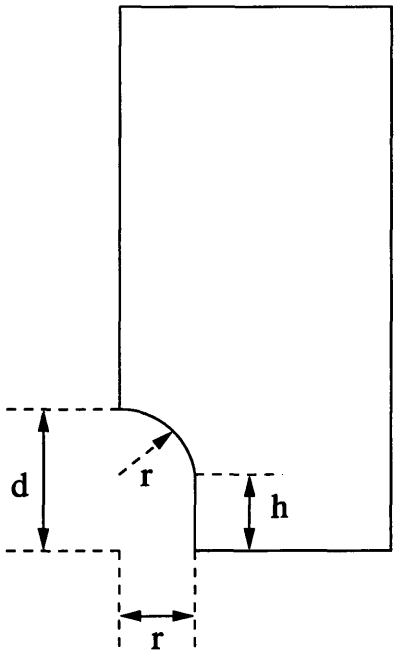

Figure 4.2: Geometry of depression textures.

4.2 Depression Only Simulations

4.2.1 Model Description

Figure 4.2 shows the geometry of the depressions that were under consideration in these finite element simulations. As shown, the depression was cylindrical in shape and terminated in the shape of a dome of identical radius as the cylinder. The depth of the

depression, d, was thus the sum of the radius, r, and the height of the cylinder, h. The width of the model, w, represents both the distance from the seal lip edge and the texture spacing in this axisymmetric representation.

4.2.2 Depth Study

In these simulations, the radius, r, was fixed at 0.15 mm. The depth of the depression was then varied by altering the value of h. Depth values were tested between 0.3 mm and 0.6 mm. The width of the model was fixed at 0.7 mm.

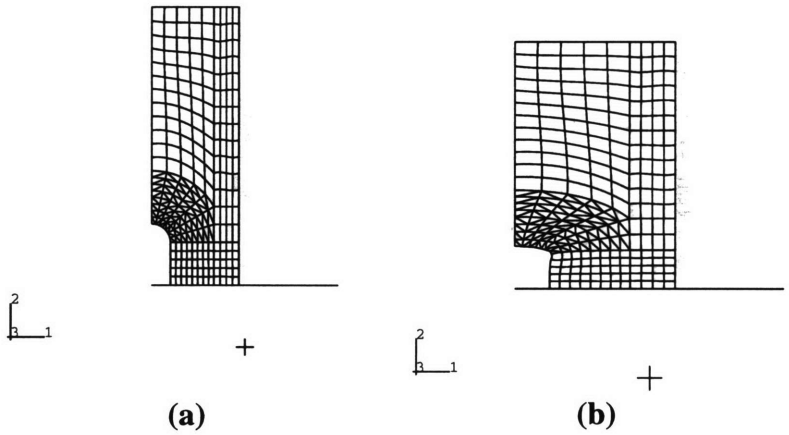

Figure 4.3: Finite element mesh of depression texture. (a) before deformation (b) after deformation

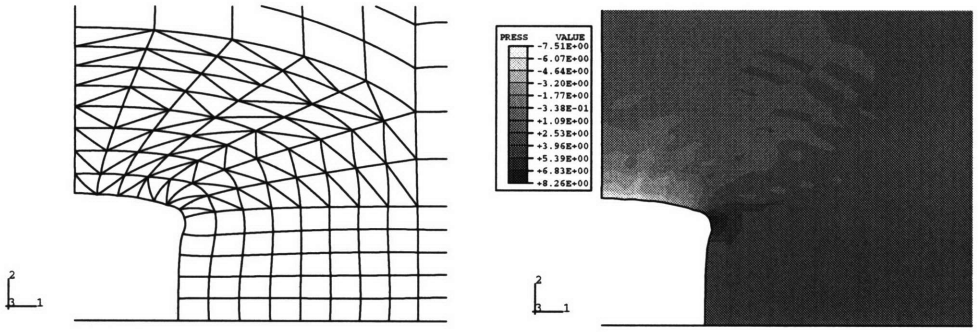

Figure 4.4: Detailed view and pressure contour of deformed depression texture.

Figure 4.3 shows an example of the finite element model before and after deformation with d equal to 0.5 mm. A detailed picture of the deformed depression is shown in figure 4.4 along with a contour of the pressure distribution. By examining these two figures, it was clear that the region of the depression that transitions from cylinder to dome was

being placed under large stresses. The pressure contour certainly indicates the concentration of stress at that juncture, and the deformed mesh seems to suggest that the depression was folding on itself at that location. Negative eigenvalue warnings during the finite element simulation would indicate that local buckling of the material was occurring at that location.

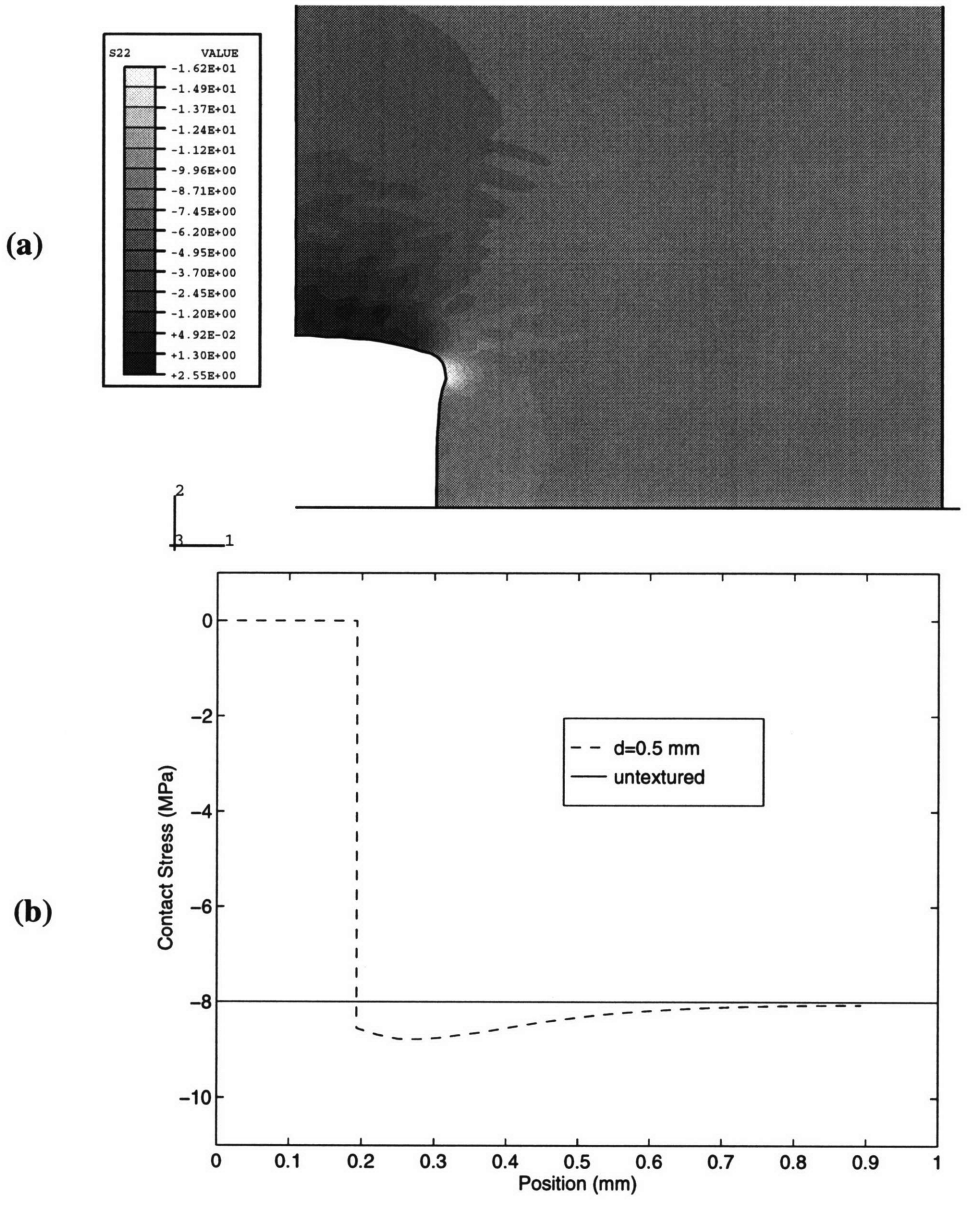

Figure 4.5: (a) 2-direction stress contour of depression texture. (b) Contact stress profile along the surface of the finite element model.

Of particular interest is the contact pressure distribution along the surface of the model. By looking at the stresses in the 2-direction interpolated to the nodes at the surface of the model, an accurate measure of the contact stress was obtained. Figure 4.5 shows the 2-direction stress contour as well as the contact pressure profile at the surface. It should be recalled that in the absence of the texture, the contact pressure profile is constant at -8 MPa. As shown, the presence of the depression resulted in a peak contact pressure of approximately -8.8 MPa, a 10% increase. The region where the contact stress was zero represents the actual depression.

Figure 4.6 shows the results of varying the depth, d. As shown, the trend indicates that as the depth was decreased, the peak contact pressure attained was actually increased. For a d equal to 0.3 mm, the maximum contact stress was increased to approximately -10.25 MPa. This is somewhat non-intuitive, given that if d equals zero, the contact stress increase between the textured and untextured models should also be zero.

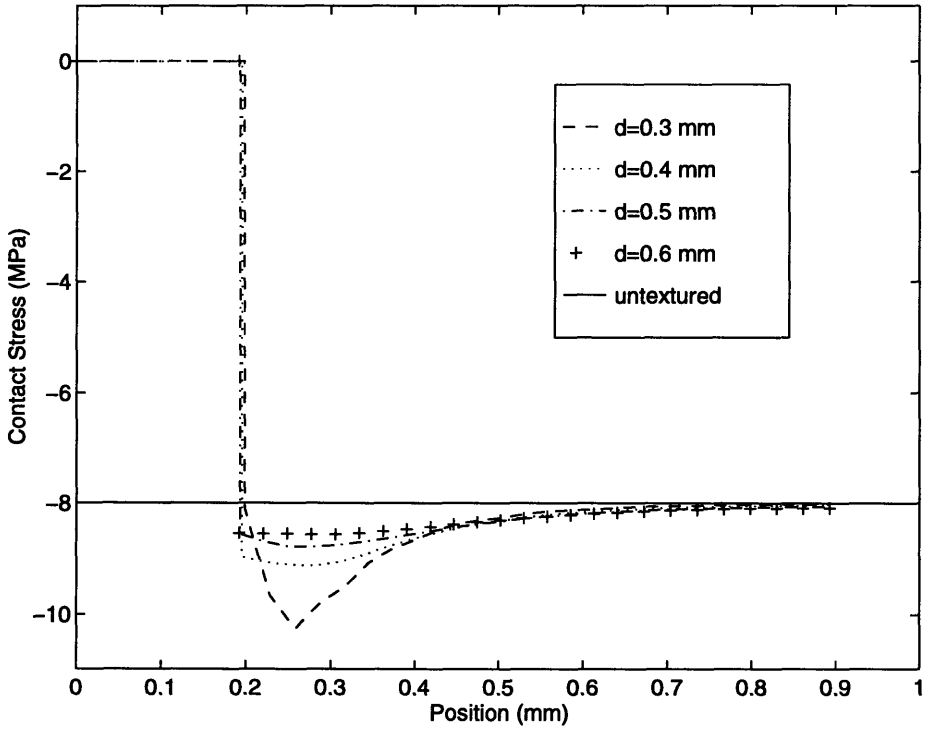

Figure 4.6: Contact stress profile for depression textures with varying depths, d.

The reasoning behind this stress increase was revealed by examining the 2-direction stress contours for two different meshes. Figure 4.7 compares the 2-direction stress contour for d equal to 0.3 mm and 0.6 mm. As shown, the local buckling at the corner of the depression caused localized regions of stress concentration. For the smaller values of d, the seal surface lay within the region of stress concentration. Thus, the contact stress is influenced by the buckling. For the larger values of d, the seal surface was unaffected by the localized region of stress concentration. It is also interesting to note that the region of stress concentration was shaped somewhat like a shear band in that its effects emanate at an angle. Thus, the location of the peak contact pressure was influenced as well. As shown in figure 4.6, the peak contact pressure was located away from the edge of the depression for d equal to 0.3.

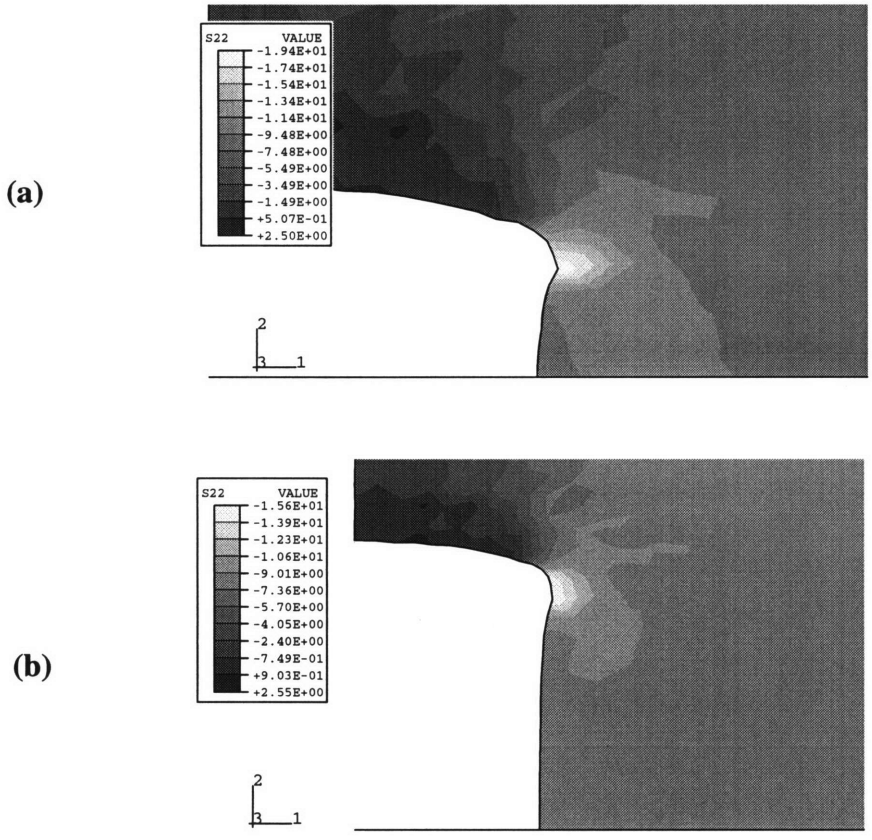

Figure 4.7: Comparison between the 2-direction stress contours of a depression texture having depth equal to (a) 0.3 mm and (b) 0.6 mm.

These results suggest other depression designs. The previous depression design benefited from the strong stress concentration caused by the geometric discontinuity between the dome and cylinder sections. A natural idea would be to completely eliminate the cylinder section, thereby moving the region of local buckling directly to the seal surface. Thus, if a higher peak contact pressure was sought, this design would probably perform better. Similarly, a cone shaped depression was considered.

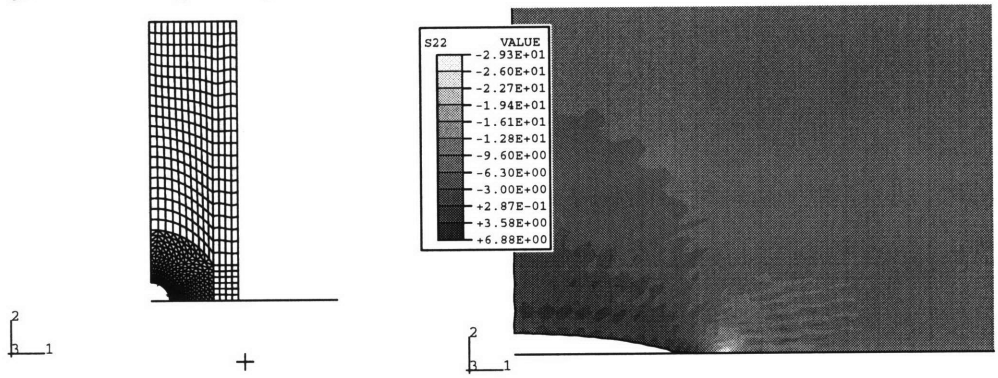

Figure 4.8: Finite element mesh and 2-direction stress contour of a dome shaped depression.

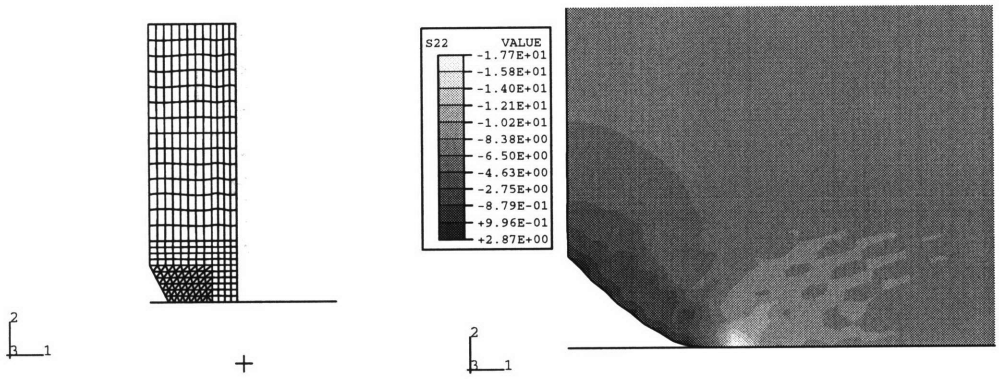

Figure 4.9: Finite element mesh and 2-direction stress contour of a cone shaped depression.

Figure 4.8 shows the mesh of the dome shaped depression and the resulting 2-direction stress contour, while figure 4.9 shows the mesh and 2-direction stress contour of the cone shaped depression. The contact stress profiles are plotted in figure 4.10. As shown, the contact stresses were increased to approximately -35 MPa and -19 MPa for the dome and cone respectively.

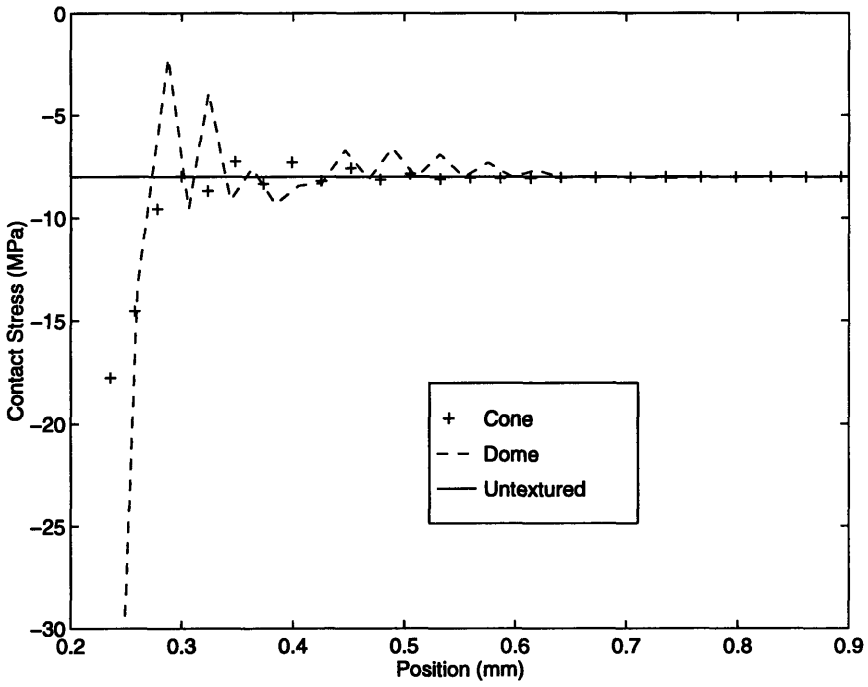

Figure 4.10: Contact stress profiles of the cone and dome shaped textures.

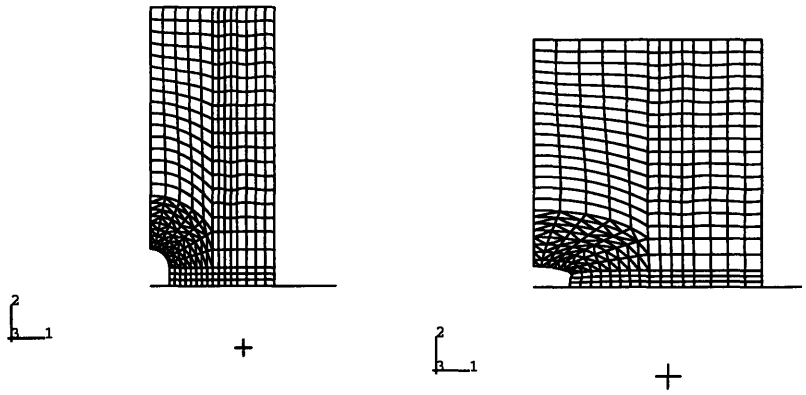

Figure 4.11: Finite element mesh of the depression texture with width equal to 1.0 mm. (a) before deformation. (b) after deformation.

4.2.3 Width Study

In these simulations, the radius of the depression was again fixed at 0.15 mm, and the depth, d, was fixed at 0.3 mm. The width was varied from 0.7 mm to 1.15 mm.

Figure 4.11 shows the finite element mesh before and after deformation for a model with width equal to 1.0 mm. The deformed mesh shows nothing unusual from the previous deformed meshes. In fact, a graph of the contact stresses for the varying widths shows that

the width does not affect the shape nor magnitude of the peak contact stress (figure 4.12). Basically, the effect of the depression was completely contained within 0.62 mm. After this point, the contact stress was simply equal to that for the non-textured model.

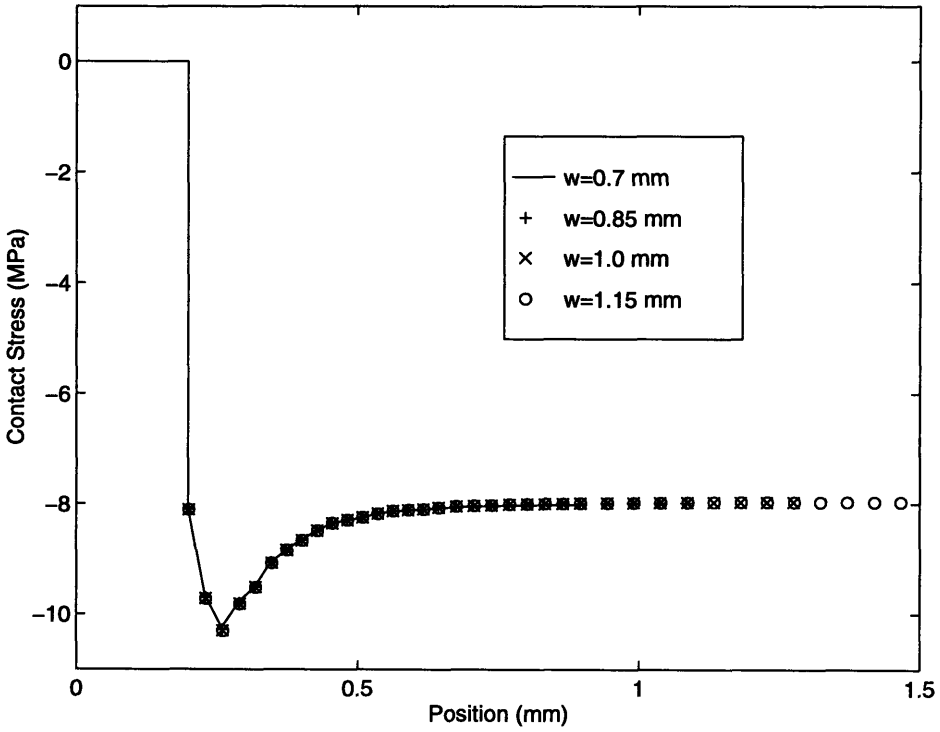

Figure 4.12: Contact stress profile for depression textures for varying widths, w.

4.2.4 Radius Study

The purpose of these simulations was to investigate the effect of changing the radius of the depression. This proved to be a bit involved as changing the radius, r, also affected the depth of the depression. The depth could be maintained at a constant value by adjusting the height of the cylindrical section of the depression. However, as shown in the previous section, h can greatly influence the contact stress by bringing the effect of buckling closer to the seal surface. In this way, it would be difficult to separate the influence of the buckling from the effects of varying the radius. It was thus decided to maintain the height of the cylindrical section and allow the depth to vary directly with the radius. This scheme was obviously not perfect since d was different for each simulation. The chosen height was 0.35 mm, and the width was held constant at 0.7 mm.

The results of varying the depression radius from 0.05 mm to 0.2 mm are shown in figure 4.13. As shown, increasing the radius raised the maximum contact stress. The radius of 0.2 mm increased the contact stress by approximately 34%. Because of the larger radius, the location of the maximum contact stress was naturally moved outward from the axis of symmetry.

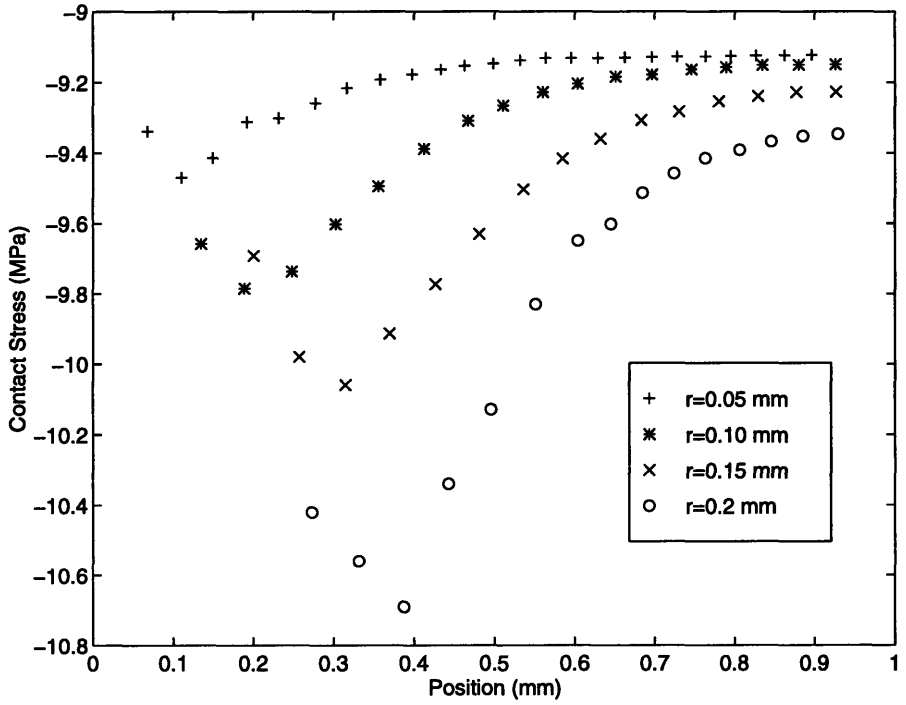

Figure 4.13: Contact stress profile for varying radius, r.

4.2.5 Discussion

The presence of a depression created a large contact stress gradient at the edge of the depression. For a radius of 0.15 mm and a depth of 0.3 mm, the gradient went from zero to -10.25 MPa. For this geometry, the entire influence of the depression was limited to a region approximately 0.6 mm from the axis of symmetry. Beyond this point, the contact stress was constant at -8.1 MPa, slightly higher than the value for the non-textured model. Independent of the width of the finite element model, the effect of the depression was always contained within the 0.6 mm, and the contact stress distribution always converged to -8 MPa outside of that region.

Depending on further experimental results, it may be desirable to have a larger or smaller peak contact stress to change the contact stress gradient. It was shown through the different parametric studies that the peak contact stress could be adjusted by changing the geometry of the depression. Central to altering the peak contact stress was the idea of localized buckling at the base of the dome portion of the depression. By moving the position of the localized region of stress concentration, the peak contact stress could be adjusted. Similarly, different depression shapes, such as the dome or cone shapes, were shown to increase the peak contact stress much higher. Increasing the depression radius had similar effects. The larger dome portion of the depression seemed to cause a larger stress concentration region.

4.3 Bump Only

4.3.1 Model Description

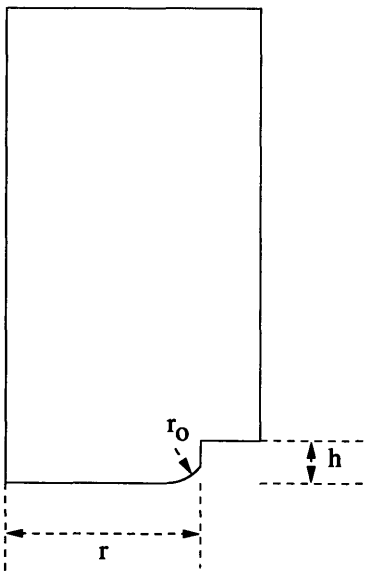

Figure 4.14: Schematic of bump textures.

Figure 4.14 shows a schematic of the type of geometry being considered in these finite element simulations. The bump is basically cylindrical in shape with a rounded edge. The bump is characterized by a radius, r, and a height, h. The radius of the rounded edge is

characterized by r_o. For most of these simulations, r_o was fixed at 0.05 mm. In addition, the overall width of the model was held constant at 0.7 mm.

4.3.2 Height Study

These simulations explored the effect of changing the height, h. The radius of the rounded edge was held constant at 0.05 mm, and the radius of the bump was maintained at 0.5 mm. Heights were varied from 0.1 mm to 0.175 mm.

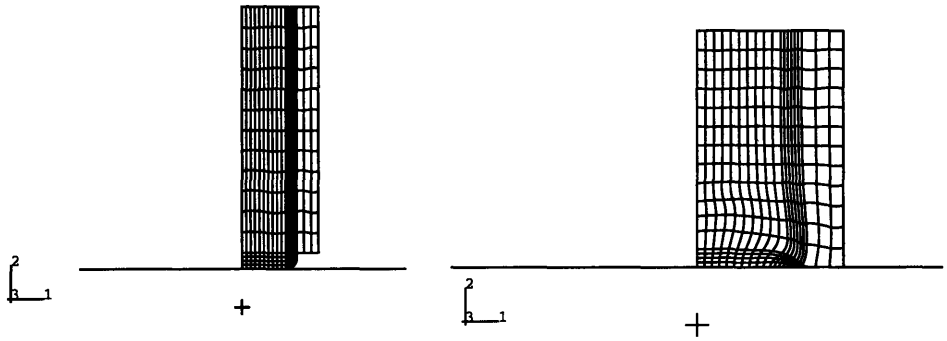

Figure 4.15: Deformed finite element mesh of a bump texture (a) before deformation (b) after deformation.

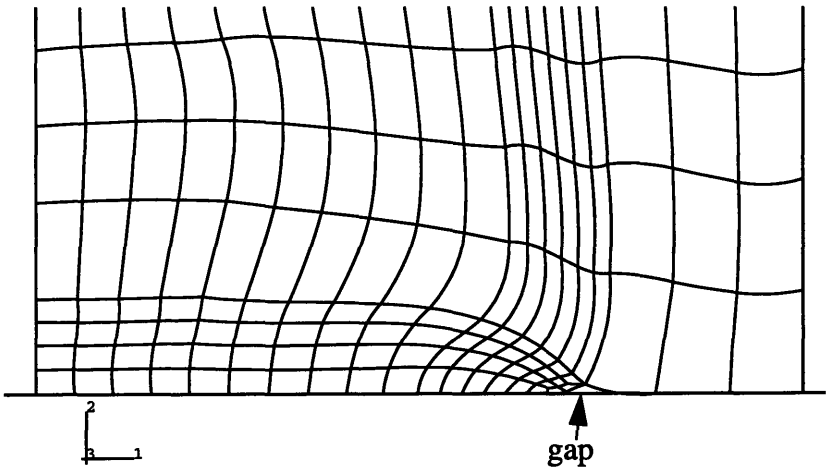

Figure 4.16: Detailed view of the deformed bump texture.

Figure 4.15 shows the finite element mesh before and after deformation for a height equal to 0.15 mm. A more detailed picture of the deformed mesh is shown in figure 4.16. Of particular interest was the small gap that resulted. The seal surface is not able to completely conform to the bushing surface. Figure 4.17 shows the contact stress distribution

for this model. The gap manifested itself as the region of tensile stress in this graph. Beyond the gap, the contact stresses tended to converge to approximately -5 MPa. The location of the peak contact stress occurred at the edge of the bump just before the gap, while the majority of the bump was at a constant contact stress of approximately -9 MPa.

Figure 4.18 displays the results for all of the varying heights. As shown, the peak contact stress increased with larger heights. Both the location of the peak contact stress and the location of the tensile stresses basically occurred in the same position regardless of the height of the bump. The contact stress peaked at approximately 0.5 mm from the axis of symmetry of the model, and the tensile stresses occurred 0.6 mm from the axis of symmetry.

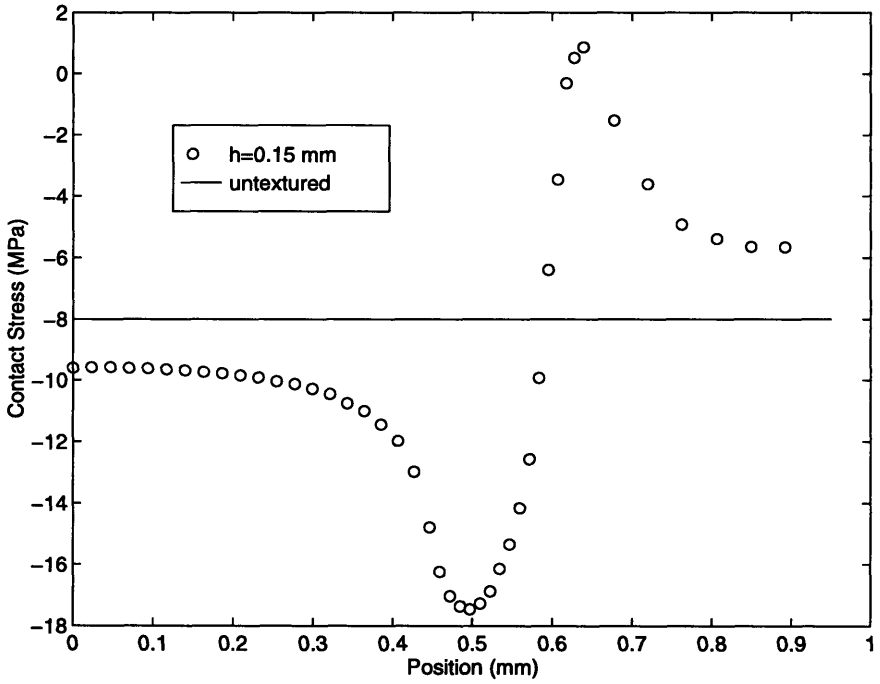

Figure 4.17: Contact stress profile for a bump texture.

4.3.3 Radius Study

For these simulations, the height of the bump was held constant at 0.15 mm. The radius of the rounded edge was again 0.05 mm. The radius of the bump was then varied from 0.4 mm to 0.6 mm.

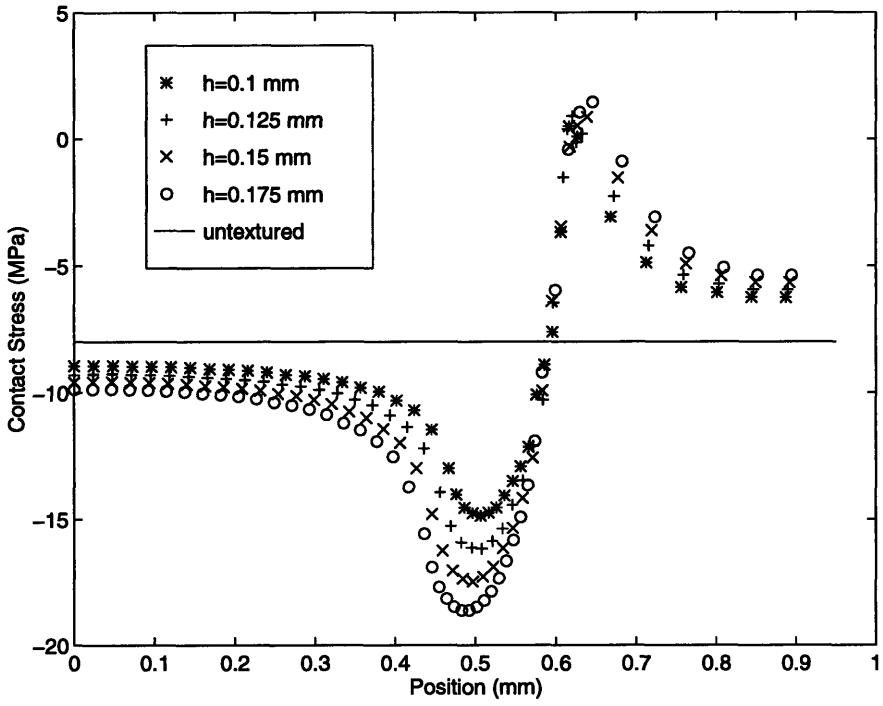

Figure 4.18: Contact stress profiles for a bump texture with varying heights, h.

Figure 4.19 shows the contact stress distribution for the various bump radii. The maximum contact stress varied slightly for the three different radii. The smallest radius of 0.4 mm displayed the largest contact stress at approximately -18 MPa. Similarly, the contact stress at the center of the bump and the contact stress at the other edge of the finite element model both converged to larger values of contact stress. At the center of the bump, the contact stress was approximately -10.5 MPa, while the contact stress at the outer edge of the model was -6 MPa. For comparison, the 0.6 mm radius displayed a contact stress of -8 MPa at the center of the bump and a value of -3 MPa at the outer edge. Naturally, the position of the maximum contact stress and tensile contact stresses shifted for the different radius values.

This trend was quite reasonable. For models with larger radii, the reaction force felt by the bushing would be larger. However, with the additional material, the force was distrib-

uted over a larger area. Thus, it can be expected that the contact stresses would be lower. For models with smaller radii, the contact stresses would be higher because the reaction force, though smaller in magnitude, was distributed over much less material.

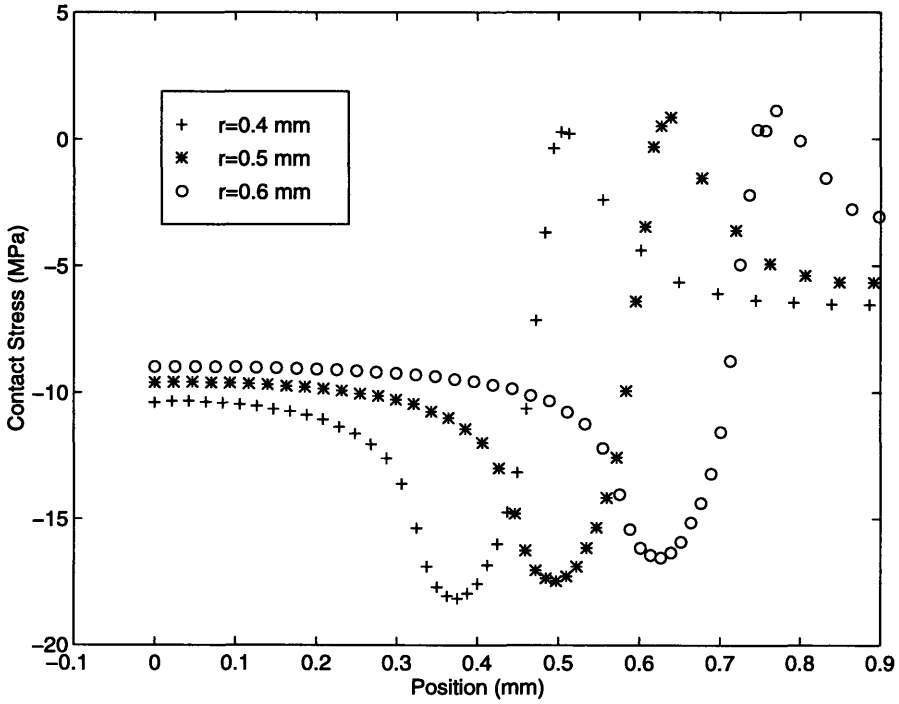

Figure 4.19: Contact stress profile for a bump texture with varying radius, r.

4.3.4 Discussion

The effect of the bump shaped texture somewhat mirrored the effect of the depression texture. Looking again at a deformed mesh of the bump texture, the small gap that resulted can actually be viewed as a depression. Thus, the contact stress in the gap was basically zero. Progressing from the gap towards the center of the bump, the peak contact pressure was reached just outside the gap and then the contact stress distribution basically reached a final value towards the center of the bump. The same basic contact stress distribution was seen in the depression finite element simulations. The contact stress was zero inside the depression. At the edge of the depression, the maximum contact stress was reached, and then the distribution tailed off to a final value.

The major differences in these simulations were the locations and magnitudes of the contact stress peaks and valley as well as the distribution of stress beyond the gap. As mentioned, the bump contact stress distribution was a mirror reflection of the depression contact stress distribution. The effect of the bump increased the contact stress by 125% over the stress resulting from a non-textured model (for h=0.175, r=0.5), and the contact stress at the center of the bump was -10 MPa. The maximum increase shown in the depression texture models was 28% (h=0.3), and the contact stress at the edge of the model converged to -8.1 MPa. Beyond the gap, the contact stress converged to a value below -8 MPa (-5.5 MPa for r=0.5 mm, h=0.15 mm).

4.4 Hole-Bump

4.4.1 Model Description

This simulation explored the effect of combining the two previously described textures. A depression was placed within a bump, as shown in figure 4.20. The height of the bump was 0.1 mm, and the radius of the bump was 0.5 mm. The depression was 0.15 mm in radius and 0.5 mm in depth. The width of the finite element model was 0.7 mm.

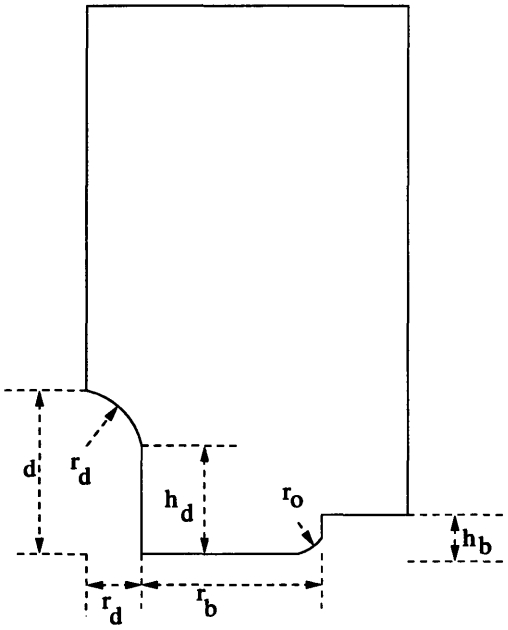

Figure 4.20: Schematic of a hole-bump texture.

4.4.2 Results

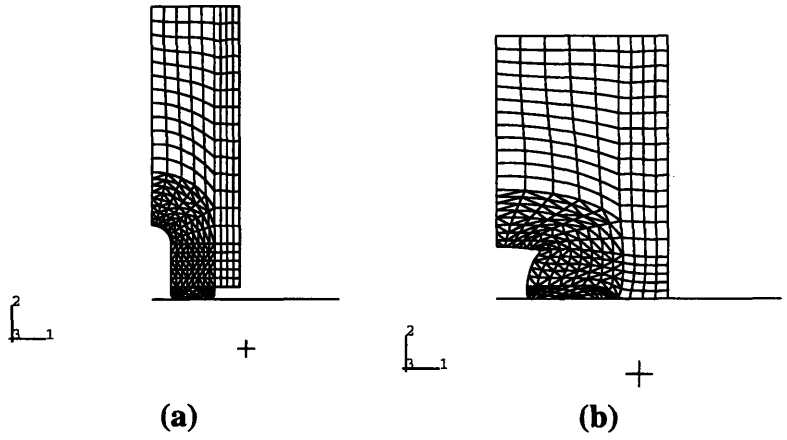

Figure 4.21: Finite element mesh of a hole-bump textures shown (a) before deformation and (b) after deformation.

The texture mesh is shown before and after deformation in figure 4.21. A detailed 2-direction stress contour is shown in figure 4.22. Most of the features shown previously were present. The contact stress profile at the surface, as shown in figure 4.23, was a combination of the previous two contact stress distributions. The influence of the depression was seen in a relative contact stress peak at the edge of the depression. The effect of the bump was evident in a second contact stress peak occurring at the edge of the bump just before the gap. The magnitude of the second peak was larger as predicted by earlier simulations. A region of tensile stress along with the picture of the deformed mesh confirmed the presence of a gap again. After the regions of tensile stress in the gap, the contact stress profile converged to a value of -6 MPa.

The first peak had a value of -13 MPa, a 63% increase over the non-textured contact stress. The second peak reached a value of -20 MPa, which was an increase of 150%. The location of the first peak was at approximately 0.22 mm from the axis of symmetry, while the second peak occurred at 0.55 mm. The gap occurred at approximately 0.63 mm.

Figure 4.22: 2-direction stress contour for the hole-bump texture.

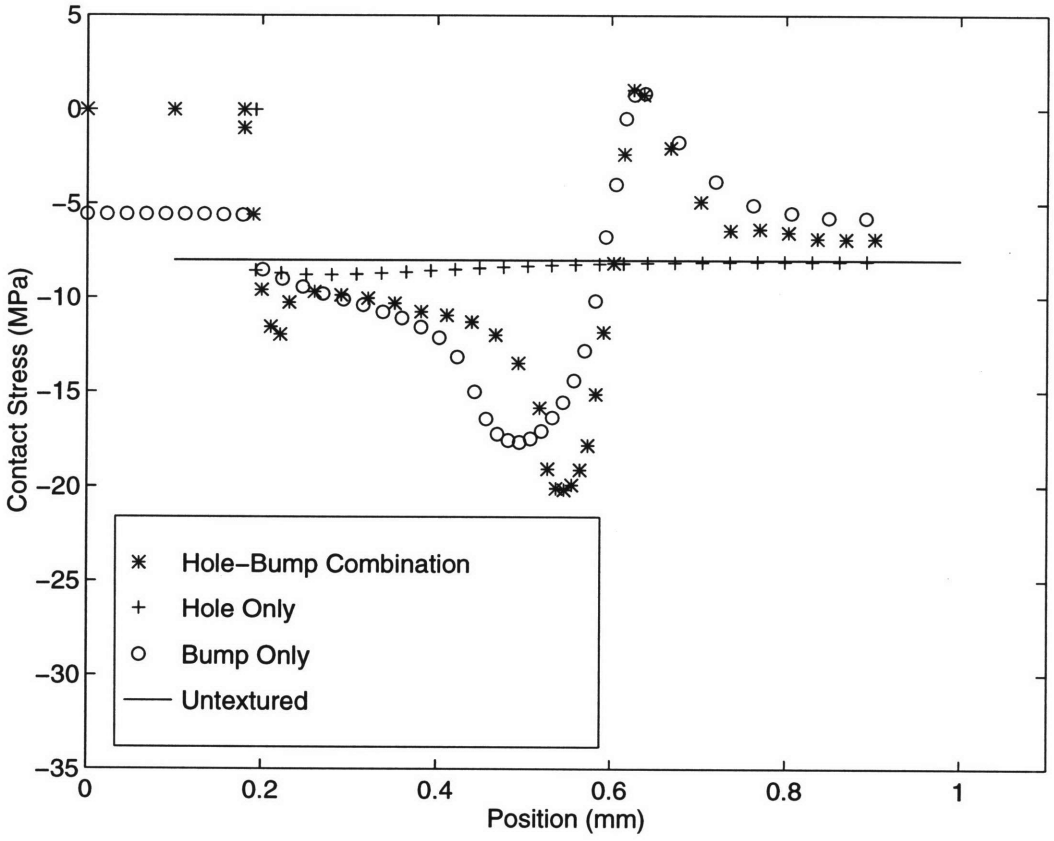

Figure 4.23: Contact stress profile for the hole-bump texture.

4.4.3 Discussion

The hole-bump combination was not a perfect superposition of the two separate effects. Contact stress increases were higher, and the location of key features were further from the axis of symmetry.

However, the shape of the contact stress profile did indeed resemble a combination of the two separate features. Together, the contact stress went from a contact stress of zero within the depression to the first peak contact stress of -13 MPa at the edge of the depression. The magnitude of the contact stress then decreased to a medium value of -10 MPa before escalating towards the second peak at -20 MPa. The contact stress then returned to zero in the gap before increasing again to a final value of -6 MPa.

4.4.4 Three-Dimensional Modeling

Thus far, the finite element simulations of the textures have been axisymmetric models; however, the geometry of the seal and texture are clearly not axisymmetric. The angle of the seal lip surface is a major aspect of the geometry that has been neglected by the two dimensional models presented thus far. A three dimensional model would have the ability to capture the asymmetry in the contact stress distribution as caused by the angled seal lip surface. Furthermore, the three dimensional model would permit non-axisymmetric loading conditions such as the shearing of the seal lip that occurs during seal oscillations.

Therefore, the initial results of a three dimensional model of the hole-bump texture are presented here. A portion of the seal lip has been modeled as shown in figure 4.24. The size of the wedge was based on a texture spacing of approximately 2.5 mm. The mesh was constructed from 20 node hybrid brick elements, and again, for computational simplicity, the Mooney-Rivlin material model was again used. Boundary conditions restrict the mesh from deforming in the 3-direction much like the axisymmetric condition prohibits displacements in the tangential direction. The model is loaded using a displacement bound-

ary condition which deforms the seal model against a rigid surface. The deformed mesh is shown in figure 4.25.

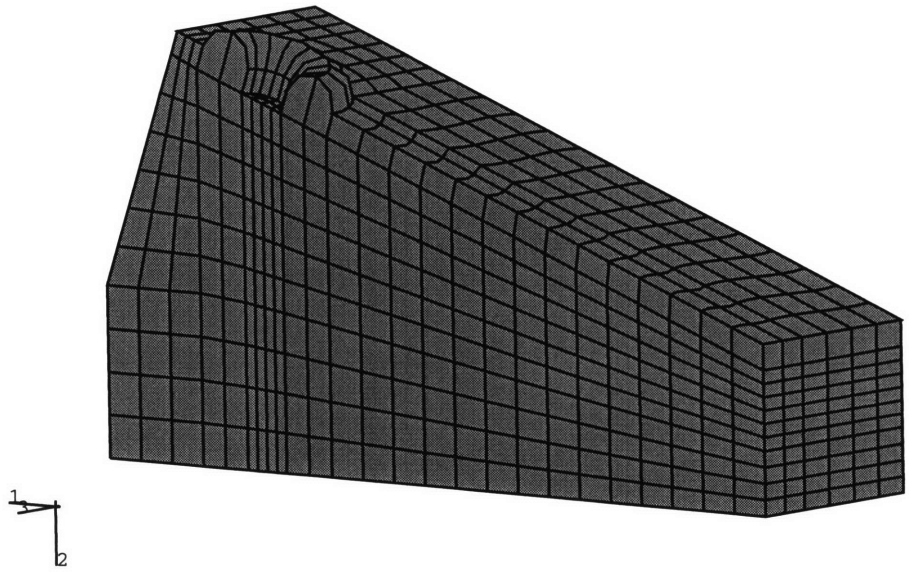

Figure 4.24: 3D finite element mesh of the hole-bump texture.

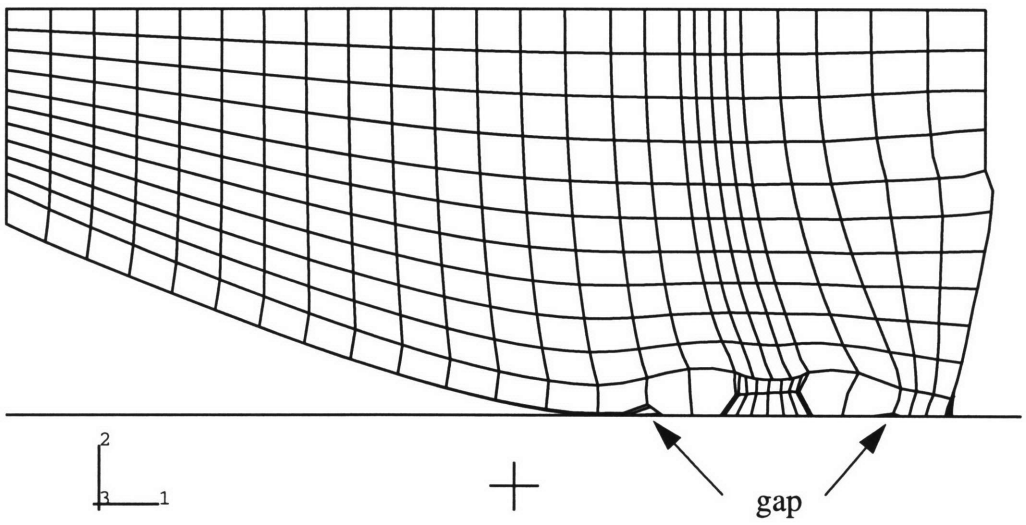

Figure 4.25: Deformed shape of the 3D hole-bump texture.

Again, the contact stress profile is of particular interest. With this model, it is now possible to examine the contact stress profile in all three dimensions and throughout the entire seal lip. A 2-direction stress contour is shown in figure 4.26. It is clear that the angled seal surface concentrates stress at the outer edge of the seal lip, as shown previously in figure 2.9. Thus, the stress distribution around the texture is asymmetric with stress concentrated

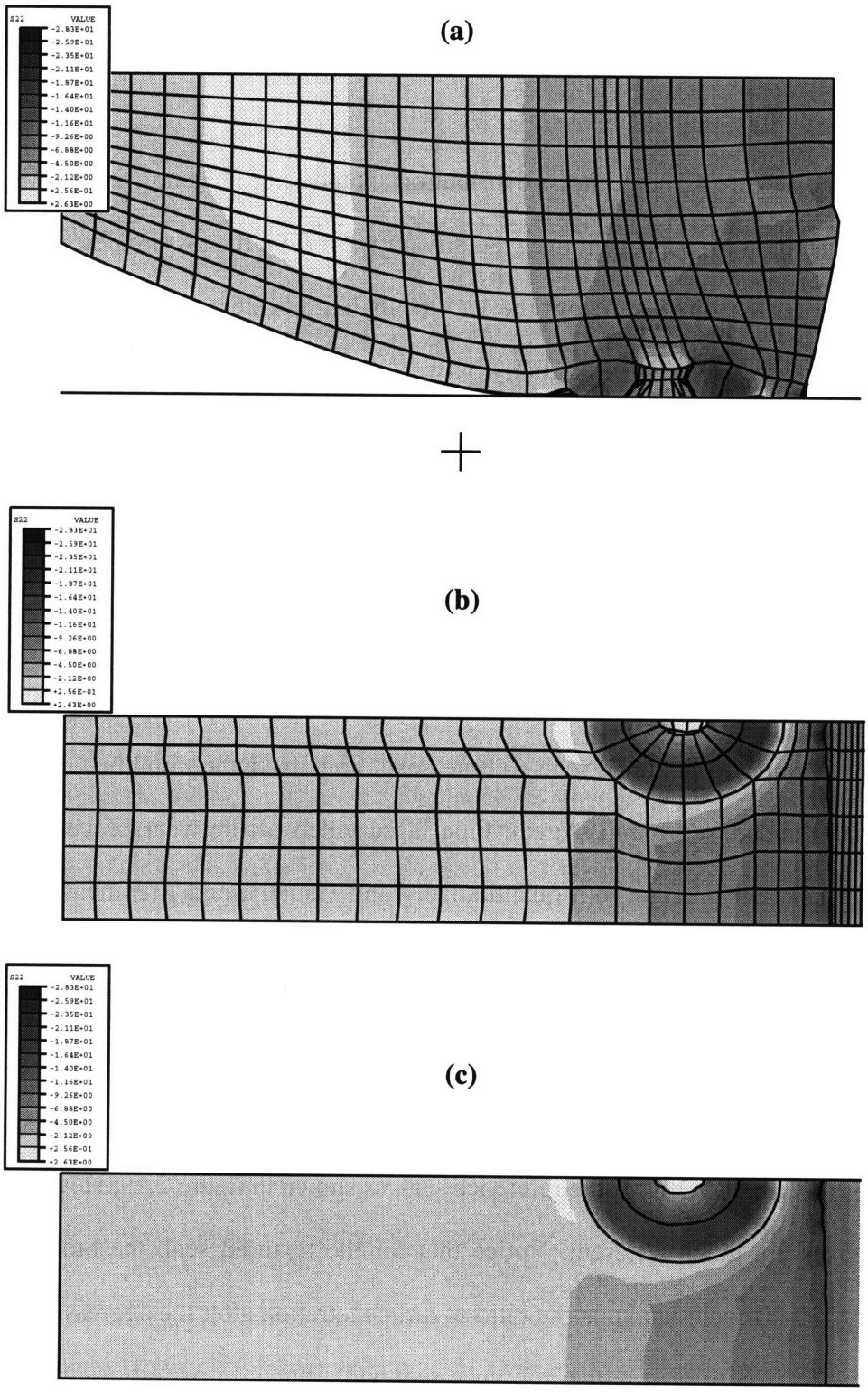

Figure 4.26: 2-direction stress contour of the 3D hole-bump texture model. (a) side view; (b) above texture with element outlines; (c) above texture without element outlines.

towards the outside edge of the texture. A low pressure region surrounds the bump corresponding to the gap at the edge of the bump as pointed out in figure 4.25. Another low pressure region is found inside the depression.

Based on figure 4.23, the stress distribution should return to a uniform contact stress of approximately -8 MPa as one moves radially outward from the texture. Examination of the stress distribution directly below the texture in figure 4.26 reveals that the stress does indeed decrease as one moves radially outward. However, because of the angled seal surface, the stress distribution does not return to a uniform contact pressure for a given radial distance from the texture. Rather, the stress distribution returns to a distribution similar to that for an untextured seal, shown earlier in figure 2.20.

4.5 Experimental Results

This section describes the more recent experimental work of Hugo M. Ayala ([14] and [15]) as applied to textured seals. These seals contained the combination texture of a depression and raised bump. Again, time lapse video of the wear process was used to observe the wear process both quantitatively and visually, and LIF measurements were used to characterize the lubrication profile underneath the seal lip and around each textured feature.

4.5.1 Time Lapse Video of Textured Seals

Figure 4.27 shows the wear data obtained for a textured seal. The general shape of this graph is the same as that for the reference seal, as shown in figure 2.19. However, the scale of the axes are much different. Notice that for the textured seal, the break-in period is roughly 15,000 cycles and that the ratio of dirt penetration after the aggressive wear period is only 7%. In comparison, the reference seal had a break-in period of 7,000 cycles, and the peak dirt penetration ratio was roughly 23%. Thus, the effect of the texture increased

the break-in period by a factor of 2 and reduced the aggressive wear rate by a factor of approximately 5.

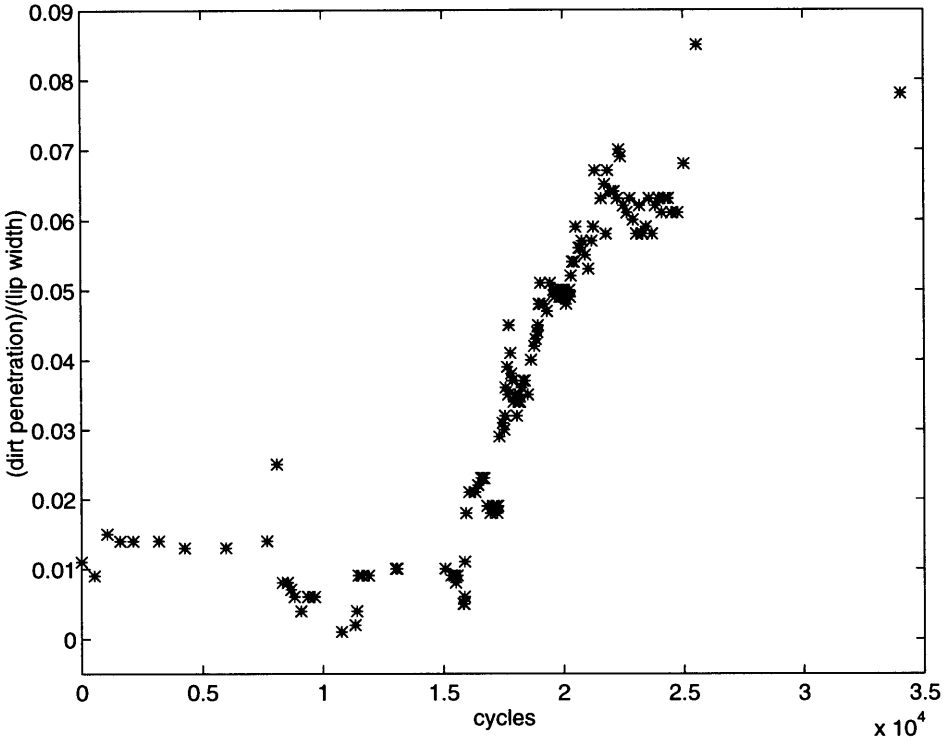

Figure 4.27: In-situ wear measurements of a textured track seal. [14]

Figure 4.28 shows the progression of images taken during the aggressive wear period of the textured seal. A dirt front is clearly visible in these pictures, but over the 6000 cycles that these frames were taken, the dirt front was not able to progress past the bump. This is an extremely important observation as it indicates that the textures do not reduce wear by trapping the particles within the depressions. If particle trapping was indeed the true wear reduction mechanism, one would expect to see particles within the depression at the end of the aggressive wear period. The images in figure 4.28 do not show this to be the case. Also of interest was the undulating contact band profile shown in the same figure. (The contact band profile is outlined by white images which Ayala believes to be air bubbles.) This undulating profile corresponds exactly with the contact pressure profile shown in figure 4.26.

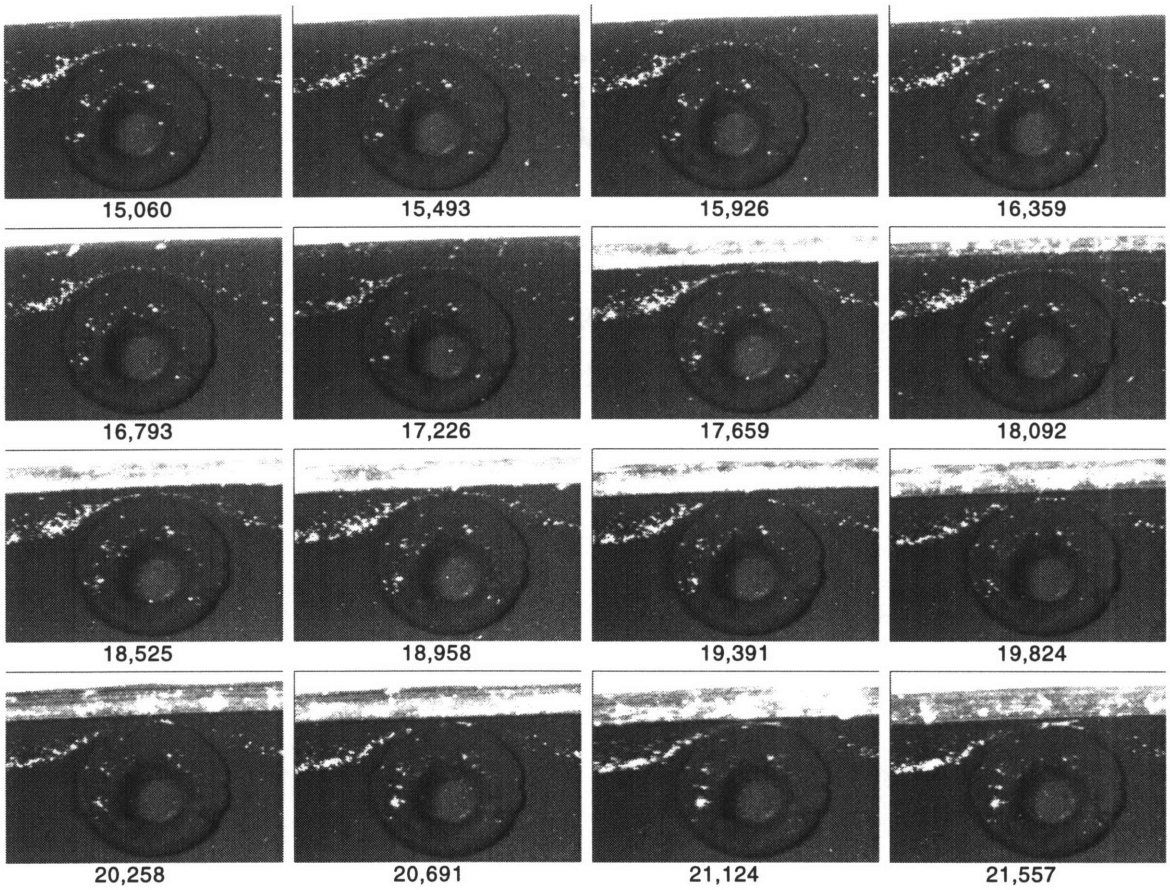

Figure 4.28: Advance of abrasive particles into a textured seal lip contact band. [14]

4.5.2 Laser Induced Fluorescence (LIF)

Figure 4.29 shows a picture of the textures as viewed with LIF. A large amount of oil was located in the center of the texture as expected. Moving from the center of the texture out, the image was progressively darker until the edge of the bump. After the bump, more lubrication was present as evidenced by the lighter images outside the radius of the bump. In particular, there was a bright white circle surrounding the edge of the bump.

Figure 4.29 also includes the contact stress distribution as determined through the three dimensional finite element model. Again, the areas of lowest lubrication in the LIF image corresponded with the areas of highest contact stress. The contact stress was highest at the edge of the bump, and that is where the LIF image was darkest. The lowest contact stresses were inside the depression and in the gap just after the edge of the bump. Accord-

ingly, the LIF image was white in these regions. The bright circle encompassing the bump would seem to indicate the gap predicted in the finite element model.

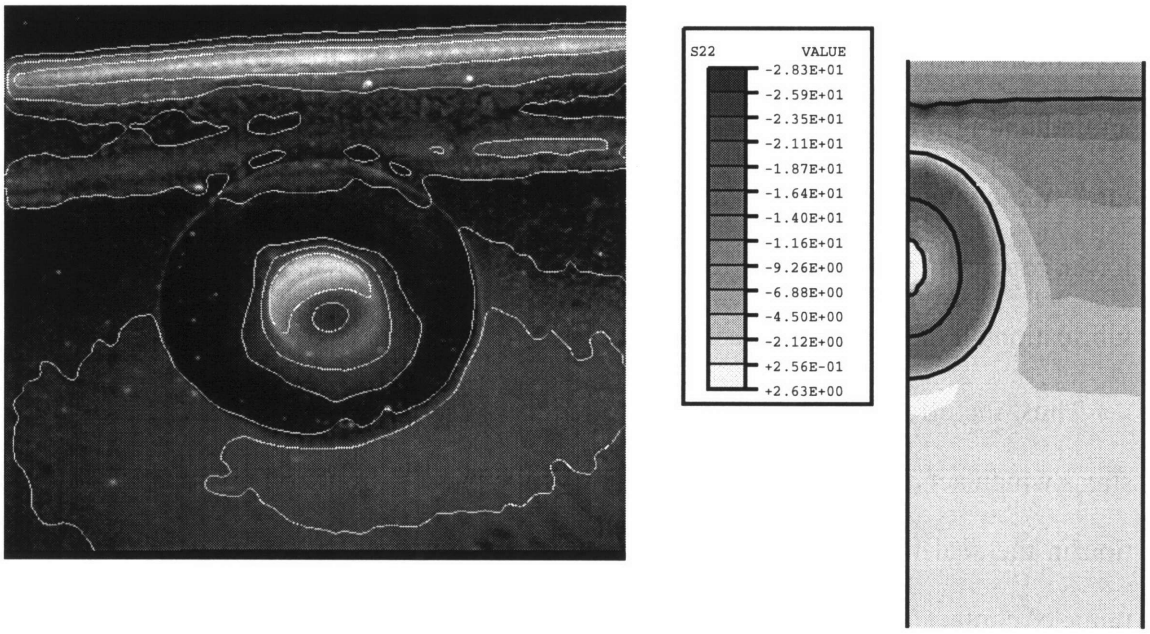

Figure 4.29: LIF image of a hole-bump texture. [14]

4.5.3 Discussion

The LIF images, time-lapse video, and finite element simulations would seem to indicate that the success of the textured seal owes to two main mechanisms: increased contact stress and increased lubrication.

As indicated in finite element simulations, areas of maximum contact stress were found at the edge of the bump textures. Figure 4.28 shows that the dirt front was not able to progress past the bump textures. Thus, the end of the aggressive wear period was marked by the arrival of the dirt front at the edge of the bump texture. This would indicate that the high contact stresses acted as a barrier to particle intrusion.

One might expect that these areas of high contact stress would just wear away. However, the contact stress distributions revealed that the textures successfully positioned areas of relatively low contact stress adjacent to the regions of peak contact stress. This

contact stress distribution placed areas of high lubrication directly next to the areas of high contact stress, thus facilitating lubrication to these high contact stress regions.

Additionally, it was already shown that the contact stress was highest toward the outer edge of the seal contact band. The use of textures, however, altered the contact band into an undulating profile as shown in figures 4.26 and 4.28. In the regions between the textures, the contact band does not reach all the way to the seal lip edge, and so there are lower contact stresses in these regions. These lower stresses can thus facilitate additional lubrication all the way to the seal lip edge.

Thus, the effect of textures is seen to reduce wear by providing areas of peak contact stress which act a barrier to the progression of the particle front and by improving lubrication in the seal lip contact band. Further experimentation would be useful to reveal the range of contact stresses and the amount of lubrication required for successful operation of the seal. With these operating parameters, the trends determined from the parametric finite element studies of the texture as presented earlier could then be used to tailor a contact stress and lubrication profile.

Chapter 5

Modeling Fiber Filled Rubber: Introduction and Motivation

In the previous chapter, modifications to the *geometry* of the seal lip were shown to dramatically improve the wear life of the seal. The use of textures on the surface of the seal lip effectively altered the distribution of contact stresses in a manner which improved lubrication and which provided a barrier to advancing particles. Thus, the texture design improved the wear life of the seal from a purely geometric point of view. The choice of seal material and how it is processed, however, is inherent to issues like contact stresses and wear life. A material's friction coefficient, stiffness, fatigue resistance, and fracture toughness can all greatly contribute to improving the wear life of the seal. The remaining chapters of this thesis concern issues involved with improving the wear life of the seal from a materials point of view.

5.1 Composite Materials

In considering alternate seal lip materials, rubber composites are an attractive option. The use of composite materials has become quite widespread today due to the superior mechanical properties that can be achieved by combining two or more materials. Composites made from ceramic particles with either aluminum or titanium as the base material have been used quite extensively in the defense industry. Carbon fiber reinforced plastics have found many applications in the aerospace industry and even in sports applications such as pole vaults or tennis racquets. Furthermore, the use of filled polymers, particularly fiber reinforced rubbers, has enjoyed great success in the automotive tire industry.

In essence, a composite is simply a mixture of different materials. The base or matrix material is usually the material which represents the largest fraction of the composite. All

other constituents are considered to be the filler materials. The use of composite materials dates all the way back to ancient Egypt where straw and clay were combined for construction purposes [28]. Today, composites are made from a variety of fillers and matrix materials. Different types and shapes of fillers include ceramic particles, rubber spheres, glass fibers or beads, carbon fibers, aramid fibers, and natural fibers such as those found in pineapples or coconuts [27]. Matrix materials range from metals such as aluminums or titanium to polymer thermosets and thermoplastics.

The combination of matrix material and fillers is able to achieve mechanical properties that would otherwise be unattainable by its constituent materials. Thus, composite materials offer two main advantages over conventional materials. First, composites often exhibit enhanced mechanical properties such as improved stiffness, strength, toughness, and wear properties. The second advantage is an additional degree of freedom for the design engineer. With conventional materials, an engineer would *design* a component and *select* a suitable material. With composite materials, the material can be designed as well. An example is the use of specifically oriented fibers which causes the material to behave anisotropically. Thus, the material can be designed to behave very stiff in one direction while at the same time respond compliantly in another direction.

To a lesser degree, composites sometimes offer a cost benefit. These low performance composite materials have enjoyed great success, because the performance gained through the use of a filler may actually allow the use of a cheaper base material. From an economic standpoint then, composite materials can also provide an advantage.

5.1.1 Improved Mechanical Properties

Over the years, researchers in academia and industry have found ways of combining materials to achieve specific mechanical properties. In designing a material suitable for the seal lip, the mechanical properties of modulus, fracture toughness, fatigue resistance, and

wear resistance would all be important issues. The following paragraphs provide examples of the types and application of composites that have been used to improve the above mentioned properties.

An important mechanical property that is often sought through the use of composite materials is an increased modulus. In critical engineering applications where more stiffness is needed, fibers or other fillers are used for reinforcement purposes. Many different types of fillers and fibers are used. For example, in bicycle applications, ceramic particles are used in aluminum to create stiffer, lighter framesets. Additionally, common applications of fiber reinforced rubber composites include automobile tires [30, 31] and transmission V-belts and hoses [32]. Automobile tires are made from different blends of rubber including natural rubber and are sometimes filled with nylon fibers as well as carbon black particles. Transmission belts are often made from chloroprene and polyamide fibers.

Fracture toughness in polymers and cement materials have long been improved through the use of fillers. Work done my Siah, Mandel, and Mousa have modeled and experimentally verified the role of steel fibers in improving the fracture toughness of mortar. Their work identified the primary function of the fiber as improving the mechanical properties of the matrix through crack growth control. Additionally, rubber particles are often dispersed in brittle epoxies to improve toughness [33].

Fatigue resistance is a mechanical property that is very important to the automobile tire industry. Because of the cyclic nature of the loading of tires, materials selected for tire use must display excellent fatigue properties. Short fiber reinforced composites (SFRC) were considered for use in automobile tires [30, 31]; however, the use of fibers to increase stiffness often meant a decrease in fatigue life. In fact, Kwon, et al explicitly stated that they expected that the fatigue resistance of a SFRC would be inferior to that of an unreinforced rubber. Stress concentrations at the interface between the fiber and rubber and heat

generation due to the fibers were cited as the causes for the reduction in life. Stress concentrations would cause debonding or crack initiation, and it was observed that a 10^{o} C increase in operating temperature could double the crack propagation rate. As a result, Kwon, et al conjectured that fibers which exhibited a modulus closest to that of the matrix rubber and which generated less heat would be the most appropriate to use for fatigue life improvements. Of course, the use of a fiber with a low modulus would compromise the benefits of increasing the stiffness of the composite. Of the various fibers tested including nylon, PET, and aramid fibers, it was observed that the use of Nylon 6 fibers more than doubled the fatigue life (760,000 cycles to failure versus 320,000 cycles for the unreinforced rubber). As expected, Nylon 6 displayed the lowest modulus and the least heat generation.

Wear resistance has also been improved through the use of short fiber reinforced rubbers (SFRR). Wada and Uchiyama tested chloroprene filled with polyamide fibers against abrasive papers and metal gauze at different sliding speeds and fiber orientations (sliding longitudally, transversely, and normal to the fibers) [32]. Under all conditions, the SFRR exhibited less wear than the unfilled chloroprene. Wear was minimized when the fibers were abraded in the normal direction, while fibers worn in the transverse direction wore the most. The effect of the type of wear surface used was quite interesting. When the material was abraded against abrasive paper, there was a linear relationship between the wear rate and the contact pressure. However, against the metal gauze, a non-linear relationship was observed. Sliding speed was also observed to have a small effect on the wear rate.

Another group of researchers reported that silicones combined with different types of fillers (including mica, glass fibers and beads, Al_2O_3, Fe_2O_3, and ZnO) all exhibited a critical filler volume fraction, v_c [34]. Below this volume fraction, the wear rate was observed to increase very slowly. After v_c was surpassed, the wear rate increased quite sharply. It

was concluded that high aspect ratios of the length of fiber to diameter as well as poor adhesion properties would lower the value of v_c and that the sharp increase in wear rate after the critical volume had been surpassed was due to the microscopic damage processes of cavitation and debonding.

5.1.2 Modeling Rubber Composite Behavior

From the previous section, it is clear that a SFRR would be an excellent material choice for the seal lip. Fiber reinforced materials were shown to be capable of improving modulus, fracture toughness, fatigue resistance, and wear resistance. While it may not be possible for all four mechanical properties to be improved together, a fiber reinforced rubber certainly seems quite attractive for use in seal applications.

The proper application of such a material, however, demands a thorough understanding of how the fiber filler affects the mechanical behavior of the entire composite. Many different models utilizing finite element analysis or other numerical methods have been used to characterize the behavior of composite materials. Finite element models have been used to make elastic modulus predictions of fiber reinforced cements [35] and to explore how coating fibers can affect the stress and strain distributions within an epoxy matrix [36]. Finite element analysis has also been used in micro-mechanical modeling of steel fibers [37]. Other forms of analysis have been used to examine the compressive strength (stress level before failure) of composites by considering the micro-buckling and kinking of fibers [38, 39].

The most important characteristics of a material being considered for use in a seal lip are probably its wear and fatigue resistance. Fatigue models, such as the one proposed by Kwon et al, cite the stress concentration at the interface between the fiber and matrix as the cause of crack initiation and crack propagation. Therefore, he draws a loose relationship between the stress concentration and the fatigue life of the material and does not consider

the crack arrest features of the fibers. Kwon uses an expression which approximates the stress concentration and simply makes use of it to predict trends in the fatigue life behavior of different composites. For example, the approximation predicted that the stress concentration should increase with increasing volume fractions of filler, aspect ratio (length to diameter), and modulus ratio (fiber to matrix). Using consistent volume fractions and aspect ratios, Kwon did verify experimentally that the fibers exhibiting a low modulus ratio had the best fatigue life. Kwon also draws similar trend predictions through estimations of fiber heat generation.

In terms of wear, much research has been performed to understand the wear phenomena of rubbers and rubber composites. However, because of the complex nature of rubbers, the true underlying mechanisms for wear are still not well understood, and few models for the prediction of wear life have been proposed [34]. Shallamach [25] attempted to relate wear to tearing energy, and Ratner [26] proposed a model which relates the macroscopic mechanical properties of the rubber to the wear loss. Yang, et al's experiments with filled silicone, however, demonstrated that Ratner's model was not able to correctly predict the wear loss in rubber composites [34]. Yang then proposed a model which related wear to a damage zone caused by the filler. Using spherical particles for its symmetry, Yang described the stress field around the particle with equations originally developed by Goodier. A damage volume was then defined as the region around the particle which exhibited a triaxial tension value greater than a phenomenological material parameter. The damage volume was intended to describe the region in which micro-cavitation was occurring. Yang then demonstrated that the relationship between the damage volume and the weight fraction of filler was nearly identical to the relationship between the wear loss and weight fraction of filler.

Clearly, more work can done in the area of modeling the wear behavior of rubber composites. While Yang's model demonstrated predictive capabilities for spherical particles, models for short fibers still have not been proposed. However, even before considering such complicated models of wear, it would seem necessary to be able to actually model the actual behavior of the matrix behavior and the composite behavior. Much work has been performed to estimate properties like the failure strength or elastic modulus of composites, but none predict a simple stress strain curve describing the composite material's response during loading and unloading. In light of the difficulties with modeling the seal materials as discussed in section 2.2.3, investigating this capability seems particularly appropriate.

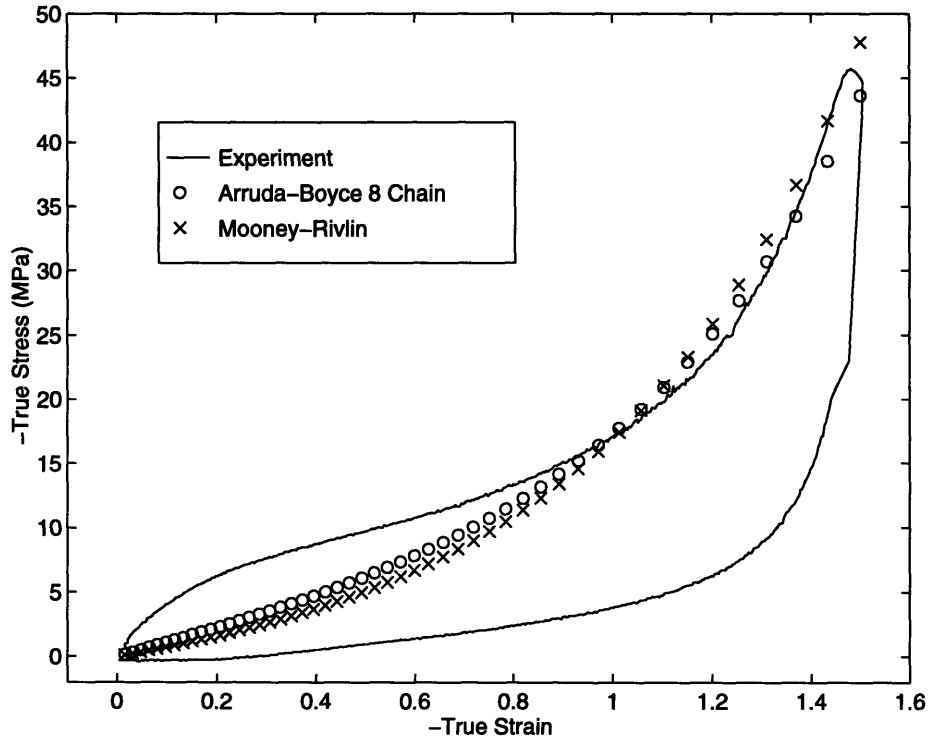

Figure 5.1: Uniaxial compression data for a fiber filled rubber. Predictions of two common constitutive models for rubbers are also shown.

A true stress-true strain curve for a fiber filled rubber placed in uniaxial compression is shown in figure 5.1. Plotted with this data are two rubber elastic model predictions for the behavior of this material: the Mooney-Rivlin and Arruda-Boyce 8 Chain model [16]. Both

of these models are commonly used. However, as clearly shown, neither of these models properly capture the entire response of this composite. In particular, the initial stiffness of the material is not predicted, and because both models are elastic models, no hysteresis is predicted. Clearly, there is a need for a better understanding of how a fiber affects the composite so that better models can be formulated.

In addition to its predictive benefits (which would be extremely valuable from a design viewpoint), such a study could then provide insights into our issues of major interest, namely the wear and fatigue resistance of the composite. A fundamental model could provide a means to investigate the problems normally associated with wear and fatigue such as the stress concentration at the interface, crack initiation, and debonding. Furthermore, these issues could stimulate further understandings which could be useful in the actual manufacturing and processing of components made from fiber reinforced rubbers.

5.2 Outline

Thus, the study of fiber filled rubbers has become quite important from a design, process, and end use point of view and is considered in the second half of this thesis. This section of the thesis seeks to lay foundation work for a more extensive study specifically aimed at modeling and understanding the wear behavior of fiber filled rubbers in an effort to improve wear life. In particular, the following chapters will explore modeling the plane strain compression response of short fiber reinforced rubbers through a unit cell finite element model.

First, experimental results are presented for a polyurethane filled with glass fibers in uniaxial and plane strain compression. General trends of the stress-strain curves are discussed and serve as a basis for the discussion of the different material models that will be considered.

Before assembling a model of the behavior of the composite material, the ability to model each constituent material's behavior should be demonstrated. To this end, chapter 7 discusses various constitutive material models that can be used to model the matrix material. Different aspects of the behavior of unfilled polyurethane and the difficulties encountered in modeling them are both discussed.

A simple unit cell finite element model of a fiber filled rubber is then described, and two sets of results are shown. The first set of results were obtained by using a simpler base material model in order to qualitatively explore the fiber-matrix material interaction. In particular, the effects of the initial angular orientation of the fiber are discussed. The second set of results made use of the elastic-visco plastic constitutive model [18], and the size of the unit cell was adjusted to correspond with the volume fractions of fibers used in the experiments. Though more difficult computationally, this model provided excellent predictions of the experimental data. With confidence that the unit cell model could accurately predict the stress-strain behavior of fiber filled rubbers, the stress and strain distributions within the unit cell are then examined in an attempt to draw connections with wear and fatigue models.

Chapter 6

Uniaxial and Plane Strain Compression Testing

This chapter presents the experimental data for a polyurethane filled with three different volume fractions of glass fibers. The stress strain curves presented here in uniaxial and plane strain compression will serve as a basis for discussing various constitutive models in later chapters. The data will also be used to determine the usefulness of the unit cell finite element model in predicting the mechanical response of fiber filled rubbers.

6.1 Material Samples

Glass fibers are extremely common fiber fillers because of their low cost. These fibers exhibit excellent mechanical properties such as high strength, low weight, excellent insulation properties, and high corrosion resistance. Similarly, polyurethane elastomers have been used in nearly every industry because of attractive properties such as excellent wear and weather resistance and good mechanical behavior over a wide range of temperatures. Thus, a composite of a polyurethane matrix with glass fibers can be considered a generic example of a fiber filled rubber.

The material used for this investigation was therefore a polyurethane filled predominantly with glass fibers. Amounts of carbon black and other fillers were also present, as evidenced by the black color of the samples; however, the dominant fillers were the glass fibers. The polyurethane had a glass transition temperature, T_g, of -16^o C as provided by the supplier, and the glass fibers were milled fibers of the "E" composition. This composition represents the most common glass fiber used in reinforcement applications.

Uniaxial and plane strain compression samples were prepared from unfilled polyurethane and polyurethane filled with two different volume fractions of glass fiber. The single filled fiber volume content was 4%, and the twice filled fiber content was 8%. The glass

fibers are assumed to be randomly oriented. SEM micrographs of the material are shown in figure 6.1.

The samples were prepared from sheets of the material that were 3.3 mm in thickness. Uniaxial compression samples were punched from the sheet and had an average diameter of 14.25 mm. Two of these discs were stacked, resulting in a sample with a height to diameter ratio of 0.46. Plane strain samples measured 9.6 mm by 10.5 mm on average and were cut from the same sheets.

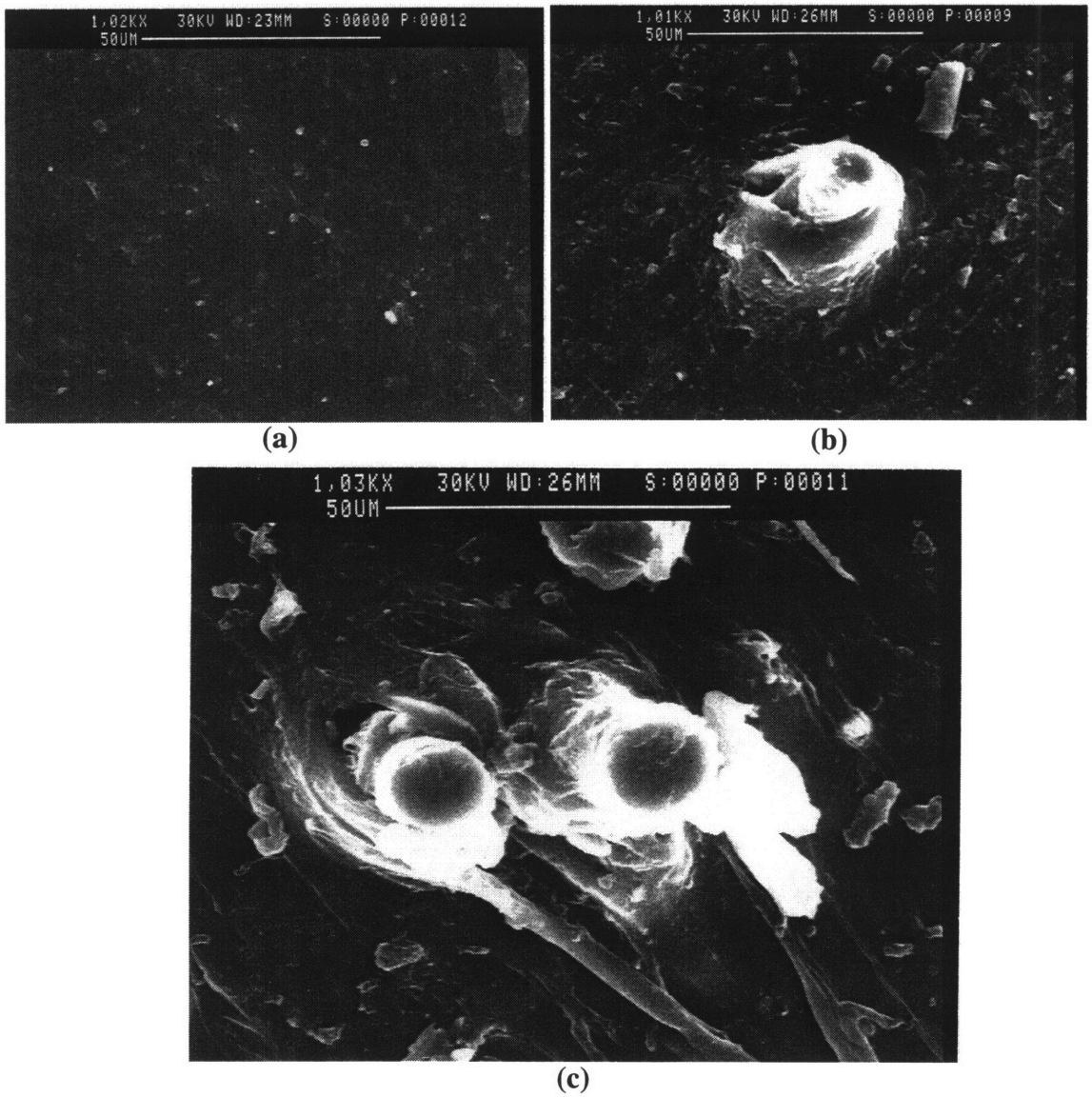

Figure 6.1: SEM micrographs of the unfilled, singled filled, and double filled polyurethane samples.

6.2 Experimental Procedure

All testing was done on an Instron mechanical testing machine. For direct comparison, tests were performed at room temperature and at a constant strain rate of -0.01 mm/mm. Data is shown for new samples. In other words, no initial straining was performed on the samples. For modeling purposes however, additional tests were performed at different strain rates and with pre-strained samples.

For uniaxial compression tests, the discs of material were roughened slightly before testing to prevent slippage from occurring between the samples. Sheets of teflon were used between the sample and Instron grips to prevent friction. Tests were run to final strains of -1.5 initially, but a fair amount of friction made the results at very high strains somewhat unrepeatable. Therefore, tests were re-run to final strains of -1.3.

For plane strain compression tests, a plane strain die was used as shown in figure 6.2. To reduce friction, teflon was again used, but because plane strain tests are highly sensitive to friction, lubricant (WD40) was also applied between the die and the sample. Tests were performed to final strains of -0.65. This moderate final strain was selected for direct comparison with the finite element simulations which will be discussed later in this chapter.

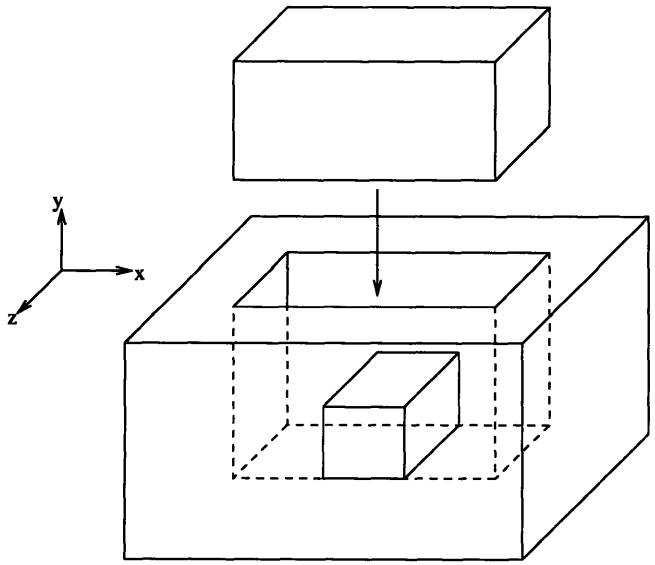

Figure 6.2: Plane strain die used in plane strain compression experiments.

6.3 Results

6.3.1 Uniaxial Compression Results and Discussion

The uniaxial compression results are shown in figure 6.3. The effect of glass fiber reinforcement was quite evident. The presence of fibers increased the initial stiffness of the material to a small degree and dramatically increased the amount of hardening at high strains.

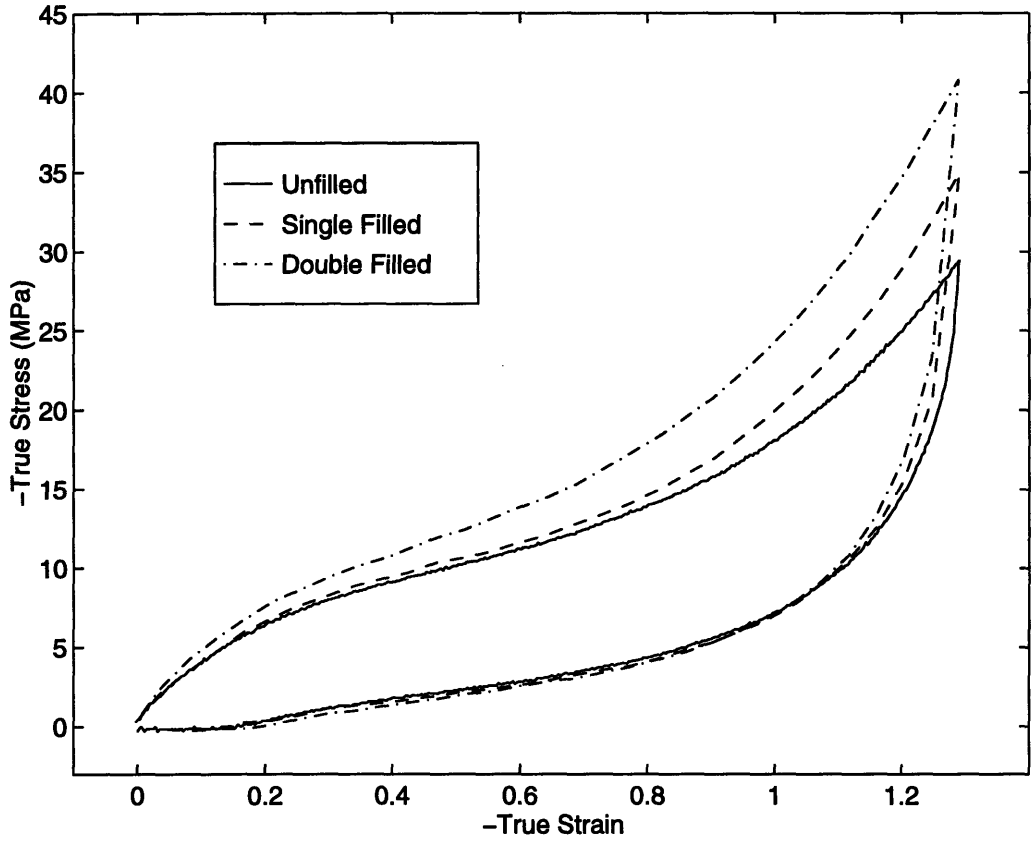

Figure 6.3: Uniaxial compression results for polyurethane filled with three different volume fractions of glass fibers: 0, 0.04, and 0.08.

The loading behavior of the unfilled material can be split into three regimes: initial stiffening, modulus reduction, and hardening. The experimental result showed an initial modulus of approximately 35 MPa until a strain of approximately -0.15. After this point, the tangent modulus of the material decreased to approximately 10 MPa. After a strain of about -0.8, the material then began to harden, as indicated by the upward curve of the stress-strain response at the high strains.

For strains below -0.8, the single filled and unfilled material responses were nearly identical. The 4% fiber content did not contribute any significant stiffening to the initial modulus nor did it change the drop in stiffness observed over the moderate strain range (-0.1 to -0.6). Above -0.8 strain, however, the single filled material began to harden at a much higher rate than the unfilled material. Final stresses for the single filled material were approximately -34.5 MPa, compared to -29.5 MPa for the unfilled material. Qualitatively, the upward hardening curve was much sharper for the single filled material.

The effect of the doubled fiber content was noticeable from the outset. The initial modulus was stiffened to about 40 MPa, and even the reduced tangent modulus was increased to approximately 16 MPa. Hardening occurred at a strain of approximately -0.8 again, and the final stresses reached were approximately 40.6 MPa.

From the uniaxial compression data, the amount of fiber content affects the material response in a nearly linear fashion. The increase in final stress for unfilled and single filled materials was approximately 5 MPa, and the increase between single filled and double filled final stresses was approximately 6 MPa. Additionally, it is interesting to note the final hardening slopes (the slope of the stress-strain curves at the final strain of -1.3) for the single filled and doubled filled materials were both approximately 66 MPa. However, the single filled material showed no significant change in initial modulus, whereas, the double filled material showed a stiffer initial modulus.

6.3.2 Plane Strain Compression Results and Discussion

Plane strain compression results are shown in figure 6.4. Data from these experiments illustrated even more clearly the effect of fiber reinforcements on initial stiffness and hardening. Qualitatively, the trends were the same as in the uniaxial compression experiments; however, the effect of fiber content is more distinctly shown in the plane strain results because of the separation between the single filled and unfilled material responses.

Initial moduli were 40 MPa for the unfilled material, 44MPa for the single filled material, and 55 MPa for the double filled material. Final stresses were 18.3 MPa for the unfilled material, 23 MPa for the single filled material, and approximately 30 MPa for the double filled material. The plane strain compression samples clearly show a difference in the increases in final stress between the unfilled and single filled materials and between the single filled and double filled materials. This data would then suggest that the amount of fiber content has a non-linear effect on the composite's mechanical response in plane strain compression.

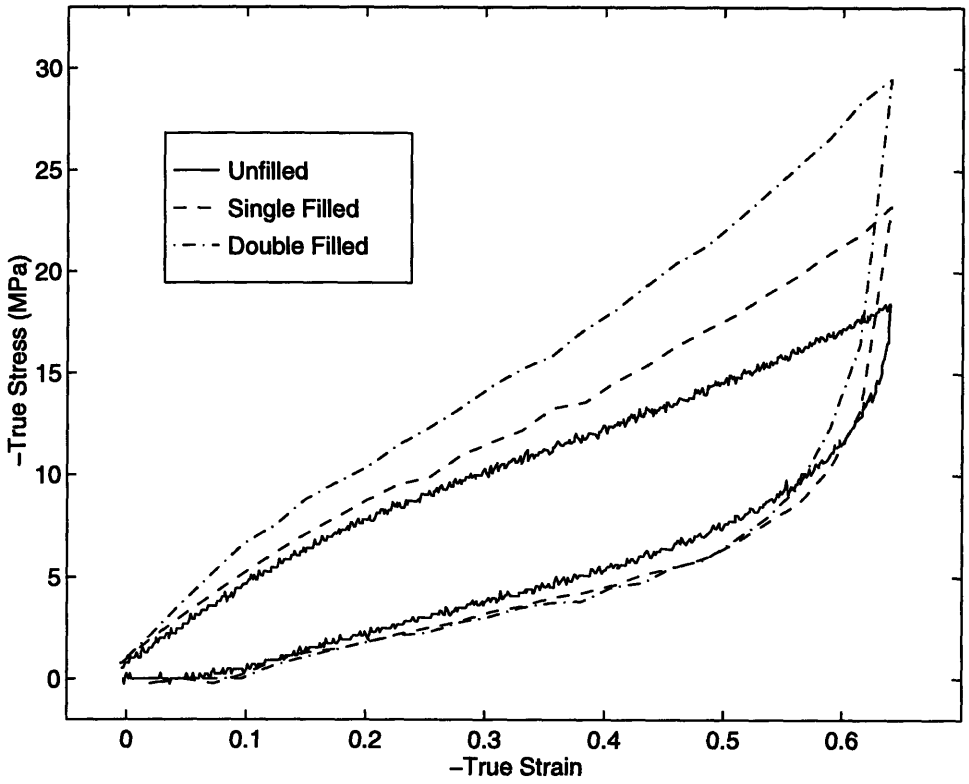

Figure 6.4: Plane strain compression results for polyurethane filled with three different volume fractions of glass fibers: 0, 0.04, and 0.08.

6.3.3 General Observations

It should be noted that in both uniaxial and plane strain compression, a significant amount of permanent deformation was exhibited. For the uniaxial experiments, a final strain of -1.3 caused permanent set of approximately 0.16 strain. For the plane strain experiments, a final strain of -0.65 caused a permanent set of approximately 0.09 strain. It

is interesting that the permanent deformation was independent of fiber content. Additionally, the shape of the unloading portion of the stress strain curve was very similar for all samples regardless of fiber content. This behavior was seen in both uniaxial and plane strain compression.

The permanent deformation was a major reason that only new samples were used in the experiments. Indeed, the occurrence of such a significant level of permanent strain indicates that this material is not deforming in a purely elastic manner. Rather, the material also exhibits plasticity during the course of the deformation. The occurrence of plastic deformation also suggests an inappropriateness of using traditional rubber elastic constitutive modes when attempting to model the behavior. The inadequacy of such models will be demonstrated and discussed in the next chapter.

In order to further explore the effect of prior deformation and permanent set on subsequent responses, materials were subjected to stress-strain testing subsequent to a previous deformation. Figure 6.5 shows two stress-strain curves for a sample of unfilled polyurethane. The solid curve corresponds to data obtained for a new sample. In this experiment, a sample that had not been previously tested was compressed uniaxially to a final strain of -1.5 at a strain rate of -0.01 s^{-1}. The dashed curve corresponds to data taken from the same material sample approximately 3 hours after the first experiment. Figure 6.6 shows an identical graph for a polyurethane filled with a fiber volume fraction of 4%.

Both figures clearly indicate that while the unloading behavior is identical for both samples, the loading behavior is drastically different. The data corresponding to the previously loaded material exhibits a much softer initial stiffness, nearly 3 times softer. This resembles the well known Mullins Effect [20]. However, the Mullins Effect is usually observed with no permanent deformation; both curves in figure 6.5 exhibit a permanent deformation of approximately 0.2. Thus, the softer response of the second experiment is

due partly to the Mullins Effect but also to the effect of permanent deformation after the first experiment. Studies have been performed which explore the anisotropic behavior that results from pre-straining a material sample [39]. However, that particular study investigated this effect in glassy polymers.

Additionally, it is noted that the tangent modulus over the moderate strain range (-0.2 to -0.6) was similar for both the new sample and the previously loaded sample. However, the final stresses for each experimental trial were similar. Thus, the hardening slope was intensified for the previously loaded material sample. This was observed for both the filled and unfilled polyurethane.

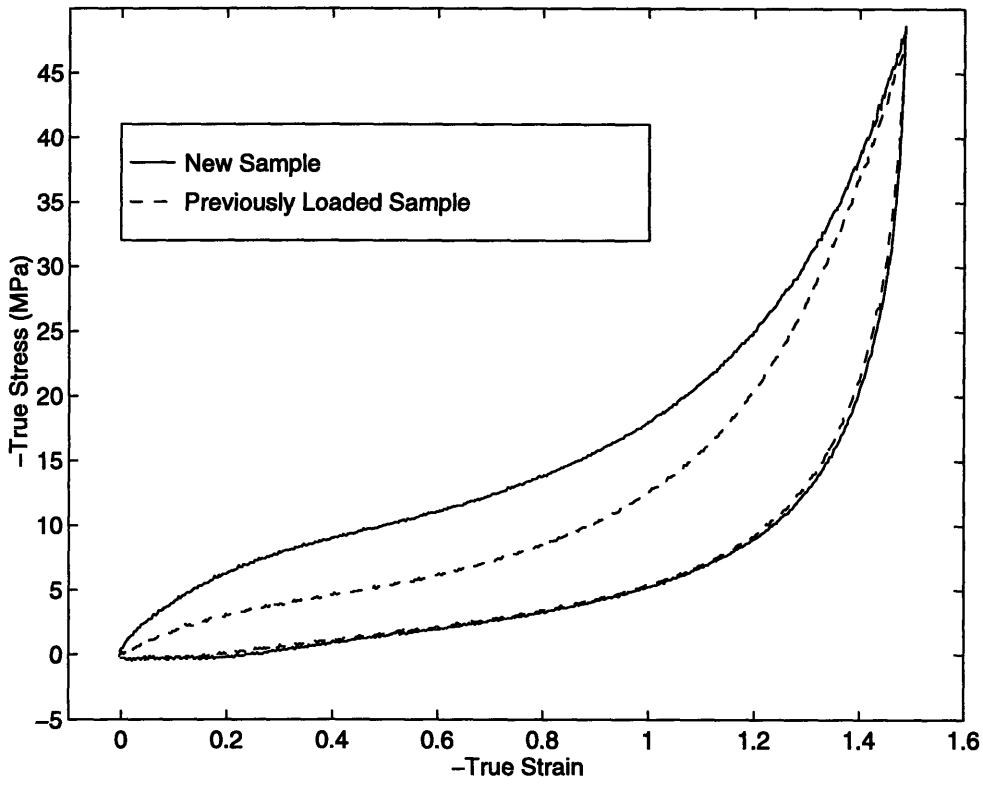

Figure 6.5: Uniaxial compression responses of unfilled polyurethane. The solid curve corresponds to an initial experiment, while the dashed line represents a subsequent experiment using the same sample.

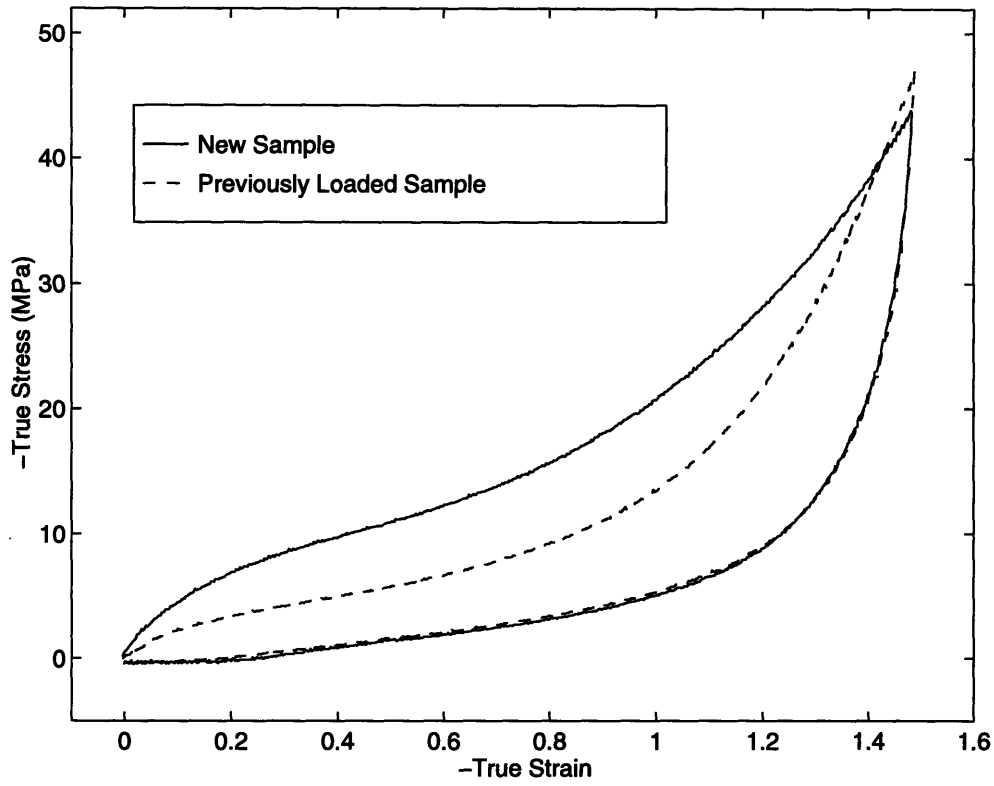

Figure 6.6: Uniaxial compression responses of a polyurethane filled with fibers at a volume fraction of 4%. The same sample was used for each data curve.

Chapter 7

Material Models

In order to assemble a finite element model simulating the behavior of a fiber filled rubber, appropriate material constitutive models are needed for both the matrix material and the fiber. The fiber is rather simple to model, but there are many complications involved in the modeling of the matrix material. In this section, a comparison is shown between the experimental data and the following constitutive models: the Mooney-Rivlin Model [16], the Arruda-Boyce Eight Chain Model [19], the Arruda-Boyce elastic-visco plastic polymer constitutive model [18], and a dual network model as proposed by Bergstrom [40]. These models are summarized, and their difficulties in capturing the polyurethane material behavior are discussed.

7.1 Glass Fiber Material Model

The glass fiber is of the "E" type composition, and its properties are easily found in standard tables. The fiber is modeled as an isotropic linear-elastic material with a Young's Modulus, E, of 72.5 GPa, and a Poisson's ration, ν, of 0.22.

While the brittleness of glass is fully recognized, no attempt is made to model this aspect of the mechanical behavior. For reference, however, the yield strength is listed as 3.45 GPa corresponding to a yield strain of 0.048. One would expect brittle fracture soon after this yield strain.

7.2 Comparison of Rubber Elastic Constitutive Models with Matrix Material Experimental Results

7.2.1 Rubber Elastic Stretch Invariant Models

In this section, the uniaxial compression stress-strain behavior of the unfilled polyurethane material is compared against two rubber elastic constitutive models, namely the

Mooney-Rivlin and Arruda-Boyce Eight Chain models. The Mooney-Rivlin model is a stretch invariant based model, and the Arruda-Boyce model is based on statistical mechanics but can be reduced to stretch invariant form. A stretch invariant based model provides a strain energy expression that is written in terms of functions of the general stretches. These functions are constant under orthogonal transformations and are thus called the stretch invariants. The three stretch invariants are:

$$I_1 = \lambda_1^2 + \lambda_2^2 + \lambda_3^2 \tag{7.1}$$

$$I_2 = \lambda_1^2\lambda_2^2 + \lambda_2^2\lambda_3^2 + \lambda_1^2\lambda_3^2 \tag{7.2}$$

$$I_3 = \lambda_1^2\lambda_2^2\lambda_3^2 \tag{7.3}$$

where λ_1, λ_2, and λ_3 are the three principal stretches.

Because rubbers are generally considered to be incompressible, I_3 has a value of one. Thus, the strain energy expression provided by these two models reduces to a function of the first two stretch invariants. Second partial derivatives of the strain energy function provide the matrix of elastic constants which relate stress to strain:

$$\sigma_{ij} = C_{ijkl}\varepsilon_{kl} = \frac{\partial^2 W}{\partial\varepsilon_{ij}\partial\varepsilon_{kl}}\varepsilon_{kl} \tag{7.4}$$

Because these models are completely elastic, the strain energy expression is all that is needed to prescribe the constitutive behavior.

7.2.2 Mooney-Rivlin Model

The Mooney-Rivlin Model is a phenomenological model which expresses the strain energy function in the following form:

$$W = C_1(I_1 - 3) + C_2(I_2 - 3) \tag{7.5}$$

where C_1 and C_2 are the parameters and are found by fitting the model to experimental data. In figure 7.1, the uniaxial compression data for unfilled polyurethane is plotted against the Mooney-Rivlin model predictions. In this figure, the Mooney Rivlin prediction

was determined with parameter C_1 equal to 2.5 MPa and parameter C_2 equal to 0.45 MPa.

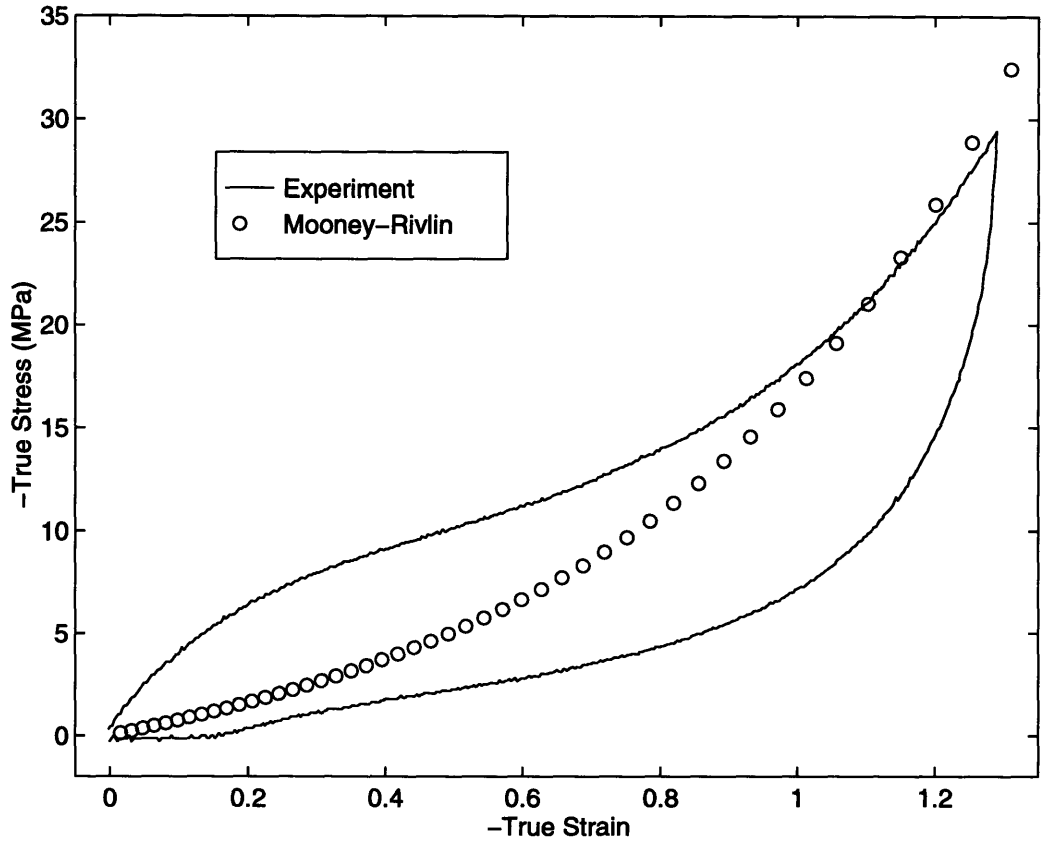

Figure 7.1: Mooney Rivlin model predictions for the uniaxial compression behavior of unfilled polyurethane.

7.2.3 Arruda-Boyce 8 Chain Model

The Arruda-Boyce 8 chain model is based on a unit cube in which eight non-Gaussian chains are united at the center, as shown in figure 7.2. Each chain extends from the center of the cube to one of the eight corners. Because of this symmetry, all eight chains undergo the same deformation during different types of loadings. This symmetry is the essence of the model and provides its computational simplicity.

Each chain in the unit cube is represented as a Langevin statistical chain to account for large deformations. The strain energy is proportional to entropy changes due to deformation since enthalpy considerations are negligible. Thus, the change in entropy is expressed for a deformed chain as a function of the inverse Langevin function and the chain vector

length, r_{chain}. The chain vector length and Langevin function itself are expressed as follows:

$$r_{chain} = \frac{1}{\sqrt{3}}\sqrt{N}l(\lambda_1^2+\lambda_2^2+\lambda_3^2)^{\frac{1}{2}} = \frac{1}{\sqrt{3}}\sqrt{N}lI_1^{\frac{1}{2}} \tag{7.6}$$

$$Langevin[\beta] = (\coth\beta)-\left(\frac{1}{\beta}\right) \tag{7.7}$$

The chain vector length, r_{chain}, is expressed in terms of the principal stretches based on the geometry of the deformed eight chain network. As seen in equation 7.6, the resulting r_{chain} is proportional to I_1, and thus, the resulting strain energy expression is a function of I_1 only. $\sqrt{N}l$ represents the initial chain length. The strain energy expression may be written in terms of equations 7.6 and 7.7 as:

$$W = nk\Theta\left(\frac{r_{chain}}{Nl}\beta + \ln\frac{B}{\sinh B}\right)-\Theta c' \tag{7.8}$$

where n is the chain density, k is Boltzmann's constant, Θ is the temperature, and c' is a constant. Differentiation of W then leads to the following stress-stretch relationship written in terms of a difference between two principal stretches in order to cancel the constant pressure term:

$$\sigma_1-\sigma_2 = \frac{nk\Theta}{3}\sqrt{N}Langevin^{-1}\left[\frac{\lambda_{chain}}{\sqrt{N}}\right]\frac{(\lambda_1^2-\lambda_2^2)}{\lambda_{chain}} \tag{7.9}$$

where λ_{chain} is r_{chain} divided by the initial length. If a series expansion form of the inverse Langevin function is used, equation 7.9 can be integrated to arrive at a polynomial form of the strain energy function. The first five terms are shown below:

$$W = CR\left[\frac{1}{2}(I_1-3)+\frac{1}{20N}({I_1}^2-9)+\frac{11}{1050N^2}({I_1}^3-27)+\frac{19}{7000N^3}({I_1}^4-81)+\frac{519}{673750N^4}({I_1}^5-243)\right] \tag{7.10}$$

where CR and N are the two parameters for this model. CR is roughly the chain density multiplied by Boltzmann's constant, k, and the temperature, while $\sqrt{N}$ is a measure of the

maximum stretch attainable by the chain.

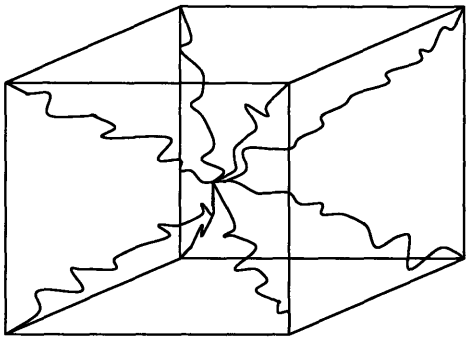

Figure 7.2: Eight chain unit cube configuration.

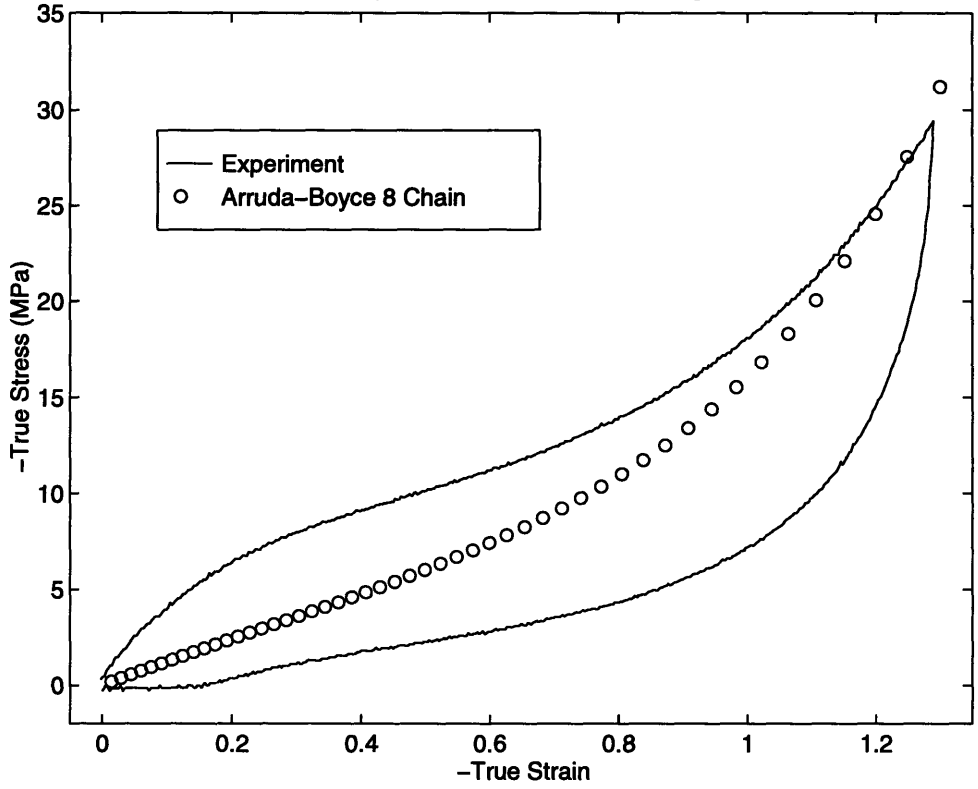

Figure 7.3: Arruda-Boyce 8 Chain model predictions for the plane strain compression behavior of unfilled polyurethane.

In comparing this model with the unfilled polyurethane data, CR was taken to be 3.32 MPa, and N was equal to 2.9. These factors were found by first adjusting N until the shape of the hardening was well matched to the experimental data. After N has been determined, CR is adjusted until the magnitude of the stress response is suitable and until the initial slope of the stress-strain curve is matched. Because of the particular behavior of this poly-

urethane, matching the initial modulus was not possible.The model fits to the data as shown in figure 7.3.

7.2.4 Discussion of Model Predictions

As seen in figure 7.1 and 7.3, these two models are not able to capture the entire material response of the unfilled polyurethane. Because they are elastic models, they inherently cannot capture the hysteresis displayed by the material. The models are able to capture the hardening behavior of the material at higher strains, but they also neglect the initial stiffness and subsequent softening behavior. In addition, the models incorporate neither time nor temperature dependence.

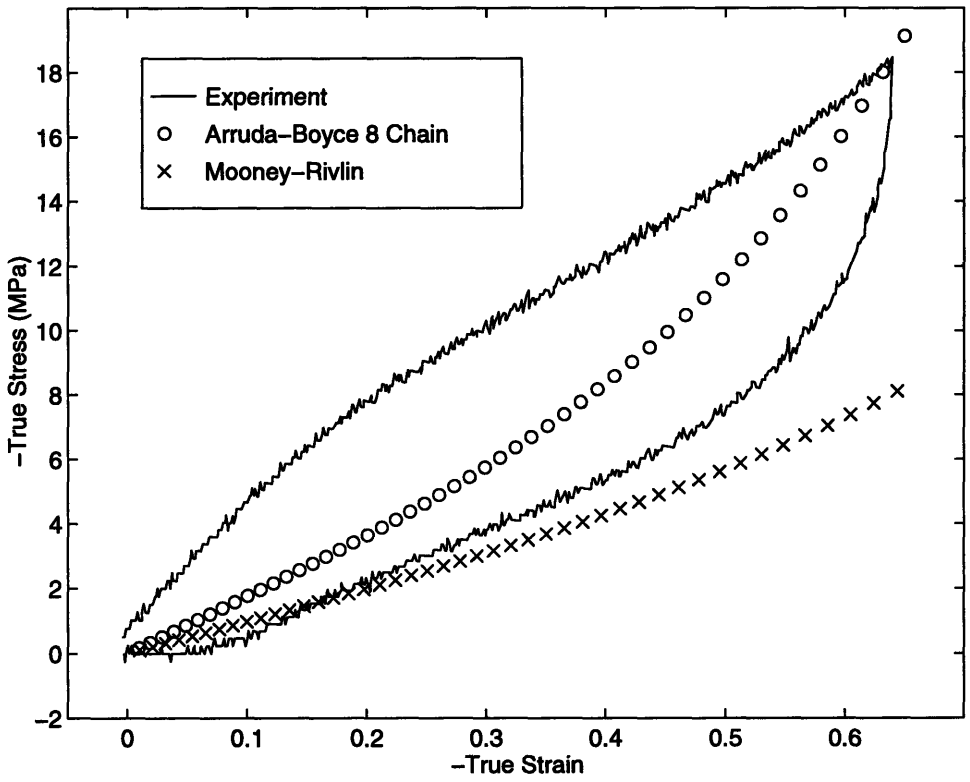

Figure 7.4: Arruda-Boyce 8 Chain and Mooney-Rivlin model predictions for the plane strain compression behavior of unfilled polyurethane.

Figure 7.4 plots the plane strain compression predictions of the model versus the experimental data. For the model predictions, the identical parameters that were used to fit the uniaxial compression data were used. Because the uniaxial fits were so approximate, it is hard to expect that the plane strain compression predictions would be accurate espe-

cially at small strains. It appears that the Arruda-Boyce 8 Chain model will eventually capture the plane strain hardening response at higher strains; however, it is clearly shown that the Mooney-Rivlin model severely underpredicts the behavior of the material in plane strain compression. As in the uniaxial compression case, neither model has the ability to capture the initial stiffness of the material.

7.3 Comparison of Elastic-Visco Plastic Model with Matrix Material Experimental Results

7.3.1 Elastic-Visco Plastic Model

The elastic-visco plastic model under consideration here is that which was first proposed by Boyce, Argon, and Parks in 1988 [18]. The essence of this model is captured in a one dimensional representation of its three major components as shown in figure 7.5. This model consists of a spring element that is in series with a parallel structure between another spring element and a dashpot element.

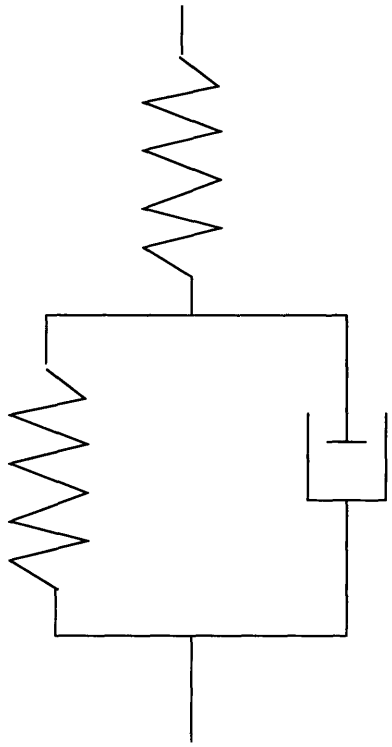

Figure 7.5: One dimensional representation of the three components of the elastic-plastic model.

The parallel structure is considered first. The dashpot is a rate and temperature dependent term which governs plastic flow. This component models the isotropic resistance to chain segment rotation of the material and is expressed in terms of an activation energy barrier Arrhenius expression:

$$\dot{\gamma}_P = \dot{\gamma}_o \exp\left(-\frac{As}{k\theta}\left\{1-\left(\frac{\tau}{s}\right)^{\frac{5}{6}}\right\}\right) \tag{7.11}$$

where $\dot{\gamma}_P$ is the plastic shear strain rate, $\dot{\gamma}_o$ is a pre-exponential factor which is proportional to the attempt frequency, s is the athermal shear strength, As is the zero stress level activation energy, τ is the effective equivalent shear strength, k is the Boltzmann's constant, and θ is the absolute temperature. The athermal shear strength is defined as:

$$s = 0.15\mu = \frac{0.15}{2(1+\nu)}E \tag{7.12}$$

where μ is the elastic shear modulus, and ν is the Poisson's ratio. When examining this expression, it is clear that the τ/s is the key to the "activation" of this component. As the effective shear strength approaches the athermal shear strength, the coefficient of the exponential approaches zero, and the entire term approaches the pre-exponential factor which is usually on the order of 1e+13 s^{-1}.

The spring element which is in parallel with the dashpot represents the anisotropic resistance to chain alignment. The spring is modeled as a non-linear rubber elastic spring element, and the considered rubber elasticity model is the Arruda-Boyce 8 Chain model as proposed by Arruda and Boyce [19]. This spring component is considered to be the "back" stress of the parallel structure, since it opposes the effect of the dashpot. The stress acting on the dashpot is called the "driving" stress.

Finally, the series spring element is simply a linear elastic spring with stiffness k.

Qualitatively, the effect of each component is easily understood. Referring back to the experimental data, the linear elastic spring provides the initial stiffness response. As soon as the dashpot element "activates," the softening behavior occurs. As evidenced by the permanent deformation that occurred after unloading, this softening behavior can be thought of as yielding. At the higher strains, the eight chain model provides the hardening. When the material is unloaded, the unloading modulus is determined solely by the linear elastic spring. The material unloads along this path until the effect of the dashpot is again realized. After this event, the unloading slope of the stress strain curve becomes much more gradual, mimicking the softened modulus of the loading response.

Thus far, the elastic-visco plastic model has been described in one dimension so that the contributions of the elements can be more easily understood. In order to formulate the entire constitutive model in three dimensions, the individual contributions must be thought of in terms of finite strain deformation continuum mechanics [18]. After the three dimensional equations have been formulated, the model can be coded as a user defined material, or *UMAT, to interface with the ABAQUS finite element solution routine. The *UMAT requires calculating and returning values for the incremental stress and the Jacobian matrix.

7.3.2 Determining Model Parameters

For the purposes of modeling this unfilled polyurethane, the elastic-visco plastic model requires that 6 parameters be inputted: the linear elastic behavior governed by E and ν; the visco-plastic flow behavior governed by $\dot{\gamma}_o$; and As; and the strain hardening behavior governed by CR and N.

In order to find these constants, experimental data is required at two different strain rates. E, the initial modulus is found by finding the initial slope of the stress strain curve before the modulus reduction has occurred. This constant completely defines the linear

elastic spring element. Attention is now turned to the dashpot element. τ is estimated through the Mises relationship as being $Y/\sqrt{3}$, where Y is the tensile "yield" stress of the material. Similarly, $\dot{\gamma}_P$ is estimated as the strain rate times $\sqrt{3}$. The athermal shear strength can be estimated as expressed in equation 7.12 with ν equal to 0.48 since rubbers are near incompressible. In modeling this rubbery material, however, it was found that a larger s value yielded a better prediction of the material behavior. Two constants remain undefined: As and $\dot{\gamma}_o$. In determining these two parameters, equation 7.11 can be expressed as follows:

$$C1(As) + C2 - \ln\dot{\gamma}_o = 0; C1 = \frac{\left(1 - \left(\frac{\tau}{s}\right)^{\frac{5}{6}}\right)}{k\theta}, C2 = \ln\dot{\gamma}_P \tag{7.13}$$

By using the data at two different strain rates, two equations of the form of 7.13 can be written in the two unknowns that are being sought. The two equations can be solved simultaneously, and As and $\dot{\gamma}_o$ can be determined. The final two parameters to be determined are CR and N. The procedure is the same as described before.

7.3.3 Discussion of Model Predictions

Model Parameter	Value
E	47 MPa
ν	0.48
s	5.8 MPa
As	1.89e-19 J
$\dot{\gamma}_o$	1.4365e5 s^{-1}
CR	2.25 MPa
N	1.59

Table 7.1: Model parameters used in the elastic-visco plastic model.

In figure 7.6, the uniaxial compression stress strain curve for unfilled polyurethane is plotted against the elastic-visco plastic model prediction. The model parameters used in this prediction are shown in table 7.1. As shown, the loading behavior is exceptionally well captured by the model; however, the unloading behavior is a large source of error. The predicted permanent deformation is approximately 0.45 compared to the experimental result of 0.16, and the slope of the stress strain curve during initial unloading is much more gradual than the unloading slope shown in the experimental results.

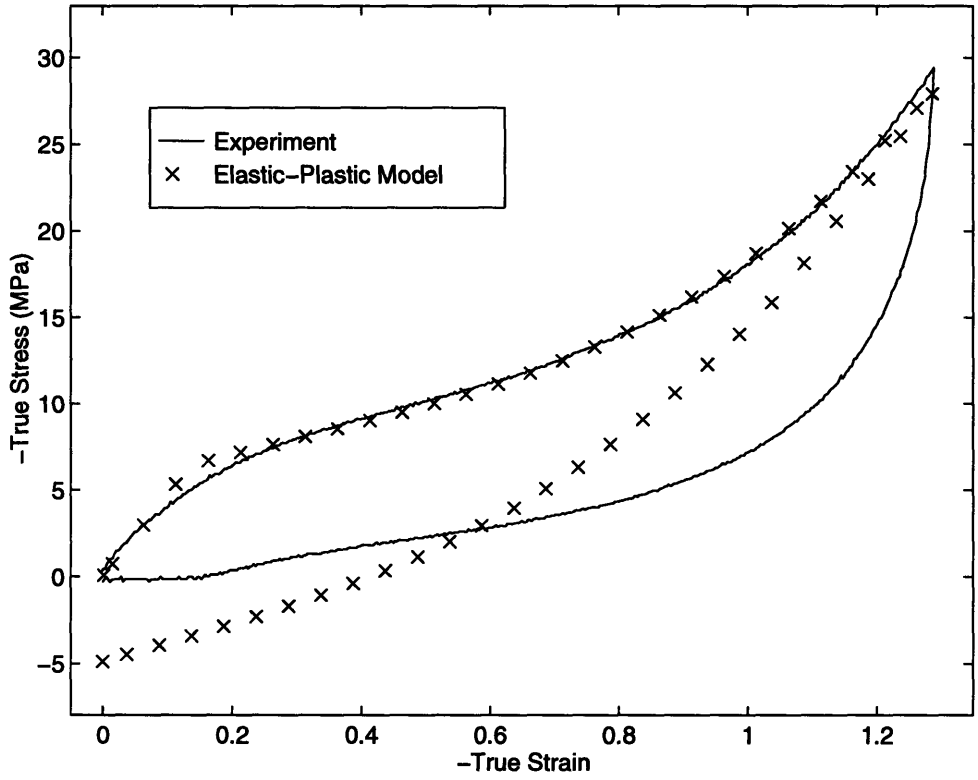

Figure 7.6: Elastic-plastic model prediction for the uniaxial compression behavior of unfilled polyurethane.

Figure 7.7 shows the plane strain compression results. Again, the loading behavior prediction is quite excellent, but the unloading behavior is still not well predicted. The observed permanent deformation is approximately 0.09, while the predicted permanent set is approximately 0.33.

In comparison to the rubber elastic models, the elastic-plastic model provides a number of advantages. First, because the initial stiffness and subsequent "yield" behavior is

considered in the model, it does a far superior job in modeling the loading behavior. Second, while the unloading response is not that accurate, the model provides some degree of hysteresis. Third, the model provides an excellent prediction of the material response in a different loading condition. Additionally, the effects of temperature and strain rate dependence are included in the model, though not considered at this time.

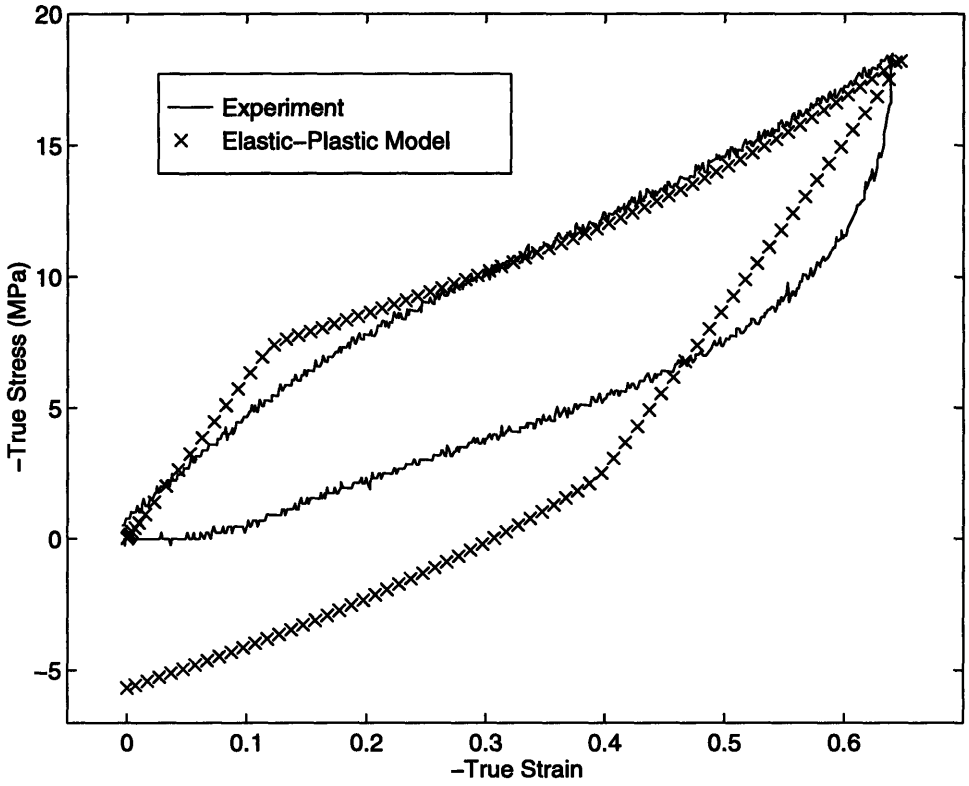

Figure 7.7: Elastic-plastic model prediction of the plane strain compression behavior of unfilled polyurethane.

It should also be noted that the elastic-visco plastic model was originally developed for glassy polymers. While the polyurethane under investigation certainly exhibits behavior similar to that of glassy polymers, its glass transition temperature is -16° C. Thus, because the material is actually in the rubbery domain, some of the actual values used as parameters of the model have lost their original physical significance. Of particular concern is the value of $\dot{\gamma}_o$. Typical values for glassy polymers are 10^{10} to 10^{13} s^{-1}, approximately 8 orders of magnitude larger than the value used in the previous predictions.

7.4 Comparison of Dual Network Model with Matrix Material Experimental Results

7.4.1 Dual Network Model

The model under consideration here decomposes the mechanical behavior of the material into two distinct parts: an equilibrium network and a time dependent network [40]. The equilibrium network is time independent and is meant to capture the state of the material after a long period of stress relaxation has occurred. The second network is meant to capture the rate dependent deviation from this equilibrium state.

A one dimensional representation of this model is shown in figure 7.8. The model consists of a parallel structure between the A and B networks. The A network is the equilibrium network and is modeled with a single spring element. The B network is the time dependent network, and it consists of a spring element in series with a dashpot.

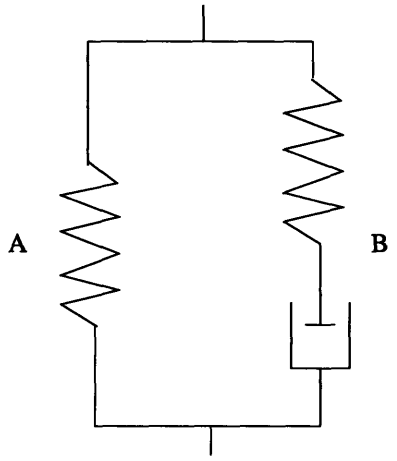

Figure 7.8: One dimensional representation of the three components of the dual network model.

Both spring elements were modeled using the Arruda-Boyce 8 Chain model, as discussed previously. The dashpot element is modeled by assuming that the reptation motion of macromolecules is responsible for the time dependent behavior of the material. Using equations which govern the reptational motion of chain molecules, the following effective creep rate expression can be written to define the dashpot element:

$$\dot{\gamma}_B = C_1[\lambda_{chain}^{Bp} - 1]^{C_2}\left(\frac{\tau_B}{\hat{\tau}_B}\right)^m \tag{7.14}$$

where $\dot{\gamma}_B$ is the effective creep rate; λ_{chain}^{Bp} is the chain stretch defined as $\sqrt{\frac{I_1^{Bp}}{3}}$; τ_B is the effective shear stress; and $\hat{\tau}_B$ is a material constant. Thus, three material parameters are needed in this model: $\frac{C_1}{\hat{\tau}_B^m}$, m, and C_2. The first two are positive values, whereas C_2 is restricted to be between 0 and -1, as restricted by reptational dynamics.

As was the case with the elastic-visco plastic model, a three dimensional finite strain continuum mechanics development is needed to formulate the full constitutive model from the one dimensional representation shown in figure 7.8. The model can then be coded as a user defined material for use with the ABAQUS finite element package.

7.4.2 Determining Model Parameters

In total, there are 9 model parameters needed to fully define the dual network model: CR, N, and the bulk modulus for each spring element; and the three dashpot parameters, $\frac{C_1}{\hat{\tau}_B^m}$, m, and C_2. In general, two uniaxial compression tests at different strain rates are all that is required to obtain the model parameters.

CR and N for the equilibrium network can be estimated by approximating the equilibrium response as a curve lying between the loading and unloading curves of the experimental data. The process for determining CR and N is the same as described before. CR for the B spring element can be estimated by corresponding its value to the tangent modulus of the stress strain curve during initial unloading, and N for the B network can be approximated as being equal to N of the A network. If the material in question is nearly incompressible, the bulk modulus can simply be taken to be a suitable value, 100 MPa for example. The effect of the three dashpot parameters are coupled together, so it is probably easiest to make a good initial guess of these values and then adjust them through trial and error. Bergstrom suggests the following values for a common elastomer: $\frac{C_1}{\hat{\tau}_B^m}$=1, C_2=-1;

and m=4. A more thorough discussion of how to obtain the model parameters can be found in reference #.

7.4.3 Discussion of Model Predictions

Figures 7.9 shows the dual network model predictions for the unfilled polyurethane in both uniaxial and plane strain compression. The material parameters used are shown in table 7.2 below.

Model Parameter	Value
CR_A	1.25 MPa
N_A	4.2
CR_B	10 MPa
N_B	9
$C_1/\hat{\tau}_B^m$	1e-4 $s^{-1}MPa^{-m}$
C_2	-0.9
m	2.4

Table 7.2: Model parameters used in the dual network model.

As shown, the dual network model captures the overall mechanical behavior of the material exceptionally well in both loading conditions. In uniaxial compression, the model underpredicts the initial stiffness of the material, and so the subsequent modulus reduction is not captured either. However, from a strain of approximately -0.6 on, the loading behavior is extremely well captured. The strength of the model is clearly seen in its ability to capture the hysteresis for the material. The unloading curve for the uniaxial compression data is also extremely well predicted. The permanent deformation as well as the slope of the stress strain curve during initial unloading are well predicted.

The plane strain compression results are also quite good. Again, the initial stiffness during loading is underpredicted, and the modulus reduction is not exhibited. The initial

slope of the unloading curve is well predicted also; however, the permanent deformation and overall amount of hysteresis are over-predicted.

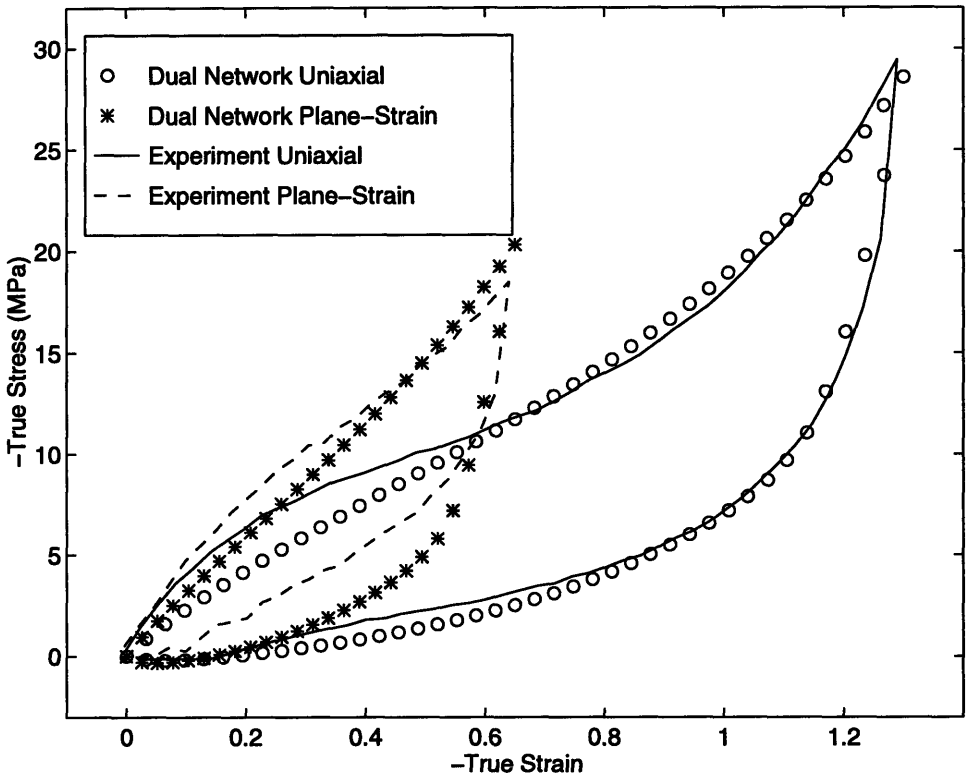

Figure 7.9: Dual network model predictions of the uniaxial and plane strain compression behavior of unfilled polyurethane.

It should be noted that the original intent of this constitutive model was to model the time dependent behavior of elastomers. The application of this model to the experimental data presented does not fully utilize the scope of the model since all of the experiments were basically tested at one strain rate. Thus, the dashpot model parameters used in the dual network model prediction of the behavior of unfilled polyurethane were determined solely for one strain rate.

Chapter 8

Unit Cell Model

Having proposed constitutive models for both the base material and the fiber, a unit cell finite element model was assembled in order to investigate the effect of fiber fillers. The glass fiber was modeled explicitly, and the polyurethane, along with any other fillers used by the manufacturer, was modeled as the base material.

Two sets of results were acquired from these simulations by using two different material models. The first set of results used the Arruda-Boyce 8 Chain model because of its computational simplicity, and the second set were performed with the elastic-visco plastic model because of its ability to accurately predict the loading behavior of the base material. The eight chain simulations provided a more qualitative understanding of fiber filler effects and explored the issue of the initial angular orientation of the fiber as well as multiple fiber interactions. The modified elastic-visco plastic simulations attempted to quantitatively predict the plane strain experimental results at two different volume fractions of fiber filler. With confidence that the model could accurately predict the macroscopic stress-strain behavior of the material, stress distributions within the unit cell were then examined in hopes of drawing connections with wear and fatigue models.

8.1 Model Description

A simple unit cell finite element model as shown in figure 8.1 was used to explore the effect of fiber content in rubbers. The finite element package used was ABAQUS. The model was constructed with two-dimensional plane strain linear hybrid elements (CPE3H and CPE4H), so that in essence, a block of polyurethane with a "sheet" of glass fiber was modeled. A two dimensional representation was selected because of its computational efficiency. The model is still appropriate, however, as a first order approximation and can

still be compared usefully with experimental plane strain data. Additionally, the two dimensional representation reduces the fiber's initial angular orientation to just one angle, as opposed to two for the three dimensional case.

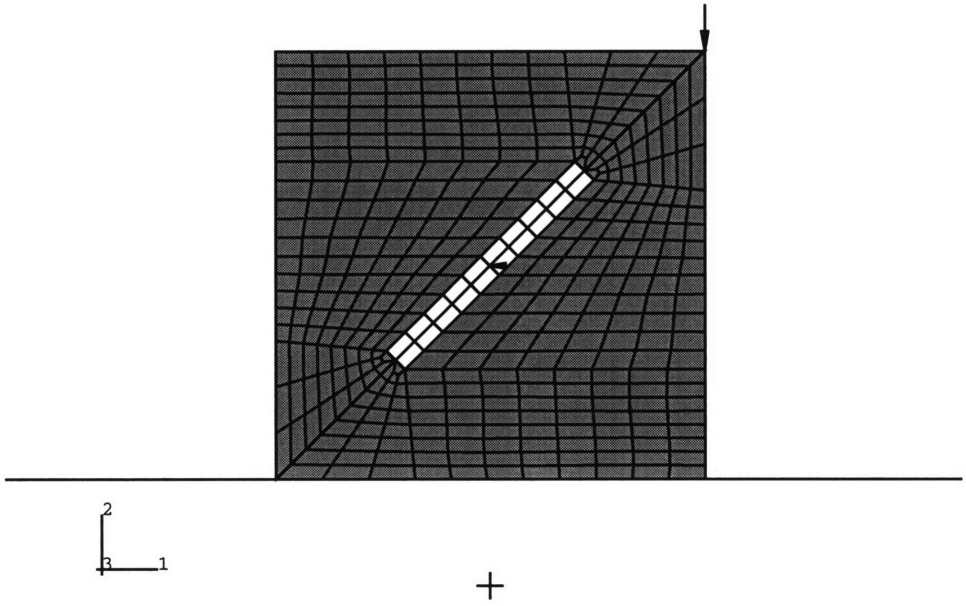

Figure 8.1: ABAQUS finite element model of a fiber filled rubber using 2D plane strain hybrid elements.

Because the model was to simulate plane strain compression, a displacement boundary condition was applied to the upper row of nodes. A surface was defined by the bottom edge of the block of material, and a rigid surface was defined, so that the block could deform against it. The rigid surface provided a measure of the reaction force during the course of deformation, and by assuming incompressibility, a true stress-true strain curve could then be assembled as follows:

$$\varepsilon = \ln\lambda = \ln\left(\frac{u}{l_o} + 1\right) \tag{8.1}$$

$$\sigma = \frac{F}{A_o}\lambda = \frac{F}{A_o}\left(\frac{u}{l_o} + 1\right) \tag{8.2}$$

where u is the displacement of the upper row of nodes; l_o is the original height of cell; A_o is the original cross-sectional area; and F is the reaction force at the rigid surface. Addi-

tionally, the sides of the unit cell were constrained to deform uniformly in order to model the mesh as a repeated unit cell.

The fiber is centered within the block of material. The aspect ratio (length to diameter) of the fiber was 10 to 1. For many of the simulations, the fiber was placed at a 45 degree angle as shown; however, the initial angular orientation was altered in one set of simulations to specifically explore the influence of fiber orientation. The matrix material and fiber share common nodes. Thus, the mesh models the interface as if the fiber were perfectly bonded with the polyurethane.

8.2 Unit Cell Model with Arruda Boyce 8 Chain Material Model

The Arruda-Boyce 8 Chain model was used initially to model the base material behavior in the unit cell finite element model. The parameters used in the model were the same as those described in the material modeling section of chapter 7.

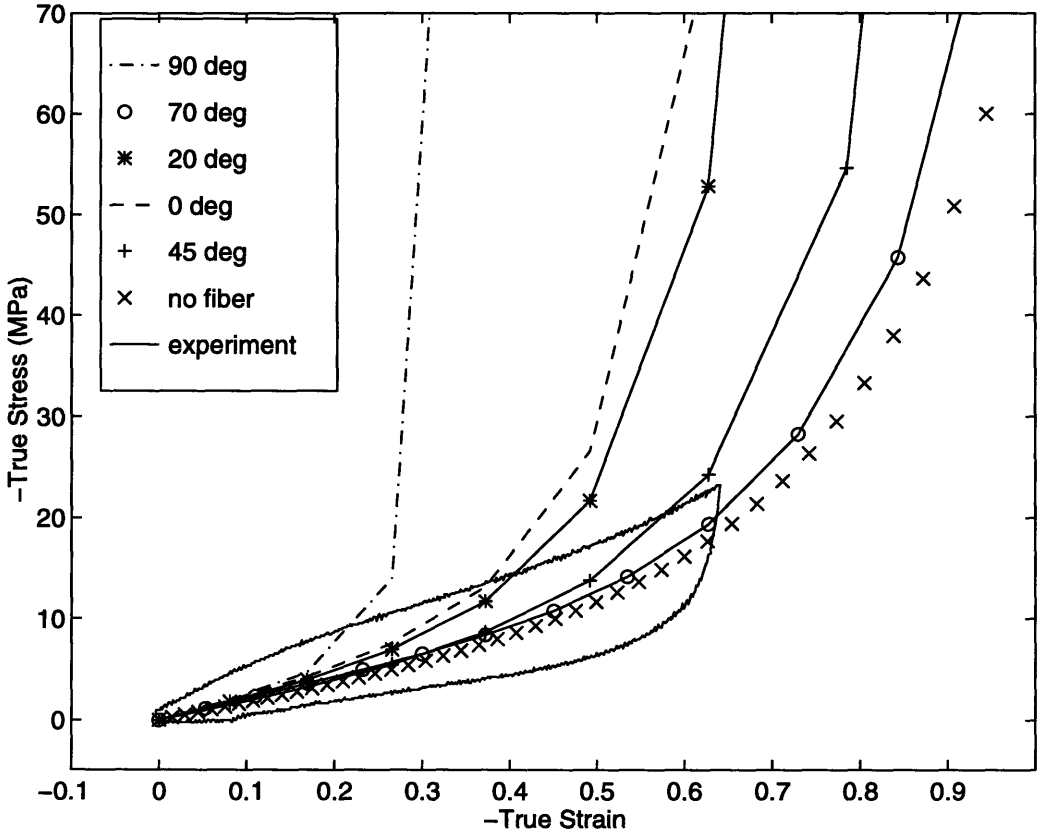

Figure 8.2: Unit cell stress-strain predictions for various initial fiber angular orientations.

An initial result from the model showed the correct qualitative trend of fiber content behavior for a 4% filled model. These results are shown in figure 8.2 with the "+" symbol representing an initial orientation at 45 degrees, and the "x" symbol representing the unfilled material. Initially, the addition of the fiber adds very little to the response of the material. However, at higher strains of roughly -0.7 and above, the effect of the fiber is seen in stronger hardening behavior. This trend is quite similar to the experimental results for plane strain compression.

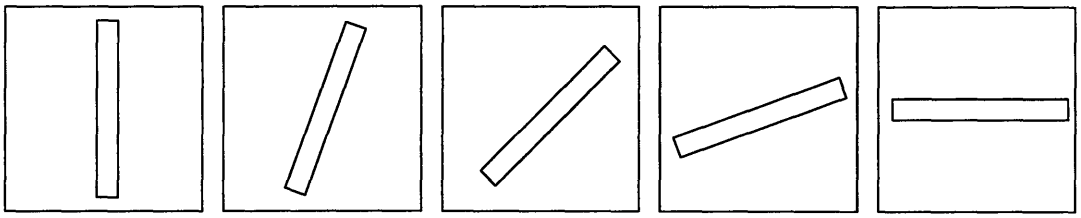

Figure 8.3: Different initial angular orientations of the fiber.

8.2.1 Effect of Initial Angular Orientation of Fiber

The model was then used to explore the effect of initial angular orientations as shown in the various meshes depicted in figure 8.3. Because the fiber is assumed to be randomly dispersed throughout the rubber matrix, looking at different initial angular orientations was of particular importance if a constitutive model was to later be assembled.

We first note qualitative observations from these simulations. Sample deformed meshes are shown in figures 8.4, 8.5, and 8.6. In the 0 and 90 degree orientations, the mesh geometry is perfectly symmetric, and the fiber does not rotate during deformation. Alternately, the 20, 45,and 70 degree orientations add asymmetry to the model, and the fiber

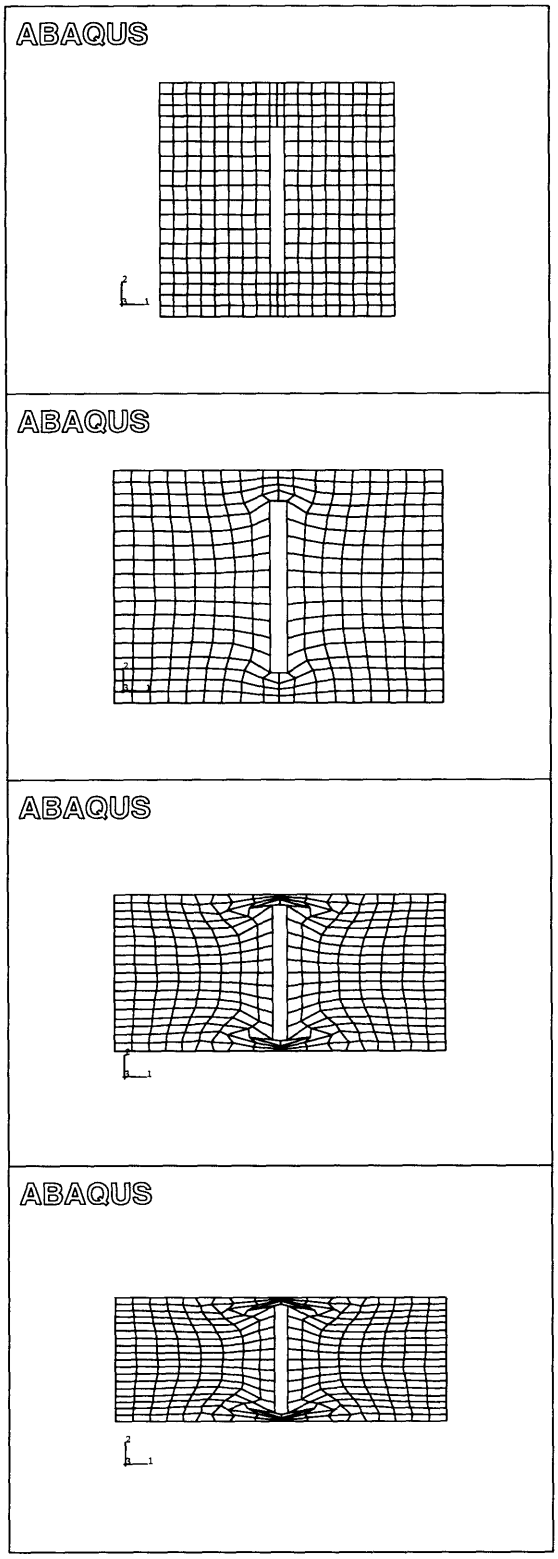

Figure 8.4: Deformed mesh of the fiber oriented at 90degrees from horizontal.

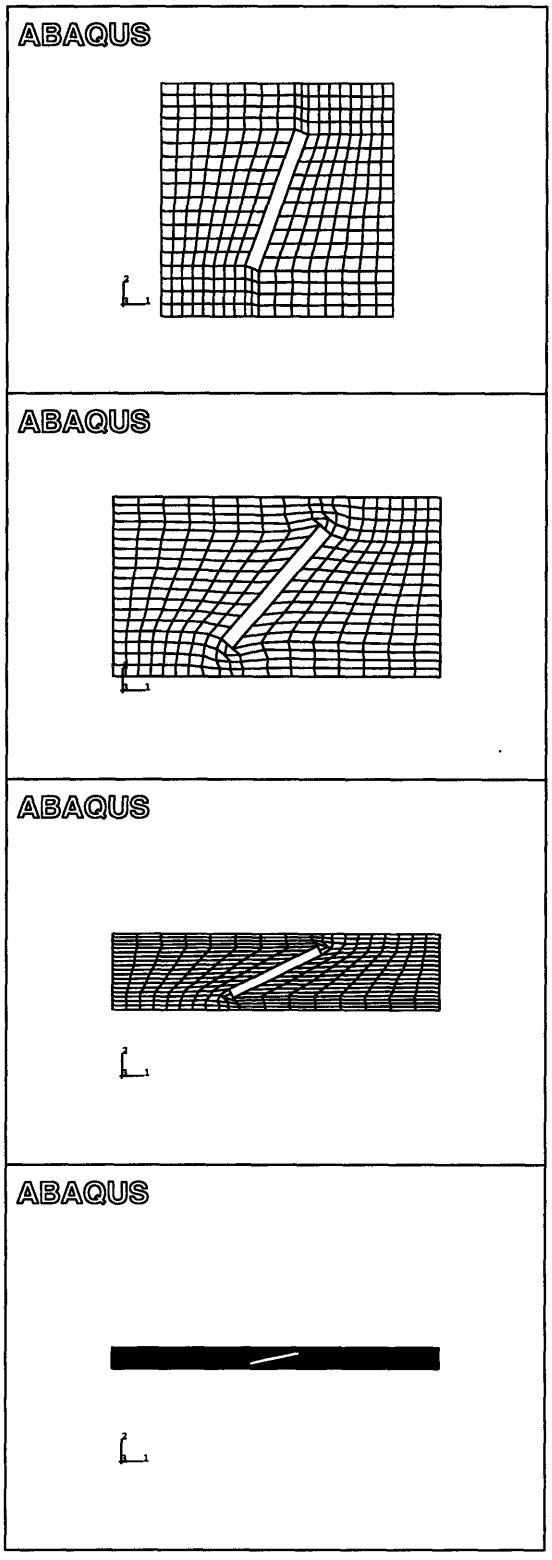

Figure 8.5: Deformed mesh of the fiber oriented at 70 degrees from horizontal.

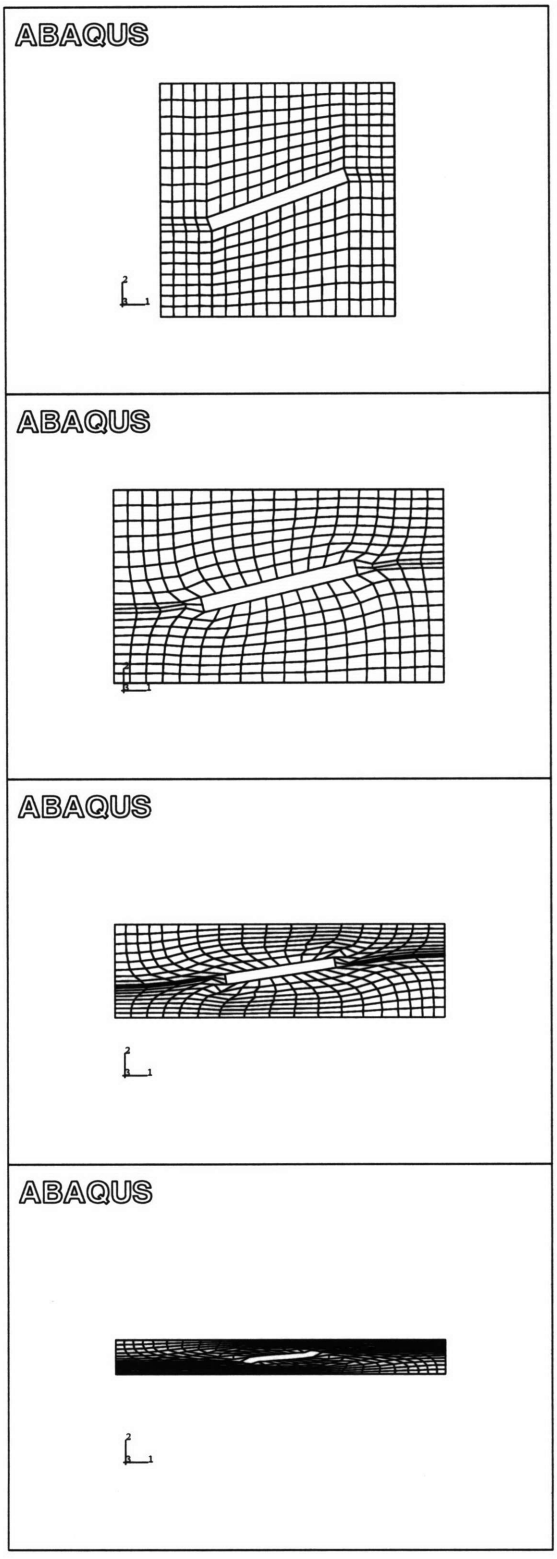

Figure 8.6: Deformed mesh for fiber oriented at 20 degrees from horizontal.

is able to rotate until it reaches a final orientation that is nearly horizontal. In a sense, after reaching this final position, the fiber "locks" and ceases any further rotation within the unit cell. Figure 8.7 plots the angular orientation of the fiber during deformation.

Alternately, figure 8.8 plots the length of the fiber at each step of the deformation. The 0 and 90 degree orientations do not permit the fiber to rotate and are considered here first. The 90 degree fiber orientation is perfectly vertical. In the early stages of deformation, only rubber deforms until the fiber is reached. Once the fiber is reached, the fiber undergoes uniaxial compression, and the fiber shortens as shown by the figure. The 0 degree fiber orientation is perfectly horizontal. This orientation offers less stiffness in the unit cell's deformation direction. In a sense, this fiber experiences uniaxial tension because the fiber is modeled as being perfectly bonded into the rubber. Thus, as the sides of the unit cell displace outward, the fiber is pulled in the same direction.

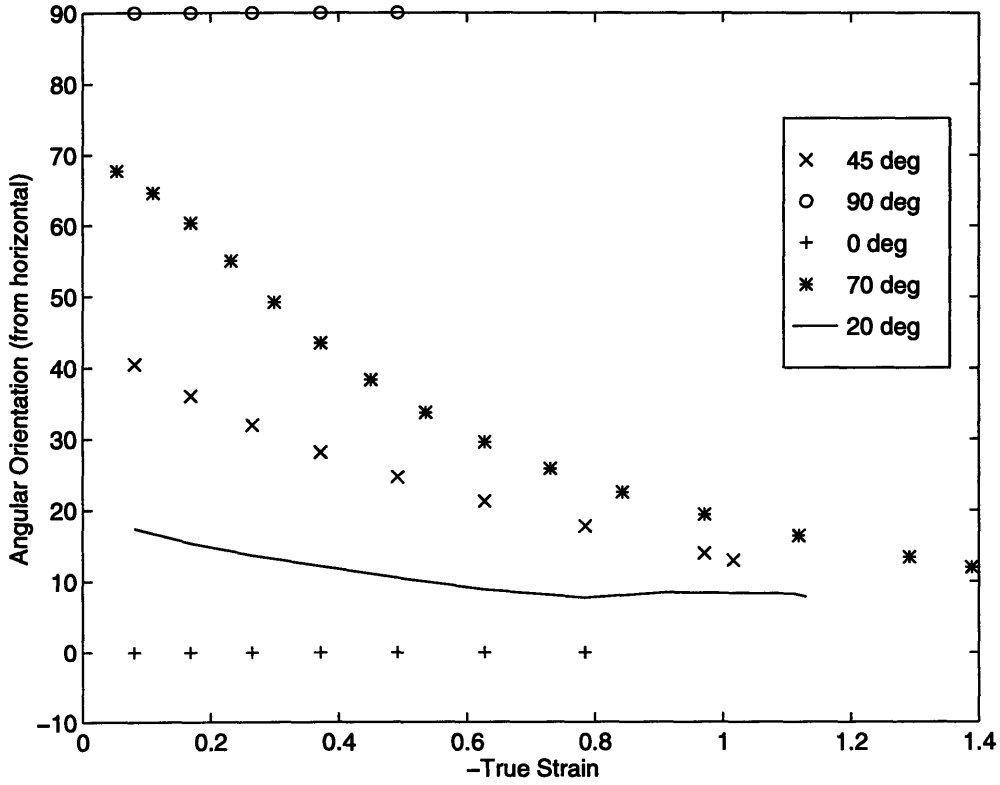

Figure 8.7: Angular orientation of fibers during deformation.

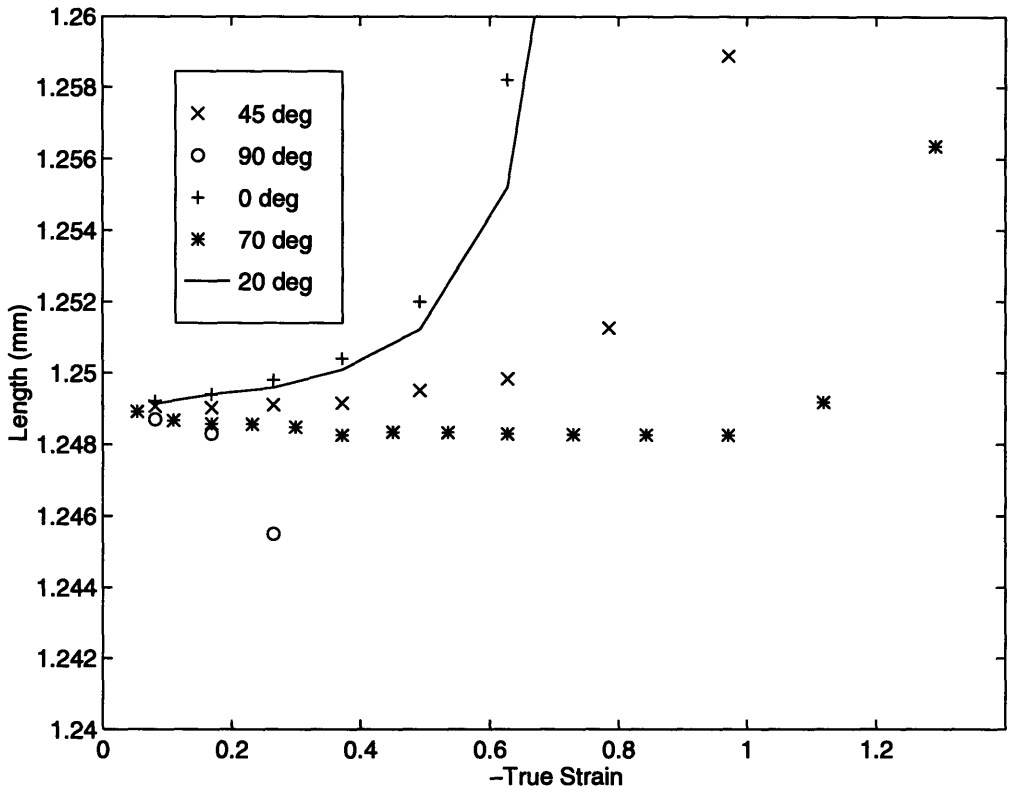

Figure 8.8: Fiber length during deformation.

For the 20, 45, and 70 degree fibers, the fiber basically remains the same length until reaching a certain point at which straining begins. By comparing figures 8.7 and 8.8, it is observed that the point of fiber straining occurs when fiber rotation has slowed. Thus, after the fiber has rotated and "locked" into a near horizontal position (15 to 25 degrees), it begins to extend. Again, the fiber lengthens because of the perfect bond assumption.

Understanding the kinematics of the fiber provides sound reasoning for the data shown in figure 8.2. In this figure, true stress is plotted versus true strain. Immediately, the effect of fiber "locking" and subsequent straining of the fiber can be recognized. The 0 and 90 degree orientations are perfectly symmetric and therefore do not rotate. Thus, they immediately contribute significant stiffening to the mechanical response of the material. On the other hand, the three other orientations can rotate. We note from figure 8.7 that the 70 degree orientation allows the fiber to rotate the most. Thus, its stiffening contribution is

not realized until a strain of approximately -0.65 is reached. Even at this point, the amount of stiffening is not very large. On the other hand, the 20 degree orientation is unable to rotate a significant amount. Thus, its stiffening contribution is felt as early as a strain of -0.2. Appropriately, the 45 degree orientation lies between the other two cases.

A comparison with actual plane strain data shows that the material underpredicts the response of the material. This discrepancy can be immediately accounted for by realizing that the Arruda-Boyce 8 Chain model did an unsatisfactory job of modeling the actual behavior of the material in both uniaxial and plane strain compression.

8.2.2 Fiber Interactions

In the actual fiber filled rubber material, the fibers are randomly oriented. The current unit cell model only accounts for one of these orientations. Because each fiber orientation rotates and deforms differently, it is particularly interesting to examine the results of coupling fibers with different initial orientations together.

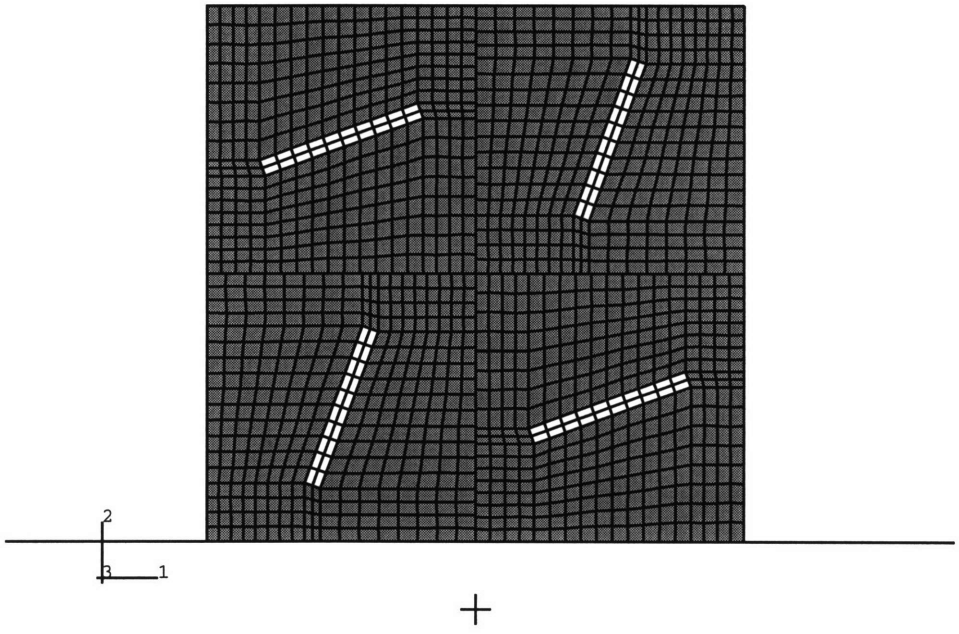

Figure 8.9: Four fiber unit cell model incorporating both 20 degree and 70 degree fibers.

Figure 8.9 shows such a model. Four fibers have been included together to form one larger unit cell. Multiple point constraints (MPC's) were used to essentially tie four

meshes together into one larger finite element mesh. The upper right and lower left fibers are 70 degrees from horizontal orientations, and the remaining fibers are 20 degree orientations. Figure 8.10 shows the deformed four fiber mesh at different stages of compression.

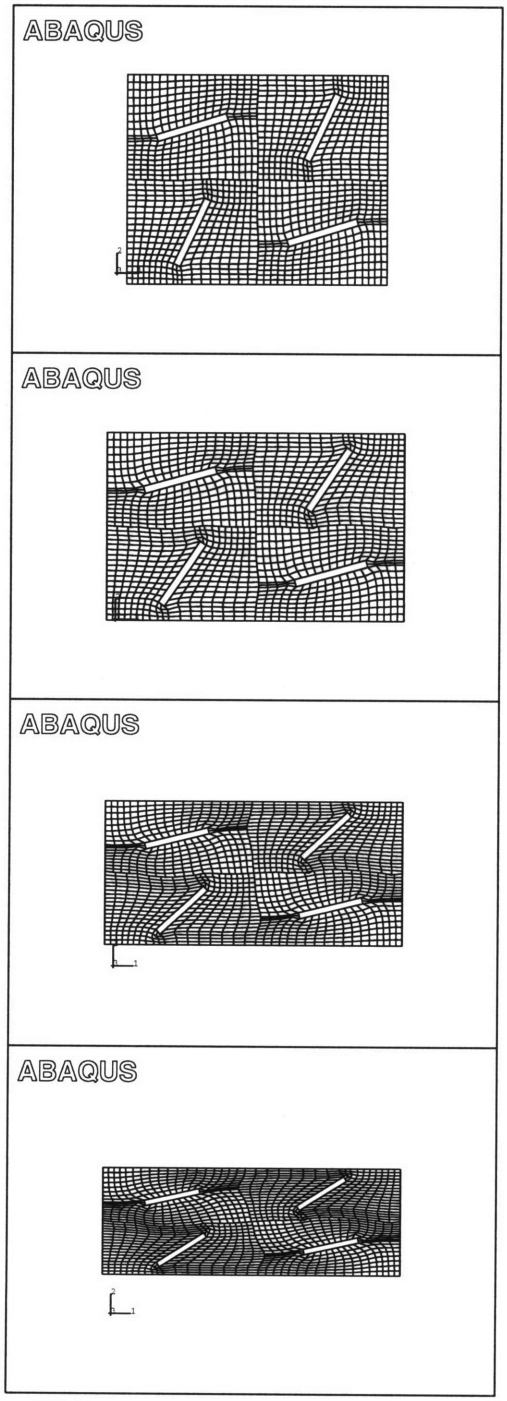

Figure 8.10: Deformed mesh of four fiber model at different stages of compression.

Figure 8.11 shows the stress-strain predictions provided by the model. It is plotted along with the results obtained from the 20 and 70 degree fiber orientation simulations. As one would expect, the response lies between the individual fiber orientation responses. However, the four fiber prediction is not an exact average of the other two. The prediction is weighted more towards the 70 degree orientation response.

Considering the unit cell model for a fiber initially oriented at 20 degrees from horizontal, it would be expected that this fiber orientation should dominate the response of the unit cell. Because the four fiber model yielded a less stiff response, it would also be expected that the 20 degree fiber rotated through a smaller angle and that the fiber was not strained as much in comparison to the single fiber model. Appropriately, as shown in figure 8.12, the 20 degree fiber rotated less and lengthened less in the four fiber model. It would seem then that the 20 degree fibers were not able to rotate as freely because of the presence of the 20 degree fibers. Alternately, the 70 degree fibers rotated through a larger angle and lengthened to a larger value.

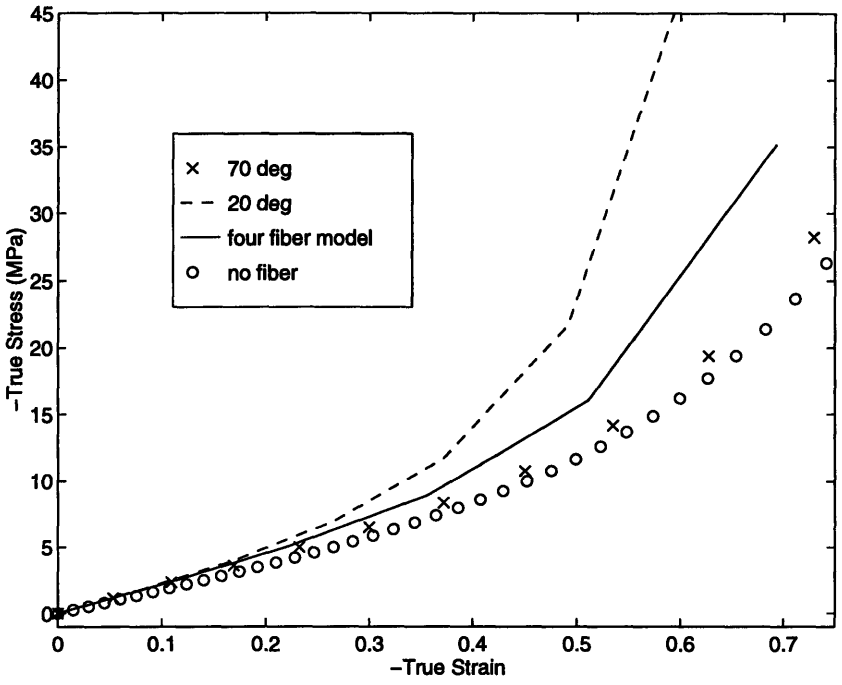

Figure 8.11: Stress-strain response of the four fiber unit cell model.

(a)

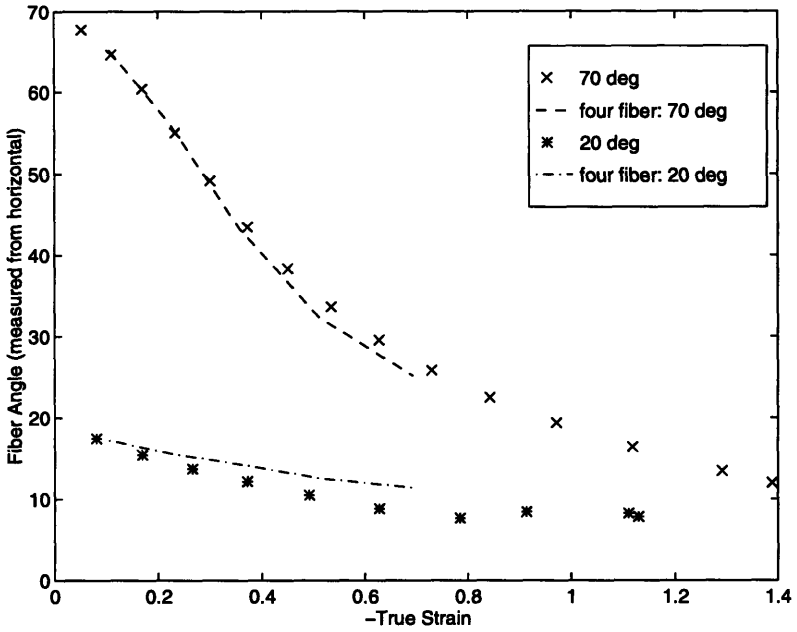

(b)

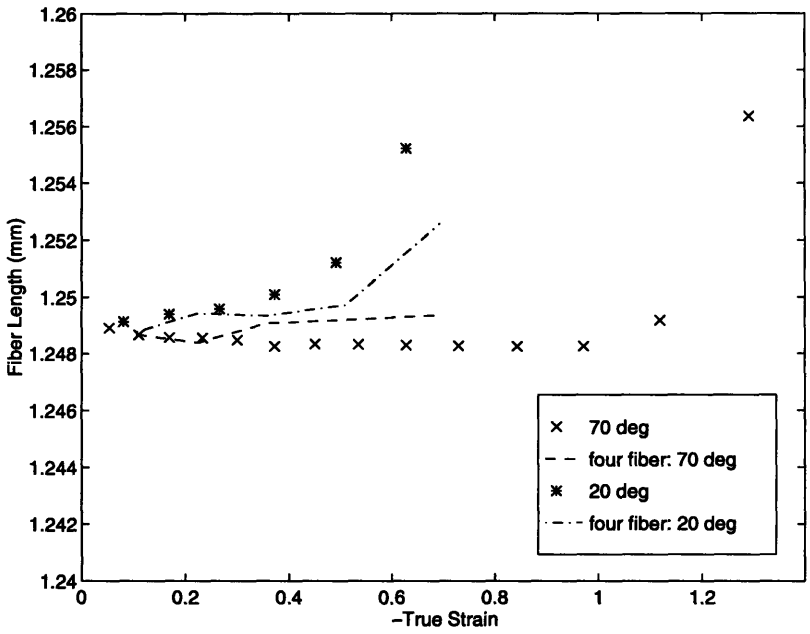

Figure 8.12: Angular orientation (a) and fiber length (b) of fibers during deformation.

8.2.3 Stress and Strain Distributions

Figures 8.13 and 8.14 show several stress and strain contours of the four fiber unit cell model as well as stress and strain contours of the individual fiber models for comparison. Because of the material model being used, a more quantitative discussion will be provided in section 8.3. Qualitatively, the presence of the fiber has certainly caused a large degree of

inhomogeneity in both the stress and strain distributions. In both the single and four fiber models, the fiber undergoes a very small amount of strain while the rubber matrix experiences some strain concentrations near the interface and at the ends of the fiber. Similarly, stress concentrations occur along the interface and at the ends of the fiber.

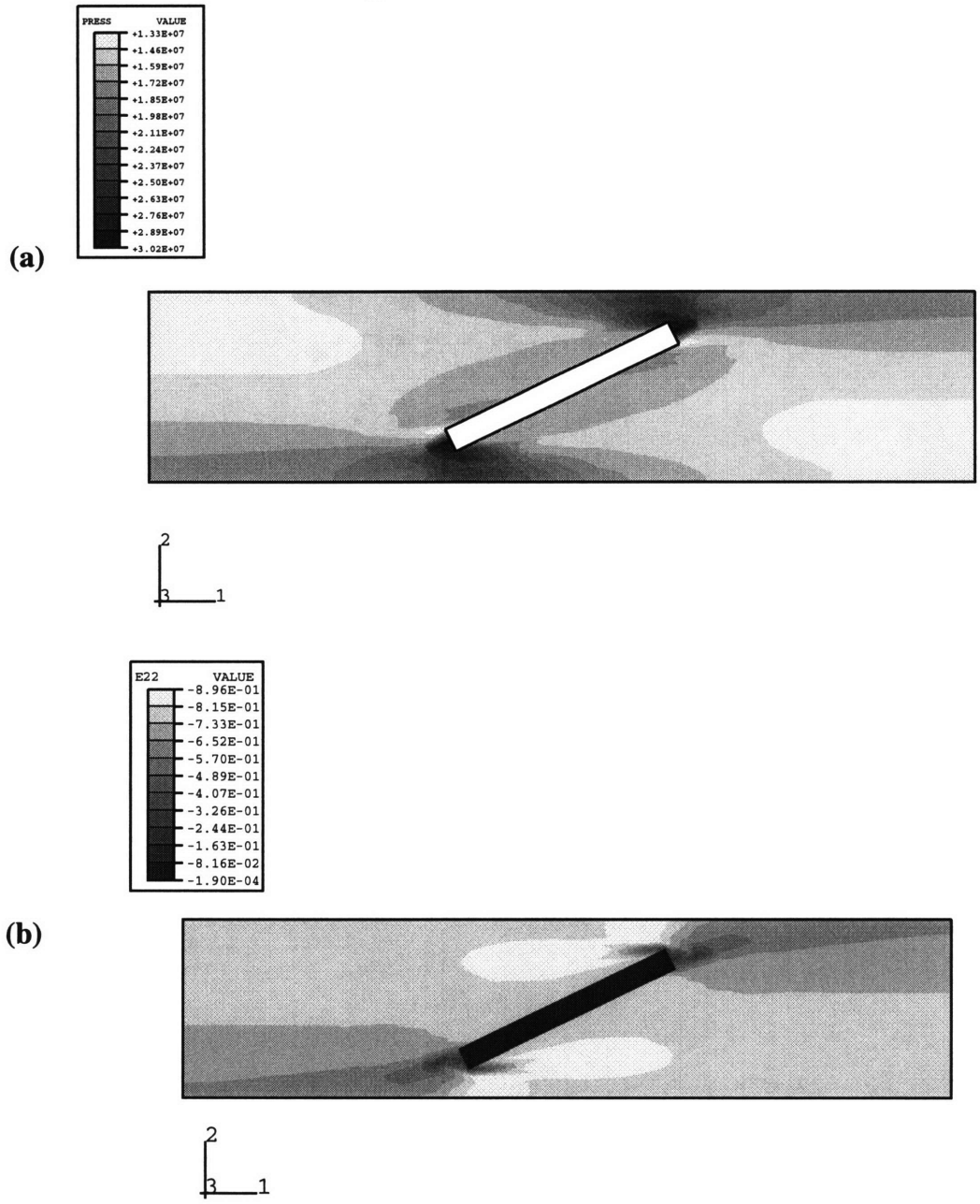

Figure 8.13: Pressure (a) and 2-direction strain (b) contours of the 70 degree single fiber unit cell model. The fiber is not plotted in (a).

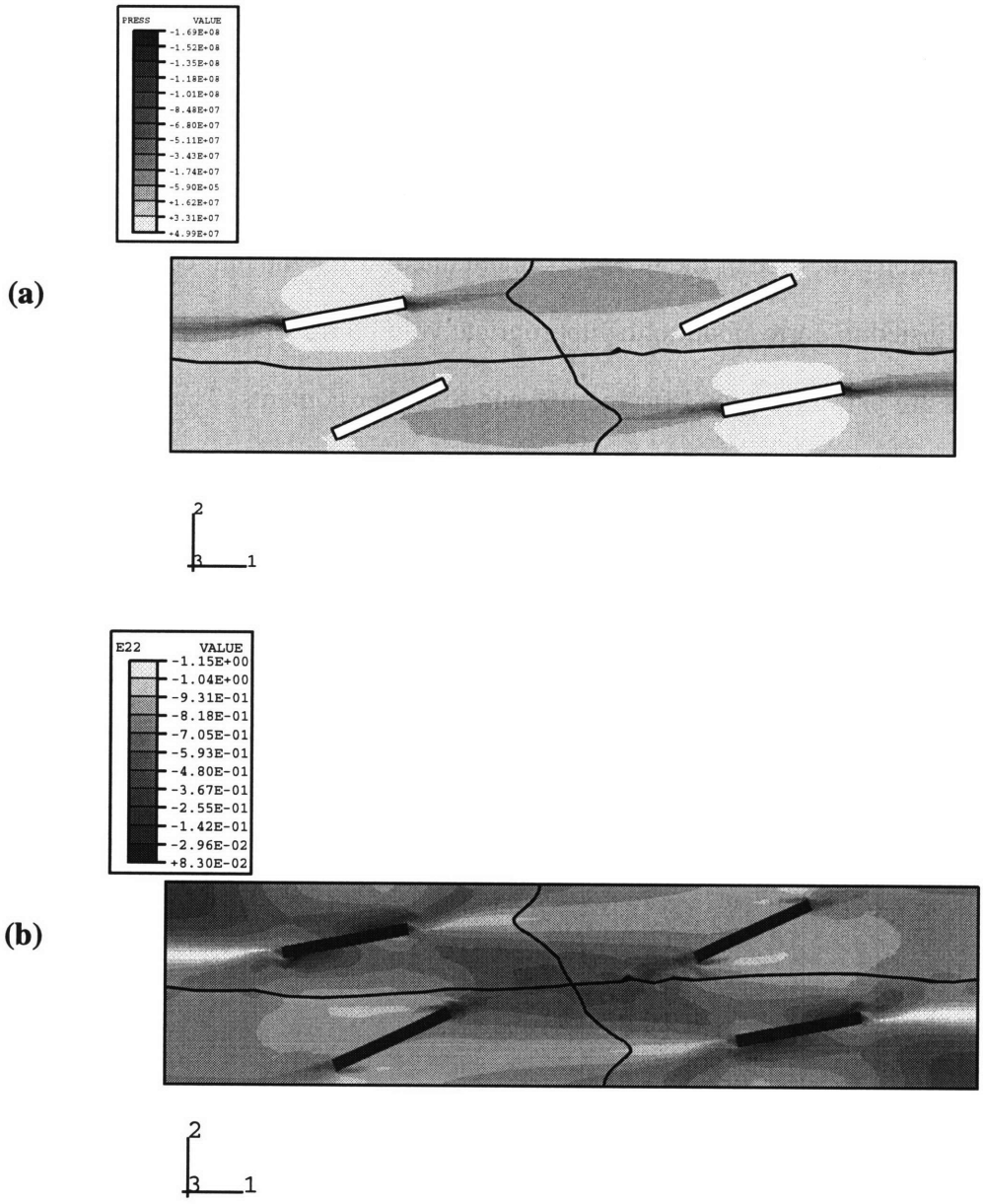

Figure 8.14: Pressure (a) and 2-direction strain (b) contours of the four fiber unit cell model. The fiber is not plotted in (a).

8.3 Unit Cell Model with the Elastic-Visco Plastic Model

For the second round of simulations, the elastic-visco plastic model was used. While the dual network model was able to capture the hysteresis behavior of the material, this model was chosen because it accurately captured the loading response of the unfilled poly-

urethane in both uniaxial and plane strain compression. Thus, the unloading behavior for the unit cell finite element model are not considered here.

Figure 8.15 shows the model predictions for the plane strain compression of polyurethane with three levels of fiber filler content: 0.0, 0.04, and 0.08 by volume fraction. For these simulations, the size of the fiber was maintained, while the unit cell of matrix material was adjusted to correspond to the appropriate volume fractions. As shown, the model predictions are extremely good for the 0% and 8% fiber contents. The single filled fiber content seems to be a bit underpredicted; however, the prediction is still quite adequate.

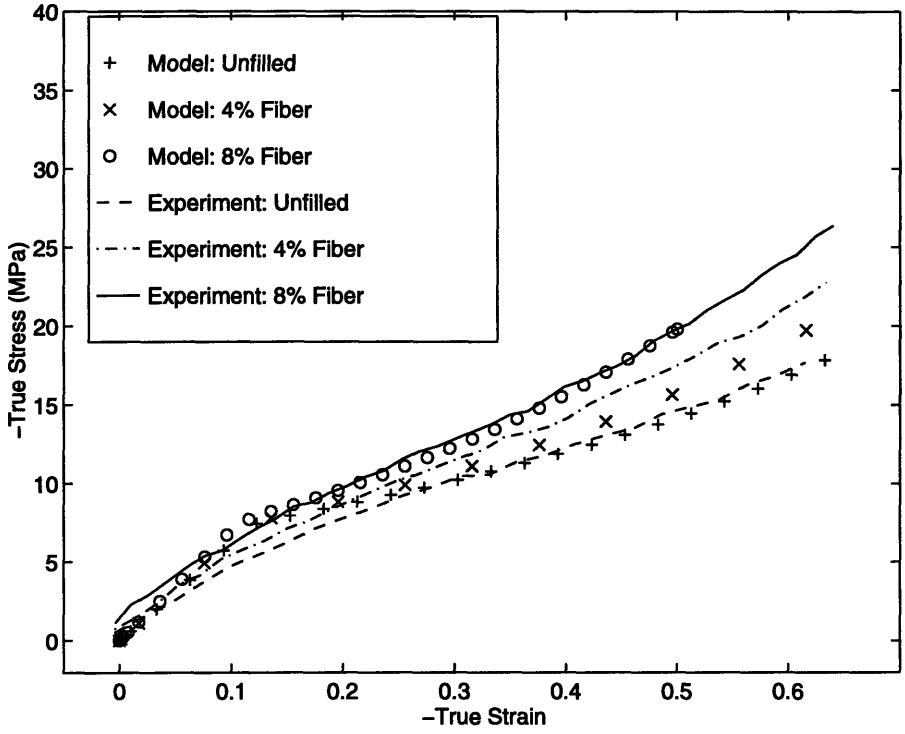

Figure 8.15: Unit cell model predictions for varying fiber contents using the elastic-visco plastic material model.

Figure 8.16 shows a pressure and mises stress contour for the single filled fiber unit cell model. The presence of the fiber caused inhomogeneity in these distributions. The pressure contour shows a gradient of large compressive pressures along the interface of the length of the fiber. These values ranged from approximately 13 MPa to 27.4 MPa. Furthermore, there were negative pressures as high as -18.7 MPa at the ends of the fiber. These

negative pressures represent the forces which lengthened the fiber as shown in figure 8.8. These same pressures would cause debonding as well. The mises contour shows a band of large values running along the diagonal of the unit cell and through the fiber. These values ranged from 13.9 MPa to 18.4 MPa.

Figure 8.17 shows the pressure and mises stress contour for the double filled fiber unit cell model. The shapes of the distributions were quite similar; however the magnitudes were larger for the double filled model. Pressure values along the interface ranged from 27 to 37 MPa, and the negative pressures at the ends of the fiber were as high as -29.3 MPa. Mises stresses along the diagonal of the unit cell ranged from 16 MPa to 28.2 MPa.

Figure 8.18 shows the 2-direction and shear strain contours for the single filled fiber unit cell model. As shown, the fiber experienced very little strain (-1.56e-4). Immediately surrounding the fiber, however, are regions of high strain ranging from -0.546 to -0.71. The shear strain contour shows large tensile and compressive shear strains along the interface of the fiber at each end. Maximum tensile shear strains were 0.425, while maximum compressive shear strains were -0.262.

Figure 8.19 shows similar contours for the double filled fiber. Again, these distributions are very similar in shape to those of the single filled fiber, but the magnitudes are higher. 2-direction strains surrounding the fiber ranged from -0.634 to -0.825. Maximum tensile shear strains were 0.937, and maximum compressive shear strains were -0.242.

Because the unit cell model was shown to properly predict the stress-strain behavior of fiber filled rubbers, the strain and stress distributions within the unit cell can provide valuable information in regards to developing wear or fatigue models. For example, models for fatigue and crack propagation mostly center on determining the stress concentration at the points of interest. The contours shown above clearly demonstrate a capability in determine-

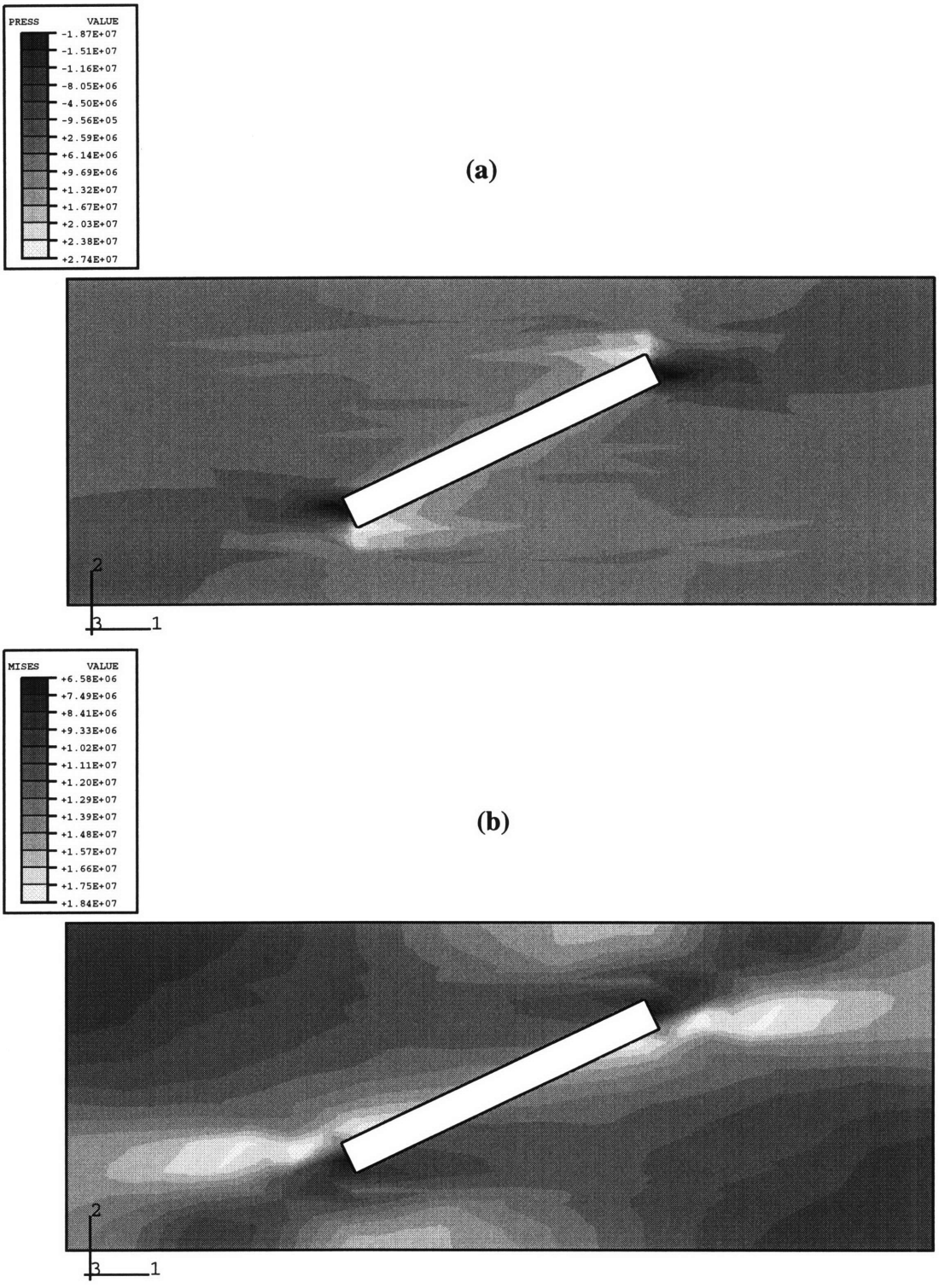

Figure 8.16: Pressure (a) and mises (b) contour for single filled fiber unit cell. The fiber is not plotted in this figure.

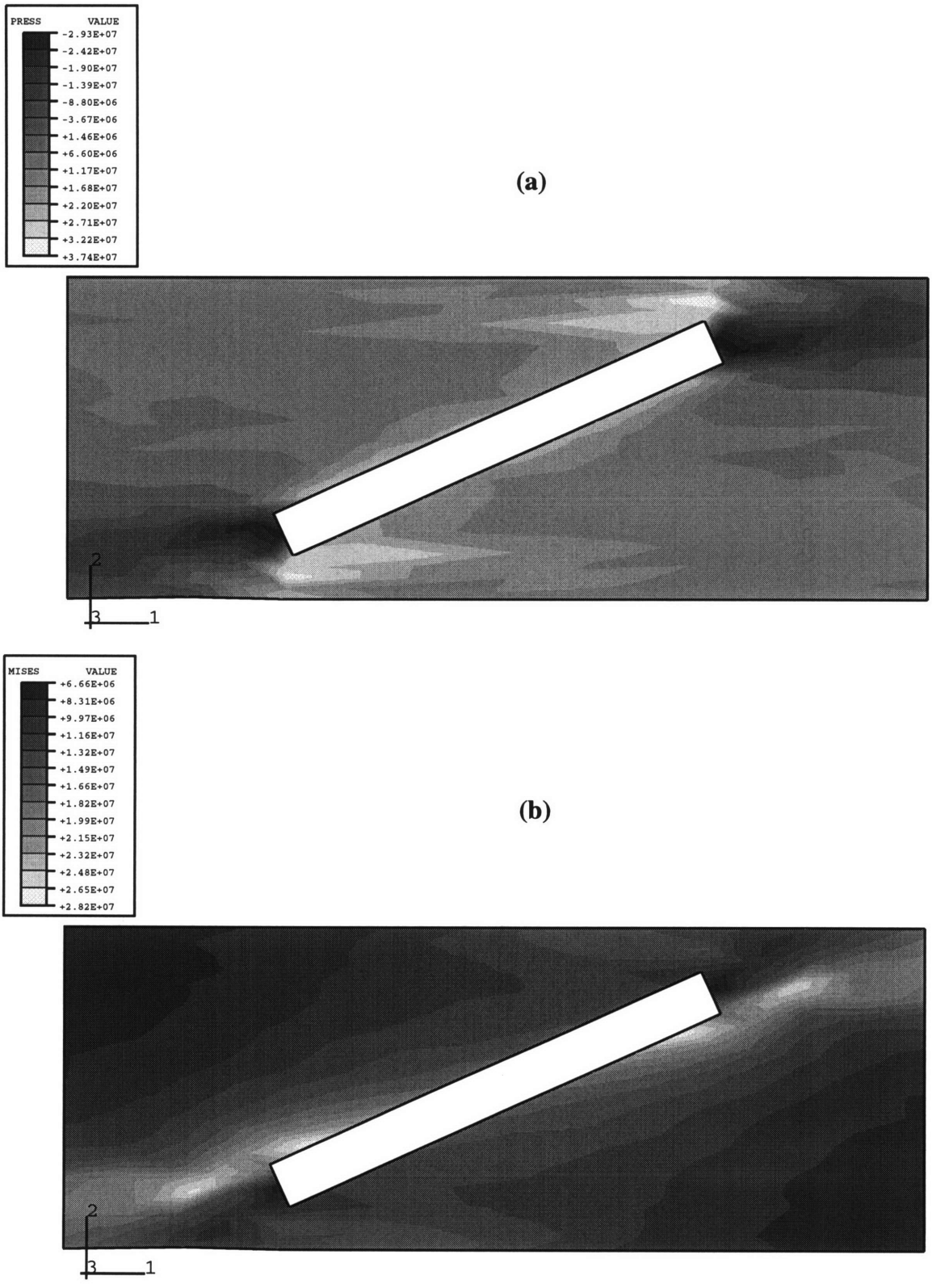

Figure 8.17: Pressure (a) and mises stress (b) contours for the double filled fiber unit cell model. The fiber is not plotted in this figure.

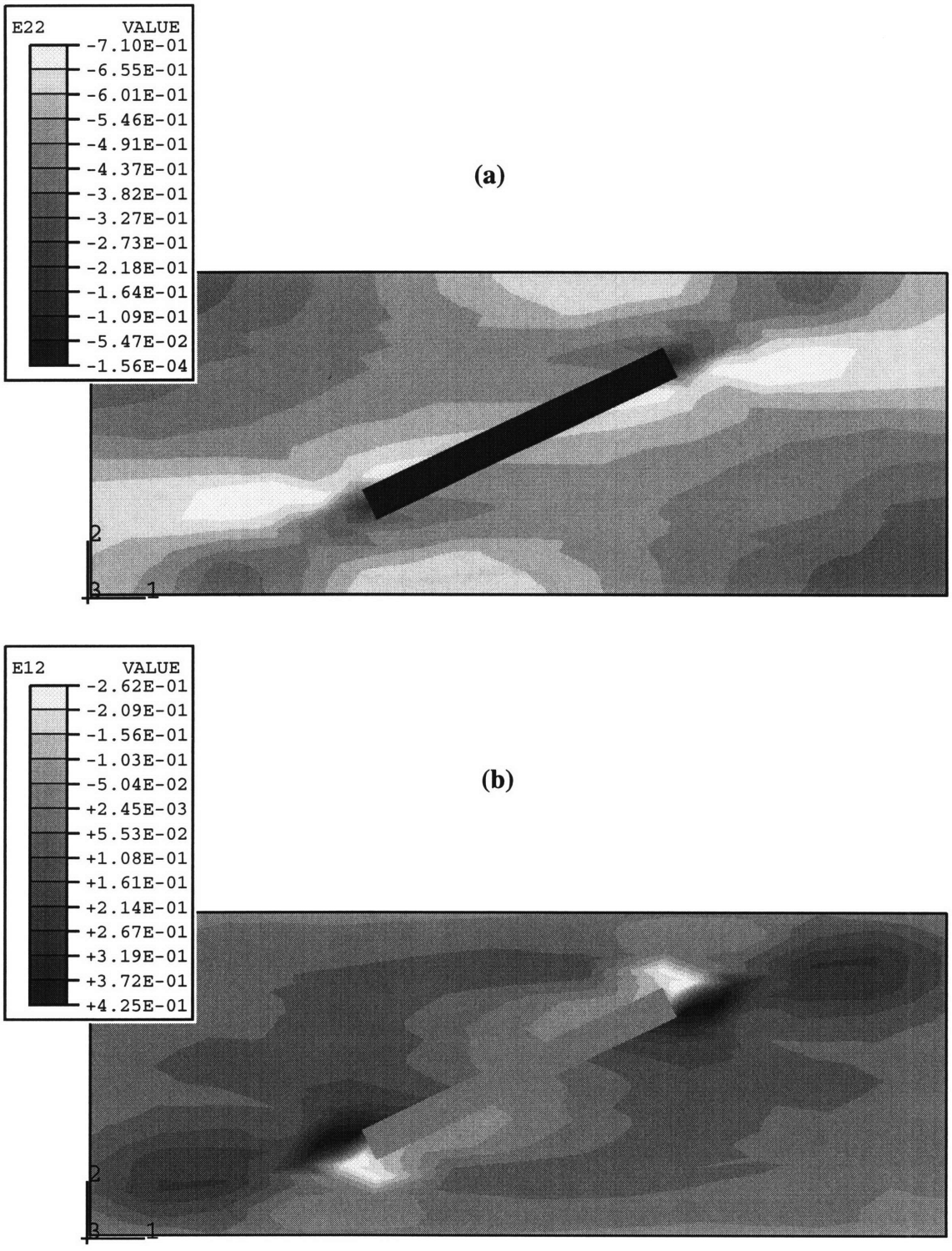

Figure 8.18: 2-direction (a) and shear strain (b) contours for the single filled fiber unit cell model.

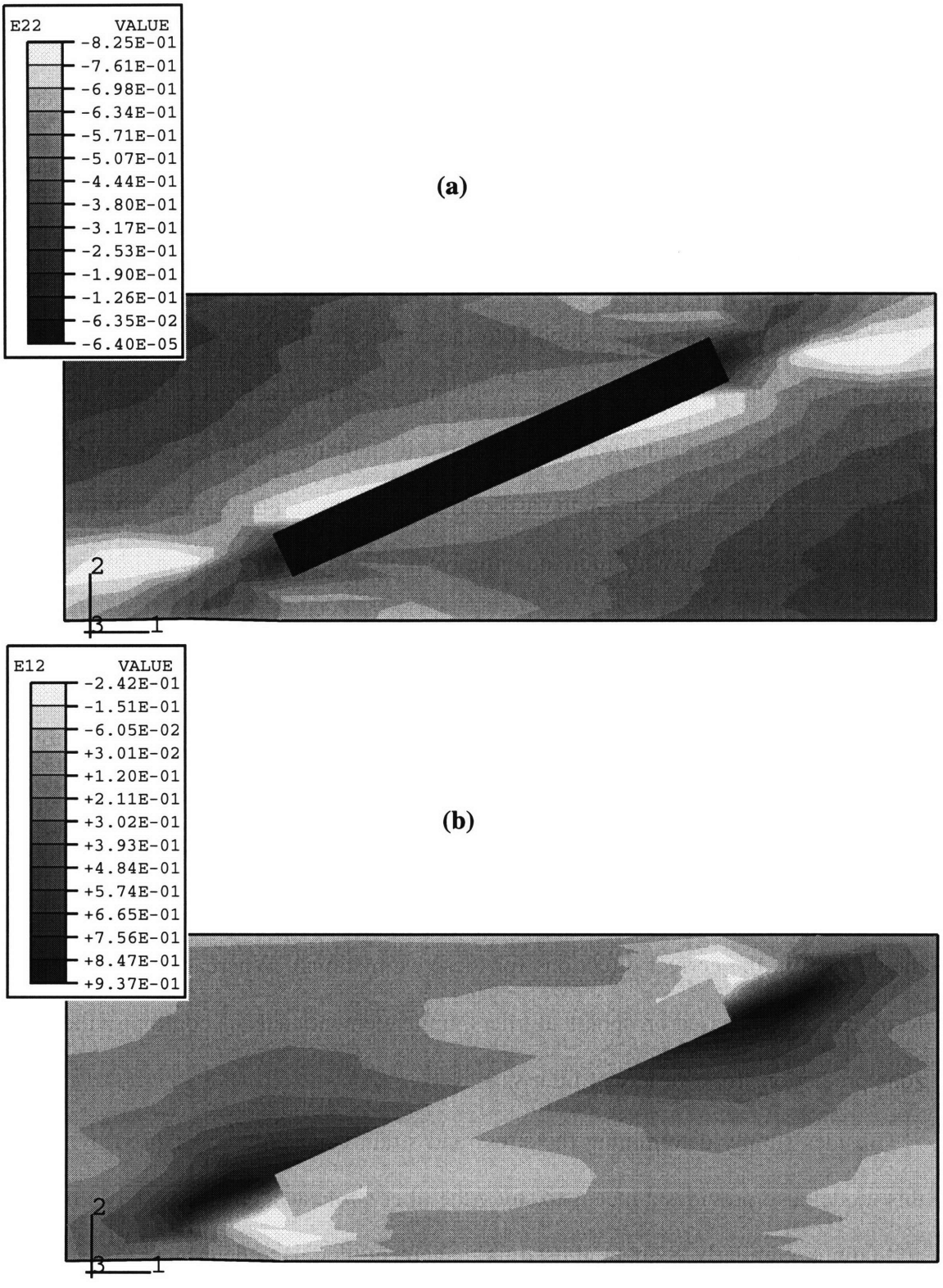

Figure 8.19: 2-direction and shear strain contours for the double filled fiber unit cell model.

ing that type of information. For example, the pressure contours in figure 8.16 and 8.17 display regions of negative pressure at each end of the fiber. These tensile stresses would indicate a mechanism for crack initiation and propagation.

The usefulness of the stress and strain distributions can also be viewed in relation to previously proposed models. As discussed in section 5.1.2, Kwon suggested a qualitative model in which the fatigue life is related to the ratio of the shear stress at the fiber-rubber interface and the tensile stress applied to the composite. Kwon's simplifying expression predicted that this ratio should increase with larger volume fractions of fiber. The unit cell model confirmed this prediction and can also be used to investigate the other effects which Kwon speaks of such as varying the aspect ratio of the fiber. Furthermore, the use of finite element analysis can provide more quantitative predictions of the ratio in different loading conditions and for various fiber orientations.

In regards to Yang's wear model, the unit cell model could also provide useful information. Yang's model is based on a damage volume which is calculated by determining the volume of material experiencing a triaxial tension greater than a certain value. Stress contours of the unit cell model could basically provide this information graphically. (The use of interface elements or local element coordinate systems would facilitate resolving the stresses in the correct directions for these estimations). Whereas Yang wrote closed form expressions based on spherical fillers, finite element analysis could provide damage zone predictions for a variety of filler shapes.

Besides simply determining the stress and strain concentrations caused by the fiber, this model also provides a means to study the fiber's role as a crack arrester in both wear and fatigue. Similarly, Siah, et al used finite element models to determine that steel fibers improve the fracture toughness of cement by controlling crack growth [37].

In summary, the unit cell model has been shown to provide information that can be valuable in developing a model for the wear or fatigue of fiber filled rubbers.This unit cell model could be applied to experimental data already in the literature in order to further explore these issues. Otherwise, wear data pertaining to polyurethane filled with glass fibers would be necessary to continue this study.

Chapter 9

Conclusions and Future Work

The goal of the research presented in this document was to improve the wear life of an oscillating, hydraulic face seal. Modifications to the geometry of the seal as well as the application of an entirely new material in the seal lip were considered. The research presented in this document is by no means complete. Suggestions for future work are thus included.

9.1 Summary of Conclusions

In order to explore any modifications to the seal design, a first step was to use experiments involving time lapse video of the wear process and LIF measurements of lubrication films in order to determine the primary cause of seal wear. Through this work, dirt penetration and abrasion were identified as the primary wear mechanisms.

Micromechanical modeling of the abrasion process demonstrated that regions of increased stresses and strains in the seal lip were caused by the presence of particles. These results then suggested the use of textures on the seal surface to control the seal's aggressive wear period by trapping the abrasive particles within the textures. This would not only prevent the particle from progressing across the seal lip, but it would also eliminate the increased stresses and strains that would have otherwise been caused by the particle. Experimentation confirmed that the textures improved wear greatly; however, they also revealed that the wear reduction mechanism was not as hypothesized. That is, the textures did not improve wear life by trapping the particles within the textures. Time lapse video, coupled with finite element models of the textures, revealed localized contact stress peaks and improved lubrication to be the primary wear reduction mechanisms. Localized pressure peaks acted as barriers to the advancing particle front, and the new contact stress

distribution (as altered by the presence of textures) provided additional lubrication at key points of high contact stress, namely at the seal lip edge and at the textures. Parametric finite element models also helped determine how changes in the texture geometry might be used to advantageously change the contact stress distribution across the seal lip band.

On the materials front, the use of fiber-filled rubbers was suggested as a possible alternate material for use in the seal lip. Industry and academia have found ways to successfully combine fibers and rubber to improve properties such as modulus, fracture toughness, fatigue resistance, and wear resistance. However, for the successful application of such a material in seals, models of fiber-filled rubber wear would be extremely important. Thus, a unit cell finite element model was created as a means for developing such a model. As a first step, confidence in the unit cell model was demonstrated by showing its ability to capture the plane strain compression stress-strain behavior of rubbers filled with varying volume fractions of fibers. With this confidence, foundation work was then laid for developing wear models by examining the stress and strain distributions within the unit cell and discussing them in light of some rubber wear models.

9.2 Future Work

The research presented in this document is by no means complete. Further research can certainly be conducted in regards to the modeling of fiber filled rubber wear, and further studies are needed which investigate the optimization of texture geometries. Furthermore, the micromechancial modeling of the wear mechanisms has mainly concerned dirt abrasion only. The issue of particle entrance still needs to be addressed. Thus, some ideas for continuing work are presented below.

9.2.1 Texture Geometry

In chapter 4, it was mentioned that the parametric finite element studies could be used to tailor an advantageous contact stress and lubrication distribution across the seal lip

band. In order to fully utilize the results of the parametric studies and to optimize the texture design, additional experimentation with different texture geometries should be performed to determine the minimum requirements of contact stress and lubrication. The results of these experiments could also add further insight into the wear reduction mechanism of the textures.

Furthermore, additional simulations should be conducted using the three dimensional finite element model so that more accurate contact stress profiles can be viewed. Specifically, it would be extremely interesting to shear the texture, simulating actual seal oscillation motions. Additionally, the parametric studies could be repeated using a more accurate material model in light of the limitations of the Mooney-Rivlin model (section 7.2.4).

9.2.2 Material Modeling

At the conclusion of chapter 8, confidence in the fiber unit cell model was demonstrated through very reasonable predictions of the plane strain compression behavior of the glass fiber filled polyurethane. A three dimensional model would also be extremely important for the material modeling of fiber filled rubbers. So far, the fiber has really been a "sheet" of fiber material. The three dimensional model would not only permit exploring the uniaxial compression behavior of the rubber composite but it would permit exploring the effects of fiber orientation in all of its degrees of freedom. Thus, three dimensional multi-fiber models may reveal even more information about how the fibers interact with each other.

Other considerations for future work related to the modeling of fiber filled rubbers are (1) exploring other constitutive models which would better capture the hysteresis behavior of the material and (2) the development of a wear model through the unit cell finite element model and further experimentation. In particular, the unit cell finite element model could be used in an investigation into the role of the fiber as a crack arrester.

9.2.3 Micromechanical Modeling of Wear

Further improvements can be added to the dirt abrasion simulations. One important observation is that the size of abrasive particle and the size of the fiber are of equal length scales (25 μm diameter for the particle versus 10 μm diameter for the fiber). Thus, modeling the fiber in the seal lip in addition to the abrasive particle could be extremely interesting and quite revealing as to how fibers might reduce wear (fig 9.1). In addition, repeating these simulations with a new material model such as the Arruda-Boyce elastic-visco plastic model is an extremely important consideration for future work. The Mooney-Rivlin model has been shown to be particularly poor predictor of material behavior in different loading conditions. In these dirt abrasion simulations, the material block is certainly deformed into a very complicated state.

Finally, the use of textures was designed to reduce wear by controlling dirt abrasion. The issue of dirt penetration has not been really addressed in this document. Thus, additional micromechanical modeling of the particle entrance event would be important for generating new ideas about how to improve the life of the seal through geometric modifications. In particular, two types of simulations are suggested.

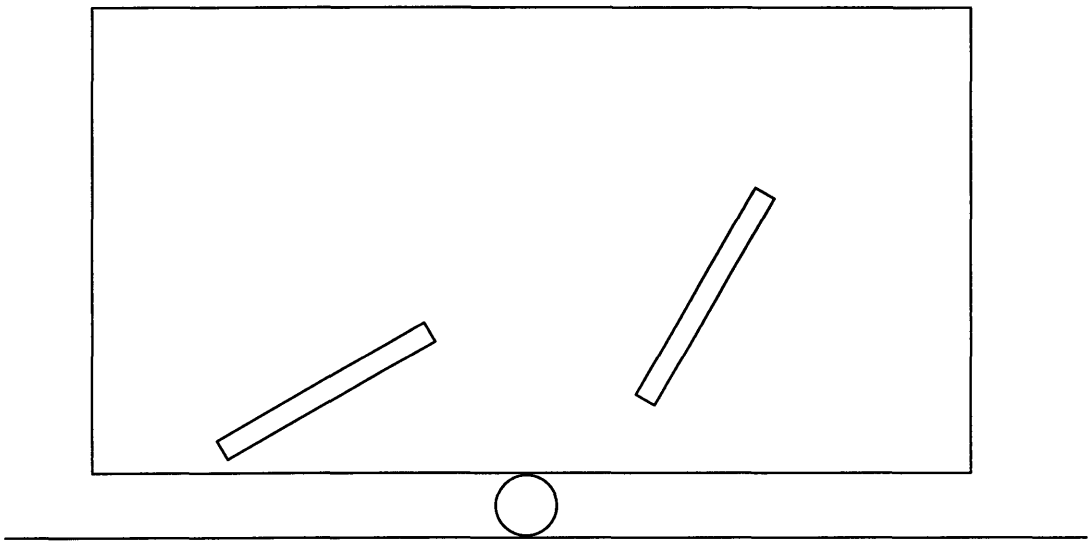

Figure 9.1: Micro-mechanical model including fibers.

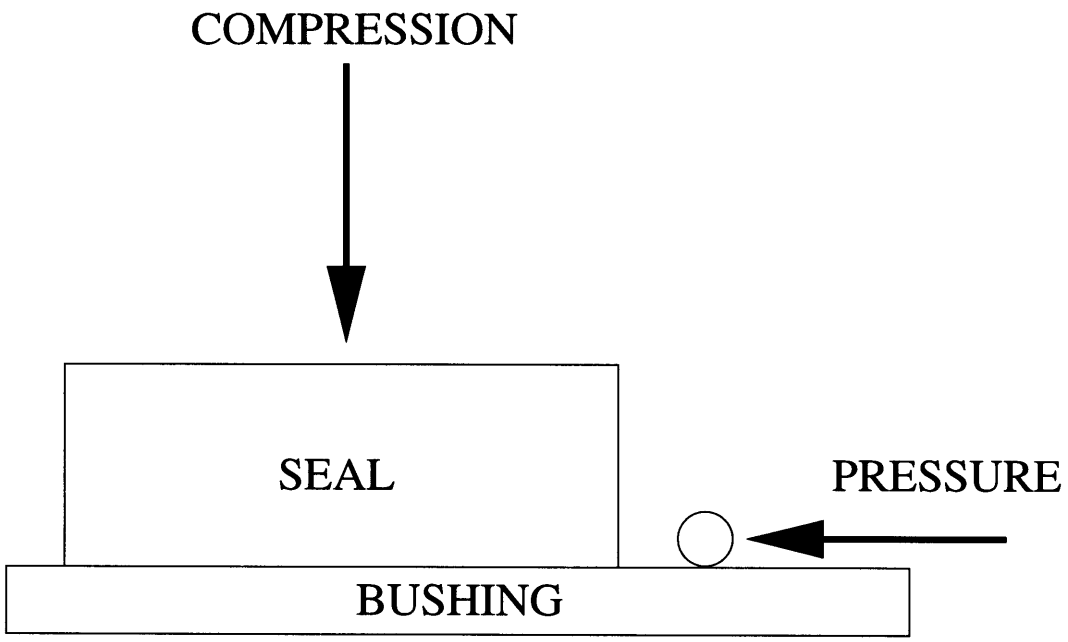

Figure 9.2: Schematic of pressurized particle simulations.

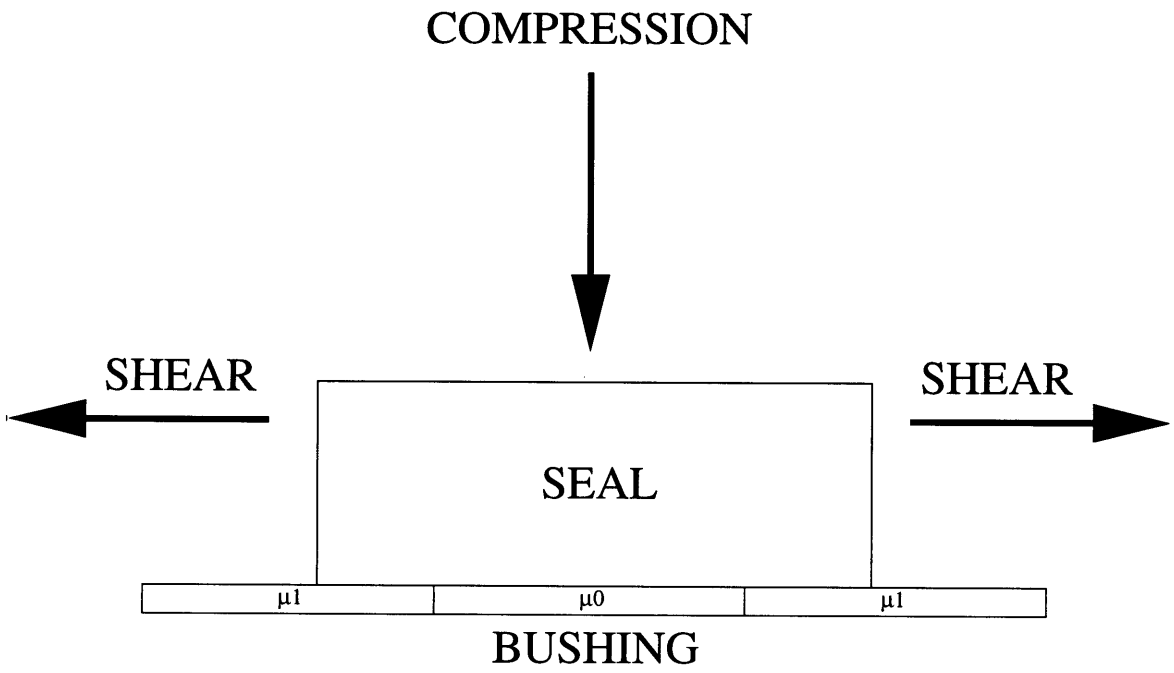

Figure 9.3: Schematic of seal lip buckling.

The first involves estimating the magnitude of pressure necessary for a particle to be forced into a the seal lip contact band. In these simulations, an abrasive particle is forced into the edge of a compressed block of material through a displacement boundary condition. As the particle tries to make its way into the block, the reaction forces on the particle can then be recorded. These simulations would be extremely valuable from a design point of view since direct comparisons can be made between different seal lip edge designs by calculating the force on the particle. A schematic of this simulation is shown in figure 9.2.

The second simulation suggests a possible mechanism by which a particle enters a seal lip contact band. Due to a difference in friction coefficient between two sections of the seal contact band, it is possible that the seal lip could locally buckle. This buckling would then provide an entrance for abrasive particles. This difference in friction coefficients could be due to a loss of lubrication in one section of the seal. One possible reason for this non-uniform lubrication is the oscillatory motion of the seal. During the time frame for a reversal in the direction of motion of the seal, the lubricant may not yet have settled to a uniform distribution. Also, at the outside edges of the seal lip, the contact pressure is highest, meaning that the lubrication is very low in this region, as shown in chapter 2. This condition may not be perfectly uniform around the entire circumference.

Therefore, these simulations examine compressing and then shearing a block of material over a surface which has regions of varying coefficients of friction. The size of each region and the friction coefficient gradient would both be varied in this study. Figure 9.3 shows a diagram of this type of simulation. The hopeful outcome of these simulations would be local buckling of the material block. Estimations of the size of the opening could then be made.

References

[1] Brown, Melvin W. 1990. *Seals and Sealing Handbook, 3rd Edition.* Oxford, England: Elsevier Science Publishers Limited.

[2] Horve, Leslie A. 1994. Understanding the Sealing Mechanism of the Radial Lip Seal for Rotating Shafts. *Proceedings of the 15th International Conference on Fluid Sealing.*

[3] Sponagel, S., G. Kilthau, G., and K. H. Spies. 1987. Sealing Mechanisms of Lip Seals. *Proceedings of the 11th International Conference on Fluid Sealing.*

[4] Salant, R. F. 1996. Elastohydrodynamic Model of the Rotary Lip Seal. *Transactions of the ASME Journal of Tribology* 118(April): 292-296.

[5] Tichy, John A. 1995. A Surface Layer Model for Thin Film Lubrication. *Tribology Transactions* 38(3): 577-582.

[6] Cogdell, J. D., M.C. Dawson, F. F. Ling, and S. F. Murray. 1986. Surface Texture Effects in Thin Film Lubrication of Steel by Silicones. *ASLE Transactions* 30(2): 141-148.

[7] Symons, J. D. 1973. The Shaft and Radial Lip Seal Performance. *Proc. Inst. Conf. on Surface Technology*: 584.

[8] Jagger, E. T., and D. Wallace. 1970. Oil Seal Research. *Industrial Lubrication and Tribology* (February).

[9] Potosky, T. Optimized Seal Performance Through Surface Finish Technology. (Private communication from Caterpillar, Inc.).

[10] Tanoue, H.; Ishiwata, H.; and Tada, H. 1971. Effects of Solid Particles in Lubricating Oil on the Wear of Oil Seals and Shafts. *Proceedings of the 5th International Conference on Fluid Sealing.*

[11] Golubiev, A. I. and V. V. Gordeev. 1975. Investigation of Wear in Mechanical Seals in Liquids Containing Abrasive Particles. *Proceedings of the 7th International Conference on Fluid Sealing.*

[12] Hirabayashi, H., Y. Kato, and H. Ishiwata. 1967. Excessive Abrasion of Mechanical Seals Caused by Salt Solutions. P*roceedings of the 3rd International Conference on Fluid Sealing.*

[13] Ayala, H. 1995. The Effects of Soil Abrasives on Rotary Seal Effectiveness. S.M. Thesis, MIT, Cambridge, MA.

[14] Ayala, H., O. Yeh, D. Hart, and M. C. Boyce. 1997. Seal Designed for Reduced Wear in Abrasive Slurries. *Proceedings of the ASME Fluids Engineering Division Summer Meeting.* (in press)

[15] Ayala, H. Ph.D. Thesis (in press), MIT, Cambridge, MA.

[16] Arruda, E. and M. C. Boyce. 1991. On Modeling the Mechanics of Rubber Elasticity: State of Deformation Dependence. Private Communication.

[17] Hibbit, Karlsson, & Sorensen, Inc. *ABAQUS Theory Manual, Version 5.5.* Pawtucket, RI. 1995.

[18] Arruda, E. M. and M. C. Boyce. 1993. Evolution of Plastic Anisotropy in Amorphous Polymers During Finite Straining. *International Journal of Plasticity* 9: 697-720.

[19] Arruda, E. M. and M. C. Boyce. 1993. A Three Dimensional Constitutive Model for the Large Stretch Behavior of Rubber Elastic Materials. *J. Mech. Phys. Solids* 41(2): 389-412.

[20] Mullins, L., and N. R. Tobin. 1965. Stress Softening in Rubber Vulcanizates. Part I. Use of a Strain Amplification Factor to Describe the Elastic Behavior of Filler-Reinforced Vulcanized Rubber. *Journal of Applied Polymer Science* (9): 2993-3009.

[21] *Fatigue and Tribological Properties of Plastics and Elastomers.* 1995. New York: Plastics Design Library.

[22] Rivlin, R. S. and A. G. 1953. Thomas. *Journal of Polymer Science* (10): 191.

[23] Suresh, S. 1991. *Fatigue of Materials.* New York: Cambridge University Press.

[24] Gent, A. N., P. B. Lindley, and A. G. Thomas. 1964. Cut Growth and Fatigue of Rubbers. I. The Relationship between Cut Growth Rate and Fatigue. *Journal of Applied Polymer Science* 8: 455-466.

[25] Shallamach, A. 1968. *Journal of Applied Polymer Science* 12: 281.

[26] Ratner, S. B. I. I. Farberova, O. V Radyukevich, and E. B. Lure. 1964. *Soviet Plastics* 7: 37.

[27] Tian, H., N. Saka, and N. P. Suh. 1989. Boundary Lubrication Studies on Undulated Titanium Surfaces. *Tribology Transactions* 32(3): 289-296.

[28] Swanson, S. R. 1997. *Introduction to Design and Analysis with Advanced Composite Materials.* Upper Saddle River, NJ: Prentice-Hall, Inc.

[29] Geethama, G., R. Joseph, and S. Thomas. 1995. Short Coir Fiber-Reinforced Natural Rubber Composites: Effects of Fiber Length, Orientation, and Alkali Treatment. *Journal of Applied Polymer Science* 55: 583-594.

[30] Kwon, Y. D., C. W. Beringer, M. A. Feldstein, and D. O. Prevorsek. 1990. Fatigue Endurance and Viscoelastic Hysteresis of Short Fiber/Rubber Composites. *Rubber World* 202 (2): 29-33.

[31] Kikuchi, N. 1996. Tires Made of Short Fiber Reinforced Rubber. *Rubber World* 214 (3): 31.

[32] Wada, N. and Y. Uchiyama. 1993. Friction and Wear of Short-Fibre-Reinforced Rubber Composites Under Various Sliding Speeds and Loads. *Wear* Vol. 162-164: 930-938.

[33] Saito, K., Ah. Araki, and T. Nakamura. 1996. Stereological Modeling and Micromechanical Analysis of Rubber Particle-Reinforced Epoxy Composite Materials. *Mechanics of Composite Materials* 32 (3): 217-226.

[34] Yang, A. C.-M., J. E. Ayala, and J. C. Scott. 1991. Abrasive Wear in Filled

Elastomers. *Journal of Materials Science* 26: 5823-5837.

[35] Najm, H. S. and A. E. Naaman. 1995. Prediction Model for Elastic Modulus of High-Performance Fiber Reinforced Cement-Based Composites. *ACI Materials Journal* 92 (3): 304-314.

[36] Fan, C. F. and S. L. Hsu. 1992. A Study of Stress Distribution in Model Composites by Finite-Element Analysis. II. Fiber/Matrix Interfacial Effects. *Journal of Polymer Science: Part B: Polymer Physics* 30: 619-635.

[37] Siah, K., J. A. Mandel, and B. R. Mousa. 1992. Micromechanical Finite Element Model for Fiber-Reinforced Cementitious Materials. *ACI Materials Journal* 89 (3): 277-288.

[38] Swanson, S. R. A Micro-Mechanics Model for In-Situ Compression Strength of Fiber Composite Laminates. *Transactions of the ASME Journal of Engineering Materials and Technology* 114: 8-12.

[39] Arruda, E. M., M. C. Boyce, and H. Quintus-Bosz. 1993. Effects of Initial Anisotropy on the Finite Strain Deformation Behavior of Glassy Polymers. *International Journal of Plasticity* 9: 783-811.

[40] Bergstrom, J. S. and M. C. Boyce. Constitutive Modeling of the Large Strain Time-Dependent Behavior of Elastomers. (in press).